IMPERIAL

Imperial College London
Faculty of Engineering
Department of Chemical Engineering

Crystal Regeneration: Investigating the Post-Breakage Growth Phenomenon in Organic Crystals

Isha Surendra Bade

Dissertation submitted to Imperial College London for the degree of
Doctor of Philosophy
October 2024

Statement of Originality

I hereby declare that the work presented in this thesis is my own and has been generated by me as the result of my own original research. Any contributions made by others to the research described in this thesis have been explicitly acknowledged. This thesis has not been submitted for any other degree or qualification at this or any other institution.

The content of this thesis (text, figures, tables, graphics) represents my own research and does not include work formed in part or entirely by others, except where such contributions have been explicitly indicated and duly referenced. All sources of information have been appropriately cited.

Signed,
Isha Bade

Copyright

The copyright of this thesis rests with the author. Unless otherwise indicated, its contents are licensed under a Creative Commons Attribution-Non Commercial 4.0 International Licence (CC BY-NC).

Under this licence, you may copy and redistribute the material in any medium or format. You may also create and distribute modified versions of the work. This is on the condition that: you credit the author and do not use it, or any derivative works, for a commercial purpose.

When reusing or sharing this work, ensure you make the licence terms clear to others by naming the licence and linking to the licence text. Where a work has been adapted, you should indicate that the work has been changed and describe those changes.

Please seek permission from the copyright holder for uses of this work that are not included in this licence or permitted under UK Copyright Law.

Acknowledgements

I would like to begin by expressing my heartfelt thanks to my supervisor, Jerry Heng, for his constant guidance throughout my PhD, not only in research but also on a personal level. His belief in me has been incredibly encouraging, and I am deeply grateful for all the positive experiences and opportunities he provided. My gratitude also extends to Dr. Vivek Verma, who has been a source of unwavering support, both academically and as a friend. Additionally, I would like to thank Dr. Vikram Karde and Dr. Ian Rosbottom for their guidance during the early stages of this journey.

A special thanks to the members of the Heng group—Ethan Errington, Hamish Mitchell, Deniz Etit, Angeliki Chalasti, Jianing Li, and Daniele Pessina—for being friends more than colleagues. Your feedback on my work and your camaraderie during difficult times made all the difference.

I am also grateful to those at Imperial College London who supported me at various stages of the PhD. Dr. Colin Hale, for his steady moral support, Marcus Yio for assistance with Nano indentation, Hamish Mitchell for helping set up the automated robot, and Kaho and Patricia for their training on the analytical equipment.

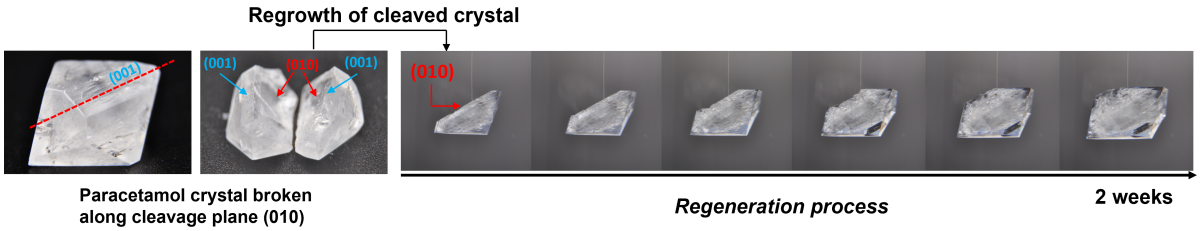
To my dearest friends Ivaxi, Rasika, Raghul, Nikhil, Vinay, Kanksha, and Varun—thank you for sticking with me through this journey and offering encouragement in all ways possible. A huge thank you to Nathan, who bore the brunt of my frustration and anxiety and supported me unconditionally. My extended family in India, though far, has always been my safe haven and a constant reminder of my roots.

Lastly, to my grandmother, Ajji, whose strength and resilience I aspire to emulate; to my brother, Viyan, who never failed to provide banter especially on the days I needed it the most and has been my biggest cheerleader; and most of all, to my parents, Aai and Baba, whose unwavering belief in me has pushed me forward through every low point—thank you. I owe my PhD journey to your endless support and encouragement.

For Aai, Baba, Ajji, and Viyan

Abstract

This thesis investigates the 'crystal-regeneration' phenomenon, where a single macroscopic paracetamol crystal, broken along its cleavage plane (010), extrinsically regenerated into its pre-breakage shape before growing equivalently to its unbroken counterpart. Regeneration occurred via rapid growth along the cleavage plane, with facets on the intact crystal remaining dormant until the shape was restored. The extent and orientation of breakage influenced regeneration: breakage parallel to the cleavage plane promoted regeneration as opposed to perpendicular breakage, emphasising the importance of both particle size and shape evolution after breakage. Growth perpendicular to the cleavage plane was at least twice as fast as parallel growth, with most regeneration occurring in the experiment's initial phase. These observations support a two-step mechanism consisting of a fast phase followed by a slower phase.



Graphical abstract: Crystal regeneration observed in a form I paracetamol crystal post breakage along the cleavage plane

The phenomenon was elucidated through intricate single crystal experiments, supported by advanced imaging setups and automated image analysis via MATLAB to measure facet-specific growth rates. Crystal regeneration was examined in three solvents—ethanol, acetone, and tetrahydrofuran (THF)—across various supersaturations (1.03 to 1.30) and under agitation. Regeneration was favourable under all tested conditions, with solute-solvent interactions, hydrodynamics, and thermodynamics influencing the process. Solute-surface interactions, driven by higher solubility, were preferred over unfavourable solvent-surface interactions, resulting in higher regeneration rates. Regardless of conditions, regeneration led to accelerated growth kinetics strongly dependent on supersaturation, following power law kinetics. Cleaved crystals also enhanced secondary nucleation, showcasing their potential as a seeding strategy in batch crystallisation processes.

Crystal regeneration challenges traditional morphological theories that emphasise the

influence of slow-growing facets, as broken crystals behave differently. The preferred 'switching off' of facets during regeneration suggests a possible link between crystal 'shape-memory' effect and surface energetics. This thesis systematically explores crystal behaviour post-breakage and proposes mechanisms to explain these phenomena, offering critical insights into previously unexplored post-breakage crystal growth dynamics.

Publications

Papers published during the PhD:

1. **Isha Bade**, Vivek Verma, Ian Rosbottom, and J. Y. Y. Heng*, Crystal regeneration - a unique growth phenomenon observed in organic crystals post breakage, *Materials Horizons*, 2023, 10, 1425-1430

   This paper corresponds to the first results chapter (Chapter 4) of the thesis

2. **Isha Bade**, Vikram Karde, Luke Schenck, Marina Solomos, Margaret Figus, Chienhung Chen, Stephanus Axnanda*, and Jerry Y. Y. Heng*, Process-Induced Crystal Surface Anisotropy and the Impact on the Powder Properties of Odanacatib, *Pharmaceutics*, 2024, 16, 7, 883

3. Vivek Verma, **Isha Bade**, Vikram Karde, and J. Y. Y. Heng*, Experimental Elucidation of Templated Crystallization and Secondary Processing of Peptides, *Pharmaceutics*, 2023, 15, 4, 1288

In preparation

1. **Isha Bade**, Deniz Etit, and J. Y. Y. Heng*, Effect of solvents on the regeneration phenomenon in organic crystals, *CrystEngComm*, In preperation

Conferences

1. **2022, July, 7th European Conference on Crystal Growth (ECCG7), France**

   Regeneration Phenomenon in Crystals Post Breakage - A case study on Paracetamol

   Oral presentation

2. **2022, November, Podcast: Never Lick the Spoon, UK**

   Episode 22: Crystal Healing

   Main speaker

3. **2023, August, 20th International Conference on Crystal Growth and Epitaxy (ICCGE20), Italy**

   Regeneration Phenomenon in Crystals Post Breakage - A case study on Paracetamol

   Oral presentation

   ROSTISLAV KAISHEV AWARD: Best young scientist oral presentation

4. **2023, November, AIChE Annual Meeting, United States**

   Regeneration Phenomenon in Crystals Post Breakage - A case study of Paracetamol

   Oral presentation in invited talk session

5. **2023, November, AIChE Annual Meeting, United States**

   Effect of solvents and agitation on the regeneration phenomenon in crystals post breakage - A case study of Paracetamol

   Oral presentation

6. **2024, March, Institute of Physical Chemistry, Bulgarian Academy of Sciences Colloquium, Bulgaria**

   The 'Regeneration' phenomenon in crystals post breakage - A case study of Paracetamol

   Invited talk

7. **2024, April, ChemEng Day UK, UK**

   Effect of Supersaturation Ratio and Agitation on the 'Regeneration' Phenomenon in Crystal Growth

   Poster presentation

8. **2024, June, Chemical Engineering PhD Symposium, UK**

   Effect of Supersaturation Ratio and Agitation on the 'Regeneration' Phenomenon in Crystal Growth

   Poster presentation

   BEST POSTER AWARD

9. **2024, July, British Association of Crystal Growth (BACG), UK**

   'Regeneration' phenomenon in crystals post breakage and the effect of supersaturation ratio on the facet specific growth rates

   Oral presentation

Contents

1 Introduction **1**

1.1 Background and Motivation 1

1.2 Aims of this PhD thesis 2

1.3 Thesis overview 3

2 Literature review **5**

2.1 Crystallisation in the pharmaceutical industry 5

2.2 Fundamentals of crystallisation 6

2.2.1 Solubility 6

2.2.2 Nucleation 9

2.3 Crystal Growth 19

2.3.1 The crystal structure 19

2.3.2 Polymorphism 22

2.3.3 Crystal morphology 24

2.3.4 Morphology prediction theories 26

2.3.5 Growth mechanism and mechanistic models 27

2.3.6 Measuring growth rates 31

2.3.7 Effect of external factors on crystal growth 32

2.4 Mechanical properties of crystals 33

2.4.1 Lattice defects 33

2.4.2 Slip planes vs. cleavage planes 34

2.5 Current understanding of crystal breakage and growth 37

2.6 Crystalline state of paracetamol 39

3 Materials and Methods 42

3.1 Materials 42

3.2 Solubility determination 43

3.2.1 Metastable zone width determination 44

3.3 Macroscopic single crystals 44

3.3.1 Seed preparation 44

3.3.2 Growing large single crystals 46

3.4 Crystal cleaving 47

3.5 Crystallisation techniques for crystal regeneration 48

3.6 Imaging techniques 49

3.6.1 Optical microscopy 49

3.6.2 Macrophotography 50

3.7 Measuring crystal growth rate 51

3.7.1 Automated image analysis using MATLAB 52

3.8 Characterisation techniques 56

3.8.1 Powder X-Ray Diffraction (PXRD) 56

3.8.2 Scanning Electron Microscopy (SEM) 57

3.8.3 X-Ray Photoelectron Spectroscopy (XPS) 59

3.8.4 Nanoindentation 61

3.9 Computational Methods 63

3.9.1 Cambridge Structural Database (CSD) 63

3.9.2 CSD Mercury 64

3.9.3 Accelrys Materials Studio 7.0 65

4 Crystal regeneration - a proposed growth mechanism in crystals post breakage 68

4.1 Overview 68

4.2 Methods 69

4.2.1 Obtaining and cutting paracetamol crystals 69

4.2.2 Bench top optical microscopy for small crystals 70

4.2.3 Macro photography for large crystals 71

4.2.4 Powder XRD 72

4.2.5 Scanning electron Spectroscopy 72

4.2.6 Nanoindentation 72

4.2.7 Computational methods 72

4.3 Results 73

4.3.1 Identifying cleavage planes of form I paracetamol crystals 73

4.3.2 Effect of extent and orientation of breakage on regeneration . . . 77

4.3.3 Growth rates of cleaved crystals vs. unbroken crystals 79

4.4 Discussion 83

4.4.1 The proposed regeneration mechanism 83

4.4.2 Effect of regeneration on crystal shape and form 84

4.4.3 Effect of regeneration on the fracture properties of crystals 86

4.4.4 Effect of regeneration on crystal quality 89

4.5 Conclusion 91

5 Design of isothermal crystallisation set-up with integrated macrophotography to investigate solvent effects on crystal regeneration 92

5.1 Overview 92

5.2 Methods 93

5.2.1 Solubility of paracetamol in different solvents 93

5.2.2 Isothermal crystallisation without agitation 94

5.3 Results 95

5.3.1 Experimental habits and PXRD patterns of paracetamol crystals from different solvents 95

5.3.2 Solubility of paracetamol in pure solvents 96

5.3.3 Effect of solvent on the rate of regeneration 98

5.4 Discussion 102

5.5 Conclusion 107

6 Effect of supersaturation and agitation on the regeneration rates of paracetamol crystals 108

6.1 Overview 108

6.2 Methods 109

6.2.1 Isothermal crystallisation with agitation 109

6.3 Results 110

6.3.1 Metastable zone width determination 110

6.3.2 Effect of supersaturation on the rate of regeneration 111

6.3.3 Effect of agitation on the rate of regeneration 115

6.3.4 Secondary nucleation in agitated system 118

6.4 Discussion 119

6.5 Conclusion 124

7 Conclusions and Future Work 125

7.1 Overall Contributions and Conclusions 125

7.2 Future Work 128

7.2.1 Recyclability of crystals 128

7.2.2 Effect of crystal orientation 128

7.2.3 Automated optical microscopy for regeneration screening 129

7.2.4 Regeneration in other organic crystal 130

A Results **132**

A.1 Growth rates of large crystals 132

A.2 Hardness of facets before and after regeneration 133

A.3 MATLAB script for Image analysis 134

B Figure Permissions **139**

References **139**

List of Tables

2.1 The 7 crystal systems and 14 Bravais lattices [1] 21

3.1 Lattice parameters of HXACAN01 before and after optimisation using COMPASSII forcefield and the associated relative error 66

4.1 Interplanar spacing, d_{hkl}, attachment energy, E_{att}, specific interaction energy (SIE), and total facet area, of the major facets of the vacuum habit of paracetamol as obtained from Materials Studio 75

4.2 Surface analysis results including rugosity and the density of chemical moieties of the major facets of form 1 paracetamol 76

4.3 Average growth rates of length a and b of cleaved crystals during fast regeneration, slow regeneration, and overall growth 82

4.4 Average growth rates of length a and b of whole crystals during regeneration and overall growth of cleaved crystals 82

4.5 Reduced modulus, E_r, of facets (001) and (010) before and after regeneration 89

5.1 Solubility of paracetamol in g/ml $\pm$ SD $\times 10^{-4}$ in three different solvents; ethanol, THF and acetone 97

5.2 Crystallisation conditions at S = 1.10 for the regeneration of paracetamol in ethanol, acetone, and THF 97

5.3 Fast and slow regeneration rates of paracetamol in different solvents at S = 1.10 101

5.4 Elemental composition of different facets determined via XPS 103

5.5 Interaction energy between solvent and (010) crystal surface along with the solvent dielectric constant and molecular weight 105

6.1 Fast and slow regeneration rates of paracetamol in ethanol at different supersaturations 114

6.2 Summary of the facet-specific growth rates of cleaved and whole paracetamol crystals in agitated and non-agitated environments with the time taken for secondary nucleation detection. 118

6.3 Parameters of the power law equation fitted to the facet specific growth rates of cleaved and whole paracetamol crystals 121

A.1 Growth rates of small and large crystals in the different phases of regeneration along with the standard deviation in mm/hr 133

List of Figures

2.1 A generalised phase diagram showing the solubility curve and the three thermodynamically varied regions 7

2.2 A schematic of the major categories of nucleation processes 10

2.3 Free energy diagram for the nucleation process as a function of the nuclei radius 11

2.4 (a) induction time data showing preferred nucleation in the hexagonal pores of polymer films (b) Aspirin crystals nucleated inside the square pores due to favourable interactions at the pore angles. (a) and (b) adapted with permission from [2] (c) Molecular dynamic simulations showing cluster formation of paracetamol and fenofibrate molecules of MCC surface due to hydrogen bonding. Figure adapted with permission from [3] (d) paracetamol crystals nucleating on D-mannitol crystal and (e) pimelic acid crystals nucleating on malonamide single crystal. Images obtained with permission from [4] and [5] respectively 16

2.5 Left: Main mechanisms of secondary nucleation, obtained with permission from [6] Middle: Surface nuclei breeding mechanism shown via molecular dynamic simulations at moderate supersaturation, obtained with permission from [7] Right: Updated phase diagram depicting the secondary nucleation threshold for seeded systems, highlighting the seed growth only and seed proliferation zones, obtained with permission from [6] 18

2.6 Left: Typical unit cell, Right: Example of miller indices based on a typical unit cell, obtained with permission from [1] 20

2.7 Left: simplified breakdown of the solid phase, adapted from [8] Right: Schematic of the Ostwald's rule of stages, depicting the journey from solution (S), to phase 4 (least stable),3,2, and 1 (most stable), image taken with permission from [9] 23

2.8 (a) Wulff construction, obtained with permission from [10], (b) Diagram showing the Frank-Chernov condition, used with permission from [11] . . 24

2.9 (a) Three possible sites on a crystal surface for growth unit incorporation; A: terrace, B: ledge, C: Kink, (b) The three growth regimes, rough growth, 2D nucleation, and spiral growth, (c) Diagram depicting the change in growth regimes with supersaturation. All images have been obtained with permission from [1, 12, 13] respectively. 28

2.10 (a) Effect of surface corrugation on slip propensity. Top: High corrugation but no interpenetration between 2 layers, hence highly likely to slip. Bottom: Less corrugation but high interpenetration between the 2 layers, thus more likely to cleave. Image obtained with permission from [14] (b) Matrix depicting the possible outcomes of the interplay between slip plane energy and the detachment energy, adapted from [15] 35

2.11 (a) 2-(Methylthio)nicotinic acid crystal bent on the (010) face (b) self-healing dipyrazolethiuram disulfide crystal after application of moderate mechanical compression (c) Self-healing of the cracks in a ferroelastic crystal AMU3. Images have been obtained with permission from [16] [17], and [18] respectively 39

2.12 Comparison between the chemical structure of (a) paracetamol and (b) metacetamol, highlighting the difference in the *para* and *meta* positions of the amide and hydroxyl functional groups 40

2.13 (a) The packing and morphology of form I and form II paracetamol, used with permission from [19], (b) form I paracetamol grown in top: ethanol, bottom: water vapour at (i) low and (ii) high supersaturation, (c) facet specific growth rates of form I paracetamol as a function of supersaturation. (b) and (c) used with permission from [20] 41

3.1 Representative image showing a broad classification of (a) High quality seeds and (b) Poor quality seeds 45

3.2 Slow solvent evaporation procedures for (a) obtaining paracetamol seeds, (b) isolating the seeds to grow small macroscopic crystals, and (c) dangling the small crystals in solution using kevlar fibres to obtain large crystals . 47

3.3 left: Macroscopic paracetamol crystal grown in ethanol being cut using a scalpel by applying point pressure on the (001) facet, Right: Paracetamol crystal after cleavage, with (010) plane exposed 48

3.4 (a) Leica M60 stereo microscope used for optical microscopy of single crystals (b) Macrophotography set-up designed for single crystal imaging . . 51

3.5 Diagram depicting the measurement of (a) Characteristic dimensions: length a and b (b) Facet propagation of (010) and (110), on a simplified drawing of a paracetamol crystal as viewed through the microscope and camera . 52

3.6 A summary of the steps used in the MATLAB script to analyse crystal images, starting from preprocessing into binary image all the way to edge detection and obtaining measurements 55

3.7 (a) Visual representation of the working principle of PXRD (b) Typical PXRD pattern obtained from a powdered sample of *(a)* form I paracetamol, and *(b)-(g)* its cocrystals and salts - image used with permission from [21] 56

3.8 (a) Visual representation of the working principle of SEM (b) A macroscopic paracetamol crystal, coated in a thin layer of gold, and placed on a stainless steel stub using carbon tape in preparation for SEM imaging . . 58

3.9 (a) Visual representation of the working principle of XPS and (b) paracetamol crystals mounted on a sample holder in preparation for XPS . . . 60

3.10 (a) Paracetamol crystal being indented in the SPM nanopositioner using a Berkovich diamond tip (b) A representative Load vs depth (P-h) curve showing the loading and unloading profiles fitted using the Oliver and Pharr fit, where h_f and h_{max} are the final indentation depth and indentation depth at maximum load respectively (c) representative image showing the pyramidal indent post tip unloading on a paracetamol facet 63

3.11 Diagram summarising the MD simulation set-up on Materials Studios for calculating the surface-solvent interaction energy 67

4.1 Summary of the extent and orientation of breakage studied: parallel to the cleavage plane - 50% (cleaved), 25%, 10% and perpendicular to the cleavage plane - chipped. Note: The crystal diagrams are simplified representations of a paracetamol crystal as seen through the microscope and camera. For a comparison with the actual crystal, please refer to Figure 3.3. 70

4.2 (a) Vacuum habit of form I paracetamol (HXACAN01) predicted by the attachment energy theory using Materials Studio (b) BFDH morphology of paracetamol calculated using Mercury (c) Experimental habit of paracetamol crystal grown in ethanol 73

4.3 Depiction of the packing of corrugated (010) and (020) planes, highlighting the hydrogen bonding in the *a* and *c* direction 74

4.4 Analysed surfaces of planes (a)(010) and (b)(011) as obtained from Mercury depicting the (i) packing and hydrogen bonding, (ii) topological information, and (iii) surface chemical functionalities 76

4.5 Regeneration observed in (a) 50% cleaved, (b) 25% mother, and (c) 10% mother paracetamol crystal 77

4.6 (a) Regeneration observed in a 10% daughter paracetamol crystal and (b) Growth behaviour of a chipped paracetamol crystal 78

4.7 Snapshots of (a) a cleaved crystal regenerating post breakage and (b) the growth trajectory of a whole crystal. Averaged over at least 3 samples, the normalised growth behaviour of (c) cleaved crystals compared to (d) whole crystals during the entire 300 hours of the experiment. (FR and SR stand for 'Fast Regeneration' and 'Slow Regeneration' respectively) . . . 80

4.8 Propagation of characteristic dimensions a and b over time for 3 cleaved and 3 whole crystals: (a) Length a of cleaved crystal, (b) Length b of cleaved crystal, (c) Length a of whole crystal, and (d) Length b of whole crystal 81

4.9 The proposed regeneration mechanism consisting of 2 phases; fast regeneration, and slow regeneration, followed by the overall growth of the crystal post shape restoration 84

4.10 PXRD spectra of paracetamol crystals top to bottom, form II predicted using Mercury, form I predicted using Mercury, as received paracetamol powder, paracetamol seeds grown in ethanol solution, paracetamol crystals regenerated in ethanol solution 85

4.11 SEM images of (010) facet at different time intervals during regeneration (a) at 0 hours, (b) 25 hours and (e) 50 hours after cleaving. 86

4.12 Example of the load-displacement curves obtained for the paracetamol facets,(a) (001) and (b) (010), before regeneration. The curves highlight the 'pop-in' behaviour commonly observed in molecular crystals along with micrographs of the indent 87

4.13 (a) Bar chart depicting the hardness of facets before and after regeneration where the error bars correspond to the standard deviation across 3 samples with 9 indents each. (b) images of the indents after regeneration on facet (i) (001) and (ii) (010) along with (b)(iii) the image of facet (010) exposed from a regenerated crystal 88

5.1 (a) isothermal crystallisation set-up using a jacketed vessel connected to a circulating waterbath and imaging done via a DSLR camera at fixed time intervals (b) Temperature profile for isothermal crystallisation where T_0 is the initial temperature at which solution is equilibrated and T_c is the temperature required to reach $S = 1.10$ 94

5.2 Experimental habits of paracetamol obtained via slow evaporation in (a) Ethanol, (b) THF, and (c) Acetone. The crystals in the image are approximately 1 cm large along their longest dimension (d) diagrams highlighting the characteristic dimension and (010) facet propagation on the observed experimental habits in the different solvents 96

5.3 (a) Solubility curves of paracetamol in the three solvents and (b) the PXRD spectra of the crystals obtained from top to bottom: THF, acetone, and ethnaol 97

5.4 (a) Regeneration snapshots of paracetamol in top to bottom: ethanol, THF and acetone 98

5.5 Example plots of crystal growth in each solvent obtained via MATLAB. Each line represents 1 individual crystal: (a) facet propagation of (010) for the entire duration of the experiment. Using this plot, the duration of the fast regeneration and the total regeneration period was deduced. Change in characteristic dimension b (b) during regeneration and (c) after regeneration. The gradients of these plots were used to estimate the growth rates 99

5.6 (a) Growth rates of (010) and length b during regeneration along with the absolute and normalised time taken for regeneration in each solvent. (b) Growth rates of length a and b after regeneration in all three solvents. Error bars in each case represent the standard deviation 100

5.7 (a) An example plot of the deconvoluted carbon spectra of individual facets, (001) in this case (b) Overlayed carbon spectra of all major facets to highlight the differences in functional group composition (c) Summary plot of the amount of C-C bonding environment and ratio of C=O to C-C in each facet as well as a comparison with the aromatic bonds density obtained via Mercury in Table 4.2 104

5.8 Snapshots of the bilayer at the end of the MD simulations depicting the bonding between the top layer of (010) surface with (a) ethanol, (b) acetone, (c) THF 106

5.9 RDF analysis of the bonding between the (010) surface and (a) ethanol, (b) Acetone, and (c) THF 106

6.1 (a) isothermal crystallisation set-up with agitation using a magnetic stirrer (b)(i)-(iii) Cleaved crystal without agitation, cleaved crystal with agitation, whole crystal with agitation respectively, studied at 5 different S values; 1.03, 1.10, 1.17, 1.25, and 1.33 110

6.2 Solubility curve of paracetamol-ethanol system determined experimentally and compared against literature sources; Granberg and Rasmuson [22], and Fernandes [23]. Metastable zone width measured experimentally to select an ideal range of supersaturations for crystal growth experiments. Error bars represent standard deviation across a sample size of 3 repeats. Error bars for solubility curve are too small and hence can be found in Table 5.1 111

6.3 Snapshots of regenerating crystal at different supersaturation; top to bottom, 1.03, 1.10, 1.17, 1.25, 1.33, in non agitated systems along with the time taken to complete regeneration 112

6.4 Example plots of crystal growth at each S obtained via MATLAB. Each line represents 1 individual crystal: (a) facet propagation of (010) during regeneration, (a)(i) a stand-alone plot showing the facet propagation of (010) for $S = 1.03$ to ensure data clarity. Facet propagation of (110) (b) during regeneration and (c) after regeneration. The gradients of these plots were used to estimate the growth rates. 113

6.5 (a) Growth rate of (010) during regeneration as a function of supersaturation along with the time taken in hours for regeneration to finish at each supersaturation (b) Growth rates of facet (110) during regeneration (green) and after regeneration is completed (orange). Error bars demonstrate standard deviation 114

6.6 Snapshots of regenerating crystal at different supersaturation; top to bottom, 1.03, 1.10, 1.17, 1.25, 1.33, in agitated systems at 200 rpm 115

6.7 (a) Growth rate of (010) during regeneration as a function of supersaturation with and without agitation (b) Growth rates of facet (110) during regeneration and after regeneration is completed in the presence and absence of agitation 116

6.8 Snapshots of whole, unbroken crystals at different supersaturation; top to bottom, 1.03, 1.10, 1.17, 1.25, 1.33, in agitated systems at 200 rpm . . . 117

6.9 Plot depicting the delay time, t_d, for a cleaved crystal and a whole crystal grown in agitated conditions in comparison to the induction time data of paracetamol-ethanol solutions studied by Mitchell et al. [24] 119

6.10 Displacement of red dye in solution being stirred using magnetic stirrer at 200 rpm (top) without, and (bottom) with the presence of an immobilised crystal 122

6.11 Proposed mechanism of the effect of regeneration on the occurrence of secondary nucleation in stirred systems 123

7.1 Snapshots depicting the regeneration of a pristine cleaved crystal followed by 2 cycles of further regeneration post cleavage of the regenerated crystal 128

7.2 Snapshots of a cleaved crystal regenerating, despite being oriented with the cleavage plane facing sideways 129

7.3 Automated imaging set-up using Dobot, the robotic arm, and USB microscope for cystal imaging in (a) evaporative crystallisation environment, and (b) isothermal crystallisation environment 130

7.4 Macroscopic crystals of (a) carbamazepine, (b) glycine, and (c) aspirin obtained from methanol, DI water, and acetone respectively 130

7.5 Snapshots representing the regeneration behaviour observed for (a) carbamazepine in methanol, (b) glycine in DI water, and (c) aspirin in acetone over a period of 48 and 24 hours respectively 131

A.1 % Growth and growth rate of length a and b for large cleaved paracetamol crystals over a period of 200 hours. Error bars represent standard deviation across 3 crystals 132

A.2 Hardness of facets (201) and (011) before and after regeneration 133

Nomenclature

List of Abbreviations

AE	Attachment Energy
AFM	Atomic Force Microscopy
API	Active Pharmaceutical Ingredient
ATR	Attenuated Total Reflectance
B&S	Birth and Spread
BCF	Burton-Cabrera-Frank
BFDH	Bravais-Freidel-Donnay-Harka
CAGR	Compound Annual Growth Rate
CBZ	Carbamezepine
CC	Crystal Crystal interactions
CI	Crystal Impeller interactions
CNT	Classical Nucleation Theory
CSD	Cambridge Structural Database
CW	Crystal Wall interactions
DSC	Differential Scanning Calorimetry
DSLR	Digital Single-Lens Reflex
FBRM	Focused Beam Reflectance Measurement
FTIR	Fourier Transform Infrared
HPLC	High Performance Liquid Chromatography
LAS	Leica Application Suite
LDE	Ledge Directed Epitaxy

LED	Light-Emitting Diode
MAE	Modified Attachment Energy
MCC	Microcrystalline Cellulose
MD	Molecular Dynamics
MSMPR	Mixed Suspension Mixed Product Removal
MSZW	Metastable Zone Width
NCC	Non-Classical Nucleation
PBC	Periodic Bond Chain
PBM	Population Balance Modelling
PSD	Particle Size Distribution
PTFE	Polytetrafluoroethylene
PXRD	Powder X-Ray Diffraction
RDF	Radial Distribution Function
ROY	5-methyl-2-[(2-nitrophenyl)amino]-3-thiophenecarbonitrile
SAM	Self Assembled Monolayers
SC-XRD	Single Crystal X-Ray Diffraction
SD	Standard Deviation
SEM	Scanning Electron Spectroscopy
SIE	Specific Interaction Energy
SN	Secondary Nucleation
THF	Tetrahydrofuran
UV-Vis	Ultraviolet-Visible light
XPS	X-Ray Photoelectron Spectroscopy

List of Symbols

(hkl)	Miller indices of a crystal facet
α, β, γ	Crystallographic angles
ΔG	Free energy change
ΔG_S	Surface free energy again
ΔG_V	Volume free energy loss

ΔG_{crit}	Free energy change for homogeneous nucleation
γ	Interfacial energy
γ_i	Activity coefficient of solute i
γ_i	Surface free energy of facet i
γ_i^*	Activity coefficient of solute i at equilibrium
λ	Wavelength (Å)
μ_i	Chemical potential of solute i
μ_i^*	Chemical potential of solute i at equilibrium
ν	Frequency of the X-rays (Hz) OR Volume of a single solute molecule OR Poisson's ratio of material
ϕ	Relative supersaturation
ρ	Density (g/m^3)
σ	Supersaturation
θ	Angle (°)
φ	Constant work function
A	Pre-exponential factor for homegeneous nucleation OR Projected contact area (nm^2)
a	Activity of solute i
a, b, c	Crystallographic axis
A_i	Total surface area of facet i
a_i^*	Activity of solute i at equilibrium
c	Concentration of solute in solution
c^*	Concentration of solute in solution at equilibrium
d_{hkl}	Interplanar spacing of facet (hkl)
E	Young's modulus
E_r	Reduced modulus (GPa)
$E_{att}(hkl)$	Attachment energy of facet (hkl)
$E_{binding}$	Binding energy of the electron (eV)
E_{cry}	Total energy of crystal layer

E_{cr}	Energy of crystal lattice
E_{int}	Interaction energy between crystal and solvent layers
$E_{kinetic}$	Kinetic energy of the emitted photoelectron (eV)
$E_{slice}(hkl)$	Energy released on the formation of growth slice of thickness d_{hkl}
E_{sol}	Total energy of solvent layer
E_{tot}	Total potential energy of simulated crystal-solvent layer
G	Growth rate of facet (hkl) or of a characteristic dimension
H	Hardness (GPa)
h	Planck's constant (Js)
h_c	Contact depth (nm)
J	Nucleation Rate
k_B	Boltzmann constant (1.381×10^{-23} J/K)
L	length of the characteristic dimension or the distance between the crystal centre and the facet (hkl)
M	Molar Mass (kg/mol)
m_{vdr}	Combined mass of solute and vial
m_{vs}	Combined mass of solution and vial
m_v	Mass of vial
n	Order of diffraction
N_A	Avogadro's constant (6.022×10^{23})
P_{max}	Maximum indentation load (mN)
R	Ideal gas constant 8.314 J/mol
r	Radius of the solute cluster in solution
r_c	Radius of critical cluster in solution
S	Supersaturation ratio OR Gradient of tangent of unloading curve
T	Temperature (K)
V_m	Molar volume
x	perpendicular distance between (010) and the topmost edge of the crystal

x_i	Mole fraction of solute i
x_i^*	Mole fraction of solute i at equilibrium
Length a	Characteristic crystal dimension perpendicular to facet (010)
Length b	Characteristic crystal dimension parallel to facet (010)

Chapter 1

Introduction

1.1 Background and Motivation

Active Pharmaceutical Ingredients (APIs) also known as 'drug substances' are crucial in pharmaceutical crystallisation as they are the components responsible for treating or preventing disease [25]. APIs range from common drugs like paracetamol and ibuprofen to therapeutic proteins for more severe conditions. The rise in chronic diseases has driven demand for drug research, with the API market forecast to grow by 60 billion USD by 2025 at a 6% Compound Annual Growth Rate (CAGR) [26, 27, 28]. However, pharmaceutical production is time and cost intensive, where the cost of a single batch can surpass £1 million [29], making advanced techniques like crystallisation essential for improving efficiency. Crystallisation is a ubiquitous process where molecules self-assemble into well-ordered, three-dimensional structures. The characteristics of crystals are largely influenced by the conditions under which crystallisation occurs, often leading to unexpected morphologies, shapes, and sizes. However they need to be of a certain size, shape, purity and structure before entering downstream processing [1]. Crystal attributes not only affect the performance of these processes – filtration, drying, milling etc., but also the final drug product qualities such as dissolution rate, shelf life, and bioavailability [30, 31]. With economic and regulatory pressures becoming increasingly stringent [32, 33],

immense emphasis is put on designing and controlling the crystallisation process so that any undesired crystal characteristics are avoided.

However, accurate prediction of crystal shape and size still remains a big challenge in pharmaceutical crystallisation. Mechanical breakage is a common occurrence in industrial crystallisers, yet a systematic study on crystal breakage and the consequent effect on crystal growth has never been reported. Micro breakage and attrition have been studied vastly as means of secondary nucleation, however, the repercussions of crystal fracture resulting in the 'death' of the large crystal and the consequent 'birth' of substantially sized crystals is unknown. In most cases, growth post breakage is assumed to be the same as before breakage either due to lack of understanding or for simplification purposes in process modelling [34].

In the pharmaceutical industry, the unique responses of crystals to external mechanical forces, such as 'self-healing' [35, 36, 37] and 'bending' [38, 39], are particularly intriguing. These phenomena can provide valuable insights into the crystal structure and enhance the performance of downstream processes like milling and tableting. Along similar lines of crystal abnormalities, this PhD reports and investigates a novel observation of crystal growth post breakage called 'crystal regeneration'. Here, paracetamol crystals broken along their cleavage plane regrew into their original shape prior to demonstrating growth like an unbroken crystal. These eccentricities have the potential of changing for the better or worse, the end crystal properties as well as their downstream performance. Considering that breakage along the cleavage plane is most probable when a crystal is under pressure [40], understanding the growth behaviour post cleavage is highly crucial to accurately predict the end crystal properties and improve their downstream processibility.

1.2 Aims of this PhD thesis

This PhD research aims to investigate the behaviour of organic crystals after breakage through systematic experiments involving the breakage and subsequent growth of single

crystals which have previously not been attempted. The primary focus will be on studying breakage along the cleavage planes of crystals to observe and report changes in crystal shape, size, and growth rates post-breakage. To achieve this overarching goal, four key objectives will be pursued:

1. Investigate in detail the recently reported 'crystal regeneration' phenomenon. With the aid of high quality images, crystal growth measurements, and characterisation techniques, propose a 'regeneration mechanism' applicable to organic crystals
2. Develop an experimental workflow utilizing automated imaging and image analysis to obtain precise growth rate measurements for deducing regeneration kinetics. This framework can then be applied to screen other crystal systems, demonstrating that regeneration is not limited to paracetamol alone
3. Investigate the effect of crystallisation conditions such as type of solvent, supersaturation ratio, and agitation, on regeneration as well as its implications on other crystallisation processes such a secondary nucleation. The goal is to highlight the significance in the behavioural differences between broken and whole crystals
4. Finally, propose hypothesis and mechanisms to explain the peculiar observations arising from the regeneration phenomenon and their deviations from the growth behaviour of crystals prior to breakage, inspiring further exploration into crystal breakage and growth

1.3 Thesis overview

This thesis consists of seven chapters in total with three main results chapters. Prior to the start of any technical content, a summary of my publications, attended conferences, and PhD achievements has been provided. The breakdown of the thesis is as follows:

- **Chapter 2: Literature review**

  This section encompasses all the relevant literature associated with the PhD topic

from the theory of crystallisation, thermodynamic and kinetic theories of growth, through to the mechanical properties of crystals. A review of the most current understanding of crystal breakage and growth as well peculiar behaviours in molecular crystals has been provided.

- **Chapter 3: Materials and Methods**

  Description of the general experimental set-ups as well as any computational methods and solid state characterisation techniques used, have been detailed in this chapter.

- **Chapter 4: Crystal regeneration - a proposed growth mechanism in crystals post breakage**

  The first results chapter introduces the regeneration phenomenon observed in crystals post breakage. The effect of crystal size, and extent and orientation of breakage has been investigated via evaporative crystallisation and optical microscopy.

- **Chapter 5: Design of isothermal crystallisation set-up with integrated macrophotography to investigate solvent effects on crystal regeneration**

  This chapter describes the developed workflow comprising of an isothermal crystallisation setup, a macrophotography rig, and MATLAB image analysis, to study the effect of solvents on crystal regeneration

- **Chapter 6: Effect of supersaturation and agitation on the regeneration rates of paracetamol crystals**

  Utilising the experimental set-up developed in the previous chapter, this section reports the facet specific growth rates during regeneration as a function of supersaturation and agitation. This section also addresses the anomalies in crystallisation kinetics resulting from regeneration.

- **Chapter 7: Conclusions and future work**

  Key findings and takeaways of this research have been summarised in this chapter. Ongoing work as well as some of the short term and long term plans associated with crystal regeneration have been detailed.

Chapter 2

Literature review

2.1 Crystallisation in the pharmaceutical industry

Crystallisation is the process of generating and isolating solid crystals from solution, melt, or directly from a gas phase by molecular self-assembly into well-defined and rigid lattices to minimise their energy state. Due to the ordered structure of crystalline materials, impurities or solvents are usually excluded, resulting in a pure product [41, 42]. This single-step separation and purification process is more efficient than traditional methods like chromatography, making crystallisation a key link between synthesis and downstream processing [30, 29]. Industries including food, pharmaceutical, and fine chemicals – dyes, pigments, explosives, implement crystallisation to different extents in their manufacturing process depending on their end product goal [43, 44, 45]. In the pharmaceutical industry specifically, crystallisation plays a crucial role in the development and manufacturing of drug substances.

Crystallisation is the primary method for purifying and producing solid APIs, influencing the physicochemical properties of drugs such as solubility, stability, and bioavailability [1]. The ability to control the crystallisation process is essential for ensuring the quality, efficacy, and safety of pharmaceutical products. The solid-state form of a drug, including its polymorphic and crystalline state, can have a significant impact on its therapeutic

performance [46]. For instance, different polymorphs of a drug may exhibit distinct solubility profiles, which can influence the rate and extent of drug absorption in the body [47].

The crystallisation process is highly sensitive to a range of factors, including temperature, solvent type, concentration, and the presence of impurities [48]. In pharmaceutical manufacturing, precise control of these parameters is critical to ensure consistent production of the desired crystal form with appropriate particle shape and size distributions, which in turn affects downstream processing such as filtration, drying, and tableting [49]. This chapter explores both the fundamental concepts and recent advancements in key areas of crystallisation, including solubility, nucleation, and crystal growth. It concludes with a summary of the current understanding of crystal breakage and post-breakage growth, alongside a detailed account of the solid-state properties of paracetamol that sets a scene for the results chapters to follow.

2.2 Fundamentals of crystallisation

2.2.1 Solubility

Phase diagram

Solubility is a fundamental thermodynamic variable that governs the crystallisation process and influences the mechanisms of nucleation and growth. Solubility can be defined as the maximum amount of a solid species that can completely dissolve in a certain amount of solvent at a given temperature and pressure. When this happens, the solution is said to be saturated and is in dynamic equilibrium with the solid phase.

Usually the temperature dependence on the solubility of a solute in a solvent or solvent mixture is represented graphically using a solubility curve. The work of Ostwald in 1897 and Miers and Isaac in 1906-1907 led to the development of a phase diagram for

crystallisation, a generalised version of which is shown in Figure 2.1.

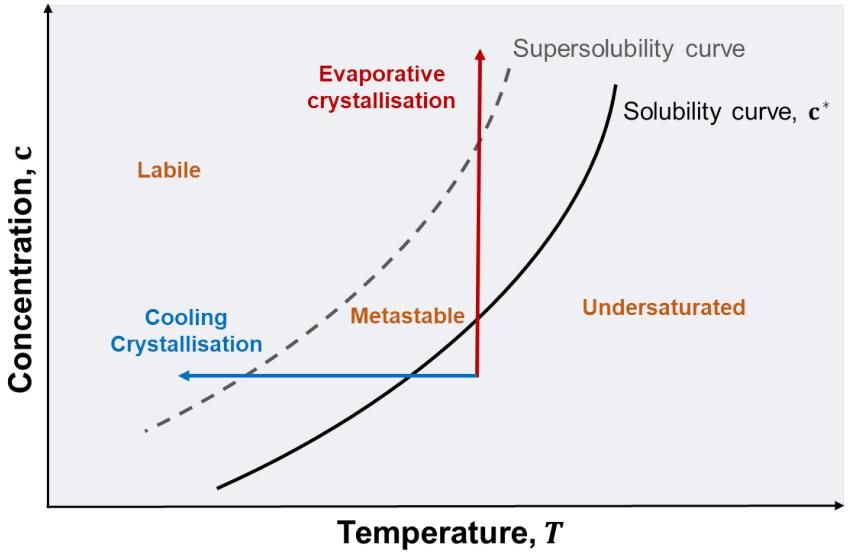


Figure 2.1: A generalised phase diagram showing the solubility curve and the three thermodynamically varied regions

As can be seen from the diagram, the curve above the solubility line is the 'supersolubility' curve, separating the 'metastable' region from the 'labile' region [50] - first reported by Mier and Isaac by studying the dependence of temperature on spontaneous crystallisation using refractive indices of the solution [51, 52]. With both, solubility and supersolubility showing a proportional relationship to temperature, the three regions on the diagram can be described as follows:

- *Stable region:* the region below the solubility line is the undersaturated zone where the energy barrier for crystallisation is high enough for no crystallisation to take place. Any amount of solid added in this region will instantly dissolve, as well as any pre-existing crystals will exhibit dissolution.

- *Metastable region:* This supersaturated zone between the solubility and supersolubility line is where, even though no spontaneous crystallisation takes place, already present crystals will grow. Crystallisation in this region is sought after as it provides adequate control over the process.

- *Labile region:* The supersaturated region above the supersolubility curve is the least

desired region for operation as it leads to spontaneous crystallisation due to a low energy barrier. Therefore there is a risk of 'run-away' crystallisation which cannot be controlled, giving undesired crystalline products.

Overall, crystallisation can only take place above the solubility line in the supersaturated region. There are various ways of achieving supersaturation; via evaporation of solvent (red line on Figure 2.1), cooling of the solution (blue line on Figure 2.1), as well as anti-solvent addition. Even though there is substantial understanding about the solubility curve, this is not the case with the metastable and labile region. This metastable limit or the Metastable Zone Width (MSZW); as shown on the diagram, is a kinetic entity and varies for a specific system depending on parameters including agitation, impurities, solution history, fluid dynamics etc., and thus difficult to determine [53, 54]. Current experimental methods of determining this region include polythermal ([51, 52]) methods, however due to the large uncertainties associated with this property and consequently the time consuming nature of these experiments, some theoretical models to predict the MSZW have also been developed [55]. Despite the complications of obtaining data on metastability, determining the MSZW and therefore controlling the supersaturation is always sought after as it has the potential to influence the thermodynamic and kinetic parameters of the entire crystallisation process.

Supersaturation

A solution is said to be supersaturated when the solute concentration at a given temperature surpasses its equilibrium concentration. As mentioned above, supersaturation, σ, is the driving force for crystallisation and is essentially derived from the difference in the chemical potential of the solute species, i, [56]:

$$\sigma = \frac{\mu_i - \mu_i^*}{RT} = \frac{[\mu_{(aq)}^0(T) + RT\ln(a_i)] - [\mu_{(aq)}^0(T) + RT\ln(a_i^*)]}{RT} = \ln\left(\frac{a_i}{a_i^*}\right) \qquad (2.1)$$

Where μ_i is the chemical potential of the solute species, μ_i^* is the chemical potential of the solute species at equilibrium, $\mu_{(aq)}^0$ is an arbitrary reference state chemical potential, R is the gas constant, and T is temperature. Moreover, a_i and a_i^* is the activity of the solute at supersaturation and at equilibrium respectively. As activity is a function of the activity coefficient, γ_i, and the mole fraction of the solute in solution, x_i, the dimensionless eq.2.1 can be rewritten as:

$$\sigma = \ln\left(\frac{\gamma_i x_i}{\gamma_i^* x_i^*}\right) \tag{2.2}$$

Under the assumption of an ideal solution where $\gamma_i = \gamma_i^* = 1$ the following definition of supersaturation is obtained:

$$\sigma = \ln\left(\frac{x_i}{x_i^*}\right) \tag{2.3}$$

Generally, the dimensionless chemical potential difference is approximated using a dimensionless concentration difference and the following expression is used to display the relative supersaturation, ϕ [57, 48]:

$$\phi = \frac{\Delta c}{c^*} = S - 1 \tag{2.4}$$

Where, Δc is the concentration difference and S is the supersaturation ratio, defined as:

$$\Delta c = c - c^* \tag{2.5}$$

$$S = \frac{c}{c^*} \tag{2.6}$$

Where, c is the concentration and c^* is the concentration at equilibrium

2.2.2 Nucleation

Nucleation is the onset of crystallisation i.e. the 'birth' of a new phase from the bulk phase that eventually develop into ordered crystalline solids. This process can be categorised into two groups, primary and secondary as seen in diagram 2.2. The major difference between them is that in primary nucleation nuclei are formed directly from solution without

the presence of a previously formed crystal, whereas, in secondary nucleation, crystals of the same solute species induce nucleation. To classify further, primary nucleation, can be homogeneous or heterogeneous. When the supersaturation of the system itself drives the formation of nuclei in a crystal free solution, it is termed as homogeneous nucleation. Conversely, the surface of foreign substances such as dust, crystalliser walls and other solid impurities act as an active site for nuclei formation leading to heterogeneous nucleation. MSZW and Induction time, t_{ind} are the most common ways of determining the onset of nucleation in a crystalliser. MSZW is measured during polythermal experiments and is the temperature range or the time, t_{MSZW} between the solution reaching saturation and the first appearance of crystals. Whereas t_{ind} is measured under isothermal conditions as the time taken from the solution reaching constant temperature until nucleation being detected [58].

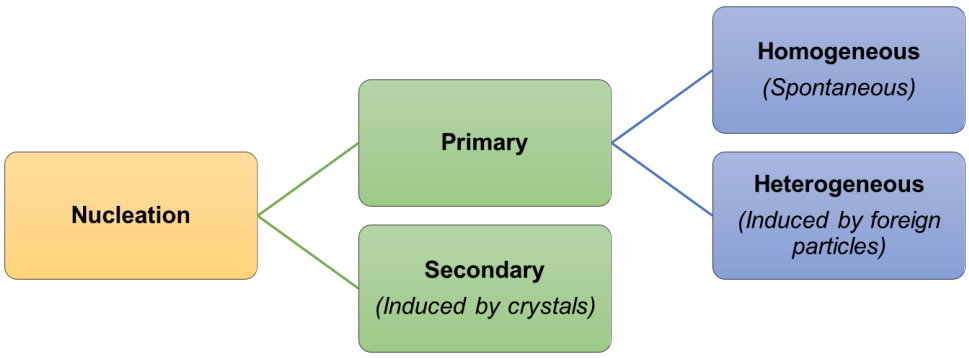


Figure 2.2: A schematic of the major categories of nucleation processes

Primary Homogeneous Nucleation

The Classical Nucleation Theory (CNT) is the most elementary and widely used theory describing homogeneous nucleation. It was first developed to understand the condensation of vapour into a liquid droplet but over the years is has been treated analogous to the generation of crystals from solutions [59, 60]. The fundamental idea of CNT is the creation of solute molecule 'clusters' in a supersaturated solution which eventually grow into nuclei after reaching a minimum size required for stability.

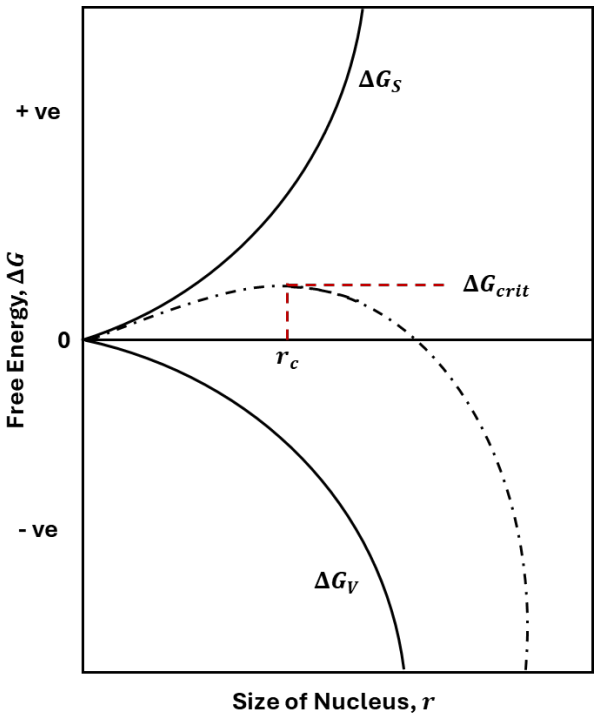


Figure 2.3: Free energy diagram for the nucleation process as a function of the nuclei radius

Gibbs formulated this theory into a thermodynamic explanation using the following equation [59, 61, 62]:

$$\Delta G = \Delta G_S + \Delta G_V = 4\pi r^2\gamma - \frac{4}{3}\pi r^3 \Delta G_\nu \tag{2.7}$$

which states that the Gibbs free energy change, ΔG, associated with the formation of a cluster in solution is the sum of two quantities; the surface free energy gain, ΔG_S, resulting from the formation of a new surface and the volume free energy loss, ΔG_V, resulting from the creation of a new solid phase which is inherently more stable than the supersaturated solution. Here ΔG_S is dependent on the cluster radius, r, and the interfacial tension between the cluster surface and solution, γ.

Equation 2.7 can be visually represented as seen in diagram 2.3 [60]. It can be seen that only after the radius of the cluster reaches a critical size, r_c, does the free energy of the system become negative i.e the system becomes stable and nuclei growth becomes energetically favourable. As ΔG passes through a maximum at r_c, this critical radius can

be found by making $d\Delta G/dr = 0$:

$$\frac{d\Delta G}{dr} = 8\pi r\gamma - 4\pi r^2 \Delta G_\nu r_c = 0 \Longrightarrow r_c = \frac{-2\gamma}{\Delta G_\nu} \tag{2.8}$$

Hence, using Equations 2.7 and 2.8, ΔG_{crit}, gibbs free energy at r_c can be found:

$$\Delta G_{crit} = \frac{4}{3}\pi r_c^2 \gamma \tag{2.9}$$

The Gibbs-Thompson equation originally developed for a liquid-vapour system in the late 1800s was later applied to crystallisation systems by Ostwald and Freundlich separately in the early 1900s to express the growth of the nuclei clusters [63]:

$$\ln \frac{c}{c^*} = \ln(S) = \frac{2M\gamma}{RT\rho r} \tag{2.10}$$

Where, M is the molar mass and ρ is the density. The above equation (Equation 2.10) highlights the dependence of the particle size, r, on the supersaturation, S, of the solution where at higher supersaturations the critical radius is smaller due to smaller energy barriers compared to at lower supersaturations. This underpins the phenomena of 'Ostwald ripening'. At low supersaturations, S approaching 1, there will be many particles smaller than the critical radius, as r_c is large. Hence they will dissolve whilst those larger than the r_c will eventually come together to form one, single large particle [64]. As Ostwald ripening takes place at low supersaturations, meaning a lower driving force, it takes place very slowly; on a scale of days to months [64].

Equation 2.10 can be rearranged in terms of r (Equation 2.11) and substituted into Equation 2.9 to obtain the critical Gibbs free energy with respect to the solution concentration (Equation 2.12):

$$r = \frac{2M\gamma}{RT\rho \ln(S)} \tag{2.11}$$

$$\Delta G_{crit} = \frac{16}{3}\pi\gamma^3 \left(\frac{M}{RT\rho \ln S}\right)^2 \tag{2.12}$$

In 1926 Volmer and Weber first came up with a kinetic theory for CNT which was developed through the years to ultimately show that the nucleation rate, J, which is the number of nuclei formed per unit time per unit volume, can be expressed in an Arrhenius form [60, 61, 65]:

$$J = A \exp\left(-\frac{\Delta G_{crit}}{k_B T}\right) \tag{2.13}$$

Where A is the pre-exponential term which depends on the rate of attachment of molecules to the cluster [60], and k_B is the Boltzmann constant. Using Equation 2.12, this can be written as:

$$J = A \exp\left(-\frac{16\pi\gamma^3 M^2}{3R^2 k_B T^3 \rho^2 \ln^2(S)}\right) \tag{2.14}$$

As $R = k_B N_A$, where N_A is the Avogadro's constant, $M/\rho = V_m$, where V_m is the molar volume, and $\nu = V_m/N_A$, where ν is the volume of a single molecule, the above equation can be simplified further and a final equation for CNT can be written as:

$$J = A \exp\left(-\frac{16\pi\gamma^3 \nu^2}{3k_B^3 T^3 \ln^2(S)}\right) \tag{2.15}$$

Though widely used, CNT is based on major assumptions [30, 60]:

- The clusters are treated as spherical and the dependence of surface curvature on interfacial tension is neglected
- The clusters grow by the attachment of one monomer at a time, in a ordered manner, resulting in the same molecular arrangement as the resulting crystal

- The clusters are stationary and the nucleation rate assumes steady state kinetics.

The assumptions and simplicity of CNT limit its use in more complex systems as it does not take into consideration the entire picture. Hence, Non-classical Crystallisation (NCC) theories have been gaining traction over the years. These are based on density fluctuations in the solution resulting in molecular precursors that are larger than the building blocks/monomers in CNT [66]. NCC includes mechanisms such as the two-step nucleation theory [67, 30], and the pre-nucleation cluster theory [68]. Details of the non-classical nucleation pathways will not be discussed here are they lie outside the scope of this thesis.

Primary Heterogeneous Nucleation

Although spontaneous homogeneous nucleation is conceptually straightforward, it requires high supersaturations such that the thermodynamic energy barrier for nucleation is low, making it difficult to control. The excessive supersaturations can lead to 'runaway' crystallisation with imperfect final crystals, sustaining impurities and defects. Hence, heterogeneous nucleation, inducing nucleation using foreign species in solution, is sought after. Theoretically, solid impurities like dust particles, crystalliser walls etc., also act as hetero nucleants, lowering the energy barrier for nucleation. These substances are inevitably present in the system, therefore achieving 100% homogeneous nucleation, although assumed, is rarely possible. Having said that, in the past 2-3 decades, the effect of various heterosurfaces, known as 'templates', on the nucleation behaviour of APIs have been widely studied. They have been shown to not only to speed up nucleation kinetics [2, 4] but also selectively nucleate the desired API polymorph [69, 5]. As the solute molecules aggregate on the heterosurface and form stable nuclei at the solid-liquid interface, the specific interactions between the solute and the template surface is a crucial parameter to investigate [70]. These interactions are mainly governed by the surface topography, epitaxy, and surface chemistry of the templates being used [71].

Heterogeneous nucleation via epitaxy occurs via lattice matching such that there is a degree of similarity between the molecular arrangement of the template surface and the crystal structure of the solute of interest [72]. These favourable epitaxial interactions reduce the interfacial energy required for nuclei formation, hence reducing the induction time for the desired crystalline product. Various studies have shown that the matching of the three-dimensional (3D) molecular arrangement of the solute and substrate have resulted in favourable nucleation outcomes [73, 74, 75, 76], however increasing number of studies have shown the success of two-dimensional (2D) interfaces, and Ledge directed epitaxy (LDE). A popular 2D interface are self assembled monolayers (SAMs) of the solute of interest. In the case of entacapone [77], used to treat Parkinson's disease, as well as 1,3-bis(*m*-nitrophenyl) urea [78], SAMs assembled on a gold surface led to the selective nucleation of the desired polymorph. Ledge directed epitaxy (LDE), a variation of 2D epitaxy, is the matching between the dihedral angles of the nucleating crystal structure and the defect of the template surface, developed by Ward and co-workers [79].

More recently the effect of functional group matching and surface topography have been more promising. Multiple studies have shown that hydrogen bonding between the substrate and the solute, along with the extended lifetime of the bond is crucial for solute molecule adsorption and the creation of stable nuclei on the hetero surface. E.g., the acceleration of paracetamol nucleation due to hydrogen bond complimentarity between paracetamol and graphite hetero surface [4], and the use of microcrystalline cellulose (MCC) as a template for inducing heterogeneous nucleation in five of the seven APIs tested [80, 3]. In terms of topography, pore sizes and shapes of the polymer templates have been shown to selectively nucleate the desired crystalline product. Whilst 5-methyl-2-[(2-nitrophenyl)amino]-3-thiophenecarbonitrile (ROY) preferentially crystallised in the pores of porous glass template with smaller pore size [81], Aspirin showed preferred nucleation in hexagonal shaped pores of polymers rather than any other geometry [2].

To summarise, a hetero template could be any material from the likes of organic crystals [4, 5], inorganic crystals [82] [3], polymers [2], porous silica [83], porous glass [81], SAMs

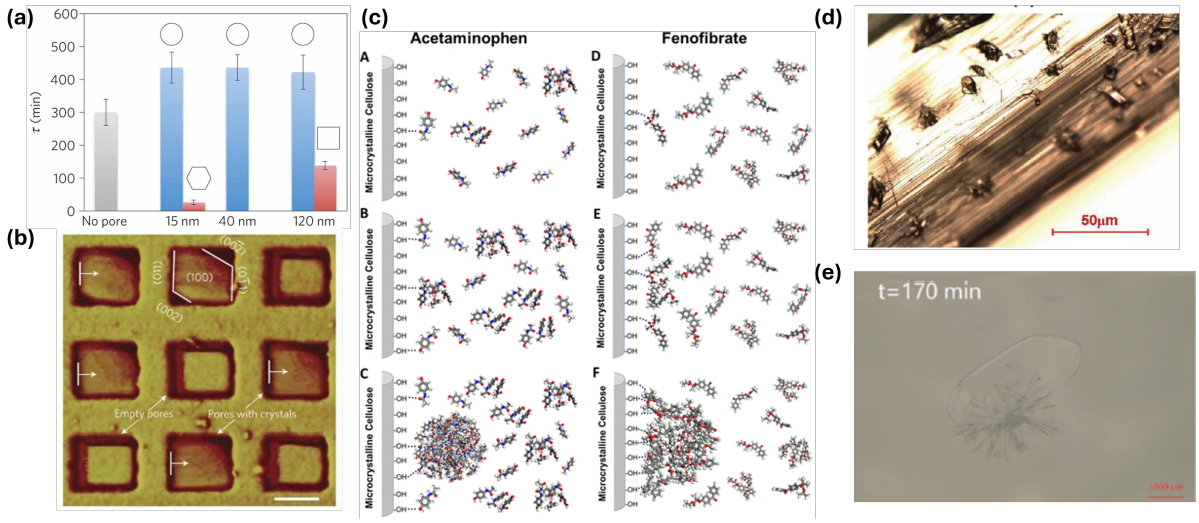


Figure 2.4: (a) induction time data showing preferred nucleation in the hexagonal pores of polymer films (b) Aspirin crystals nucleated inside the square pores due to favourable interactions at the pore angles. (a) and (b) adapted with permission from [2] (c) Molecular dynamic simulations showing cluster formation of paracetamol and fenofibrate molecules of MCC surface due to hydrogen bonding. Figure adapted with permission from [3] (d) paracetamol crystals nucleating on D-mannitol crystal and (e) pimelic acid crystals nucleating on malonamide single crystal. Images obtained with permission from [4] and [5] respectively

[77, 78] etc. (Figure 2.4) . As long as these surfaces enable favourable interactions, epitaxial and/or chemical, with the crystal structure of the desired solute, heterogeneous nucleation has been seen to be successful. The way in which a heterosurface is introduced to a crystallisation cocktail is via 'seeding' which will be discussed in detail in Section 2.2.2.

Secondary Nucleation

Secondary nucleation (SN) is the generation of nuclei in the presence of the parent crystal of the solute in solution [84]. As seen previously, nucleation is the interplay between the free energy gain from formation of a new surface and the free energy loss due to creation of solid phase in solution. Due to the already present crystal surface, the energy required for the creation of a solid-liquid interface is lower, thus allowing secondary nucleation to occur at lower supersaturation compared to primary nucleation, consequently enhancing crystallisation control. The readers are directed to the secondary nucleation reviews for

a detailed account on the process [85, 86, 6] however to summarise, the following are the main routes of SN identified with consensus across the literature (Figure 2.5 (left)):

- **Nucleation from parent crystal**

  1. *Needle/dendritic breeding and Attrition*

     At very high supersaturations, needles (dendrites) grow on the crystal surface and shear away into the solution [87]. Industrial crystallisers do not normally operate at such high supersaturation and thus this phenomenon rarely occurs. Under attrition, impact forces such as crystal-crystal (CC), crystal-wall(CW), and crystal-impeller (CI) interactions can also chip away fragments from the crystal which then grow into bigger crystals [88]. Since these two mechanisms result in particles bigger than the average nuclei, it is debated whether they classify as a SN mechanisms. Moreover, the high collision energy leads to considerable lattice strain in parent crystals, leading to growth rate dispersion [86].

  2. *Contact nucleation/microattrition*

     High fluid shear and/or CC, CW, and CI interactions occurring at minimal collision energy result in microattition or contact nucleation [89]. This form of SN causes minimal damage to the parent crystal and produces fines that are in the size range of nuclei. These fines on the parent crystal surface get displaced into the solution due to fluid motion or by contact, which then grow into individual crystals [84].

- **Nucleation from solute layer**

  1. *Embryo Coagulation Secondary Nucleation (ECSN)*

     In this mechanism first discovered by Qian and Botsaris in 1997 [90], solute/prenucleation clusters in the solution move towards the parent crystal via Van der Waals attractive forces. When concentration of these clusters or 'embryos' increases within the boundary layer, they rapidly coagulate and

form nuclei of critical size, which are washed away into the bulk solution by fluid shear stress and contact nucleation [91].

2. *Surface nuclei breeding*

   Prenucleation clusters from solution come into contact with the surface of the crystal, which facilitates the formation of stable nuclei. These nuclei are weakly bound to the surface and hence, as with the previous cases, are washed away by fluid motion or weak contact forces (Figure 2.5 (middle)). Recently, this mechanism has been proposed as the route for secondary nucleation in several studies, including the crystallisation of paracetamol and glycine [7, 92, 93].

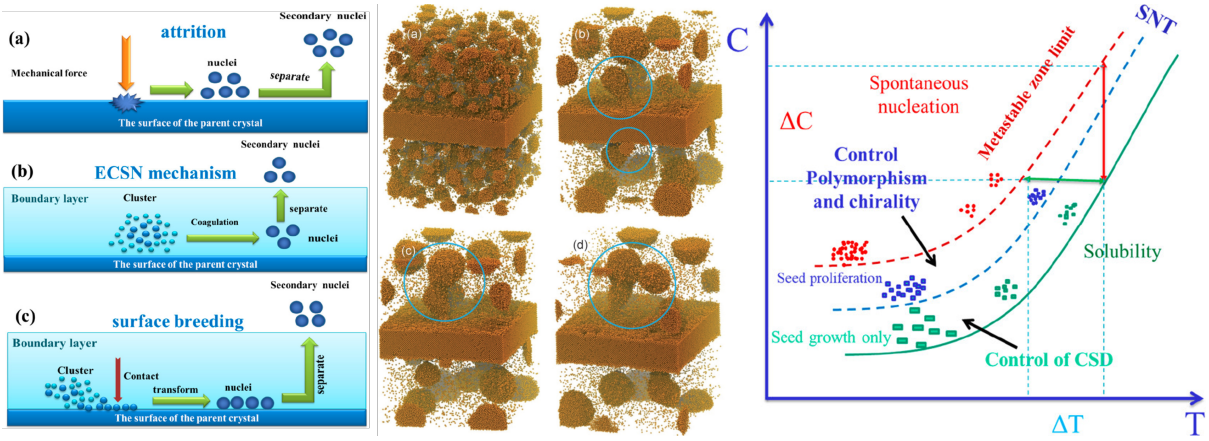


Figure 2.5: Left: Main mechanisms of secondary nucleation, obtained with permission from [6] Middle: Surface nuclei breeding mechanism shown via molecular dynamic simulations at moderate supersaturation, obtained with permission from [7] Right: Updated phase diagram depicting the secondary nucleation threshold for seeded systems, highlighting the seed growth only and seed proliferation zones, obtained with permission from [6]

The rate of SN, B_N, is normally expressed as an empirical relationship [1]:

$$B_N = k_{n,s} N_i^j M_T^k \sigma^b \tag{2.16}$$

Where $k_{n,s}$ is the empirical SN rate constant, M_T, N_i and σ are the suspension density, impeller speed and supersaturation respectively, and j, k, b are empirical constants. Although Equation 2.2.2 is widely used, several other ways are used for expressing SN depending on the specific mechanism. These include power law models for contact SN [94], mechanistic models for collision-induced SN [95], and surface nucleation models [6].

Seeding

Seeding is the process of adding crystals of the crystallising species or a heterogeneous entity to a crystallisation solution to create more crystals. Seeding is commonly employed to provide better control of the batch crystallisation process and impacts the final Crystal Size Distribution (CSD) depending on the amount of seeds added (seed loading), time of seeding and size, shape and chemistry of the seeds itself [24, 96, 97]. Seeding is often regarded as an art [98], and the specific technique employed can significantly impact the final product's quality, including yield, size, and polymorphism. For example, dry or wet addition can affect the final CSD depending on the hydrophilicity of the seeds, with hydrophobic seeds being more prone to agglomeration [97].

In the case of homogeneous or solute crystals, seeds are typically introduced within the metastable zone to prevent secondary nucleation while promoting seed growth. A 'secondary nucleation threshold' (SNT) (Figure 2.5 (right)) lies between the solubility curve and the supersolubility curve. Below this threshold, only seed growth is observed; above it, seed proliferation occurs [99, 92]. To accurately measure SNTs, single crystal seeding strategies have been employed in addition to traditional batch crystallisation techniques. Here the delay time, t_d, time between crystal addition and moment the suspension density increases, was used to determine the SNT. It has been observed that smaller seeds and lower supersaturation led to a larger delay time and also lower SN rates (low suspension density per unit time) [100, 93].

2.3 Crystal Growth

2.3.1 The crystal structure

Crystals are three-dimensional solids formed by periodically repeating units of atoms, ions, or molecules. The crystal lattice, or 'point lattice', consists of regularly spaced points, each with an identical surrounding environment. Organic crystals are composed

of repeating molecular units held together by intermolecular forces, which are weaker than the intramolecular forces within molecules. These forces, such as hydrogen bonding or dipole-dipole interactions, depend on the molecule's properties [101] and influence how the molecules are packed, determining the crystal's structure.

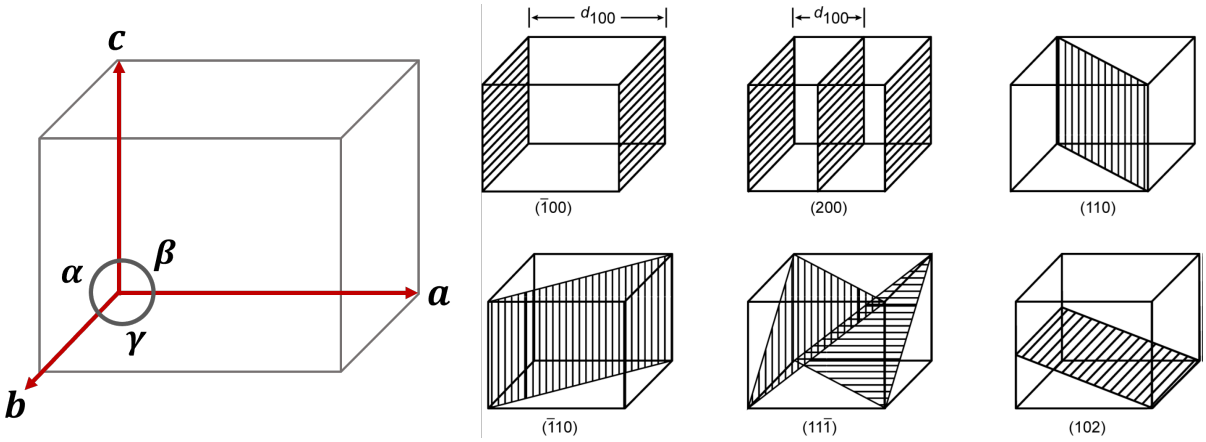


Figure 2.6: Left: Typical unit cell, Right: Example of miller indices based on a typical unit cell, obtained with permission from [1]

The repeating unit, also known as a 'unit cell' can be constructed using 'lattice parameters', which are three dimensions, a, b, c and three angles, α, β, γ, as shown in Figure 2.6. Bravais in 1848 showed that only 14 point lattices can be constructed which can be divided into 7 categories known as 'crystal systems' [48, 1]. These crystal systems are characterised using unit cell dimensions and are highlighted in Table 2.1. Depending on whether the Bravais lattice is 'simple', 'face centred', 'base centred' or 'body centred' it can be determined whether the unit cell has one lattice point i.e. a 'primitive' lattice, or multiple lattice points i.e. a 'non-primitive' lattice. Simple lattices are primitive whereas face centred, body centred and base centred lattices are non-primitive as they have lattice points present at the centre of the faces, centre of the overall unit cell and centre of the top and bottom faces respectively.

The crystal system can also have 'symmetry', either by reflection, rotation, inversion or rotation-inversion. This means that if the lattice undergoes the above movements, it will superimpose over itself. Each system has its unique way of achieving symmetry and hence, this can be used as a distinction technique between different systems [102].

Table 2.1: The 7 crystal systems and 14 Bravais lattices [1]

System	Axial lengths and angles	Bravais lattice
Cubic	Three equal axes at right angles $a = b = c$ $\alpha = \beta = \gamma = 90^\circ$	Simple Body centred Face centred
Tetragonal	Three axes at right angles, two equal angles $a = b \neq c$ $\alpha = \beta = \gamma = 90^\circ$	Simple Body centred
Orthorhombic	Three unequal axes at right angles $a \neq b \neq c$ $\alpha = \beta = \gamma = 90^\circ$	Simple Body centred Base centred Face centred
Rhombohedral	Three equal axes, equally inclined $a = b = c$ $\alpha = \beta = \gamma \neq 90^\circ$	Simple Body centred
Hexagonal	Two equal coplanar axes at 120°, third axis at right angles $a = b \neq c$ $\alpha = \beta = 90^\circ$ $\gamma = 120^\circ$	Simple
Monoclinic	Three unequal axes, one pair not at right angles $a \neq b \neq c$ $\alpha = \gamma = 90^\circ \neq beta$	Simple Base centred
Triclinic	Three unequal axes, unequally inclined, and none at right angles $a \neq b \neq c$ $\alpha \neq \beta \neq \gamma \neq 90^\circ$	Simple

Miller Indices

The three axes of the unit cell, a, b, c, are used to identify and name the faces of the crystals using a convention known as 'Miller indices' (Figure 2.6), denoted (hkl) [48, 103, 62]. Taking a point on the lattice as the origin for the axes, facets will intersect the axes at various distances, n_i. These indices are calculated by taking the reciprocal of the intersections and then rounding to the lowest integer while maintaining the ratio (Equation 2.17). For example, if a plane intercepts the a axis at $a/1$, and b axis at $b/2$, and does not intercept the c axis, then the facet will be (120).

$$h : k : l = \frac{1}{n_a} : \frac{1}{n_b} : \frac{1}{n_c} \tag{2.17}$$

The miller indices for a particular facet of a crystal remains constant irrespective of the crystal size [62]. Moreover, as (hkl) is a plane, if the facet intercepts a negative axis e.g., $-b$, it is denoted by adding an overbar in the notation, $(h\bar{k}l)$ [48]. Whilst round brackets are used to denote a specific plane, planes related by symmetry are denoted with 'curly' brackets, $\{hkl\}$. For example, (010), (100), (001), and their negative counterparts belong to the same family of planes, $\{100\}$, because their indices depend only on the way the unit cell axes are defined [48]. Moreover, when referring to specific directions in a crystal, the vectors are denoted by square brackets, $[hkl]$. For example, (010) and (020) are both part of the [010] direction, and the symmetry equivalent $< 100 >$ set of directions.

2.3.2 Polymorphism

Molecular solids can either exhibit amorphous or crystalline properties (Figure 2.7). In the crystalline state, they may exist as single-component crystals or multicomponent crystals, such as cocrystals, solvates, or hydrates. Hydrates and solvates consist of a 'host' molecule (e.g., the API in pharmaceuticals) and a 'guest' (water or solvent), where the guest may either integrate into the crystal structure or simply occupy space within

it [104]. Cocrystals, by contrast, are defined as 'solids that are crystalline, single-phase materials composed of two or more different molecular and/or ionic compounds, typically in a stoichiometric ratio' [8]. While the classification and nomenclature of these solids are widely debated [8, 105], this thesis will focus on single-component crystals. However, polymorphism—where a solid can exhibit different crystal structures due to variations in molecular arrangement—can occur in any of these crystalline forms.

Predicting and controlling polymorphism is crucial for APIs, as different forms can exhibit varied physical properties, such as stability and solubility, as well as differences in processability, including flowability and compressibility. Additionally, polymorphs can affect drug delivery, with some forms potentially leading to reduced bioavailability [106, 107, 108]. An example is the AIDS drug Ritonavir from the late 90s. While Form I was stable and safe, the sudden appearance of Form II in capsules reduced its dissolution rate in the body [109]. Many other APIs such as Paracetamol [19], Aspirin, Atorvastatin, Axitinib, Citric acid [110], L-Glutamic acid [108] etc., exhibit polymorphism with varying effects on their end goal.

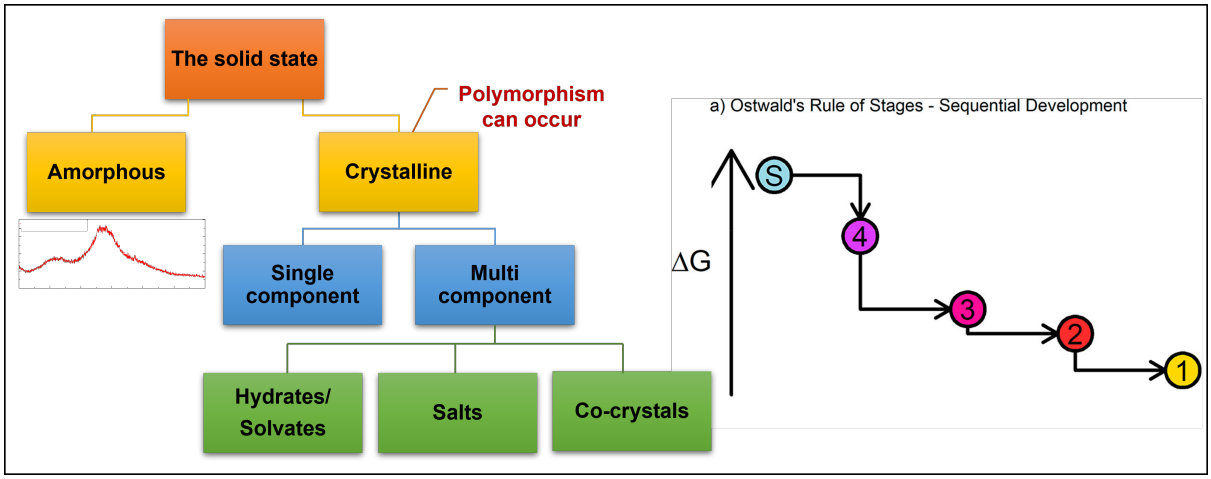


Figure 2.7: Left: simplified breakdown of the solid phase, adapted from [8] Right: Schematic of the Ostwald's rule of stages, depicting the journey from solution (S), to phase 4 (least stable),3,2, and 1 (most stable), image taken with permission from [9]

The reason why polymorphs are seen can be understood using a theory of 'Rule of Stages', proposed by Ostwald in 1897 (Figure 2.7). According to this, the Gibbs free energy of a crystallising system decreases in 'steps' from an initial stage of high-energy to equilibrium.

These steps arise from local minima, which are essentially the points where polymorphs are created. So the most unstable polymorph is crystallised out of the solution first followed by the metastable polymorph and finally the most stable polymorph is formed as the system reaches its lowest energy state [111, 112, 106]. Though this is the most widely used theory, there has been no general proof of its validity [9].

2.3.3 Crystal morphology

Morphology defines the inherent and unique set of crystal faces, resulting from the crystals' internal structure. When particle formation occurs slowly enough to allow the facets to reach equilibrium, the resulting morphology is governed by thermodynamics, and is known as the *equilibrium morphology* [12]. However, when growth proceeds more rapidly than the particle can adjust its shape, growth kinetics dictate the particle's morphology, and the stable shape that forms during growth is labelled as the *growth morphology* or *steady-state morphology* or *crystal habit* [12]. Growth morphology is the geometric appearance of the crystal, such as needle-like, plate-like, tabular, prismatic, spherical etc. [113, 114].

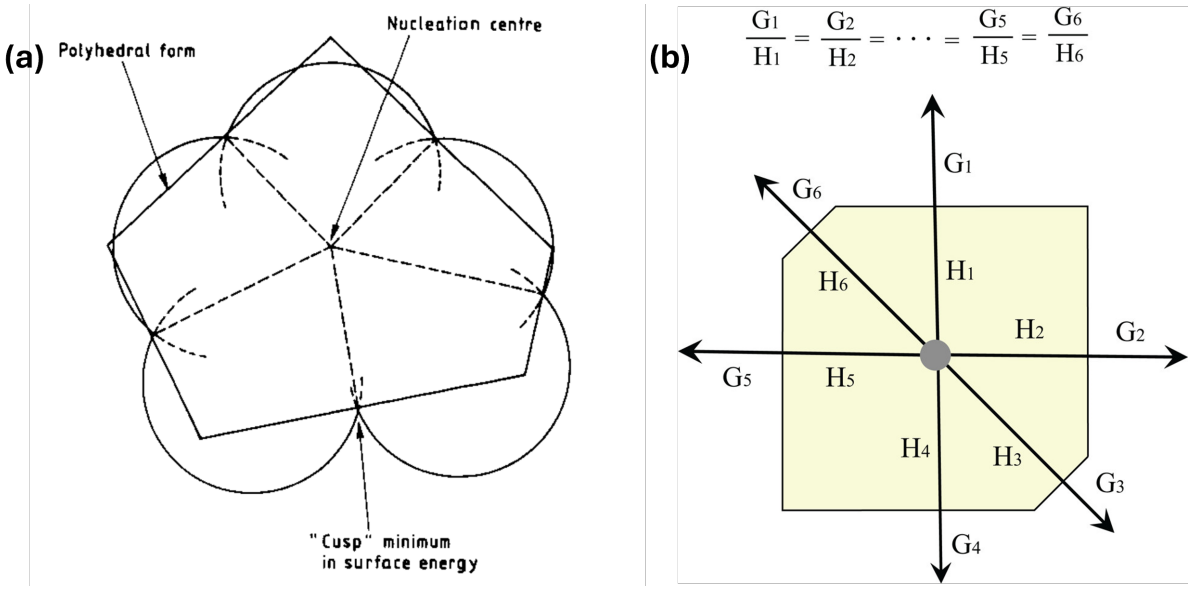


Figure 2.8: (a) Wulff construction, obtained with permission from [10], (b) Diagram showing the Frank-Chernov condition, used with permission from [11]

Equilibrium morphology

The earliest understanding of crystal morphology was shown by Gibbs and Wulff where Gibbs in 1875 postulated that the equilibrium morphology of a crystalline solid in contact with a fluid, at any given volume, will minimise its overall surface tension [115, 10, 116]:

$$\sum_{i=1,n} \gamma_i A_i = \text{minimum} \tag{2.18}$$

Where, n is the number of facets, γ_i and A_i, are the facet specific surface tension and total surface area of the ith face. Wulff in 1901 proposed a geometric construction, the 'Wulff plot' (Figure 2.8(a)), fulfilling the Gibbs condition, which shows that the distance, H_i, of a given facet from the growth origin (centre) of the crystal will be directly proportional to γ_i [117, 10, 116]:

$$\frac{\gamma_i}{H_i} = \text{constant} \tag{2.19}$$

The Gibbs-Wulff theorem however, does no hold true for crystals grown in a multicomponent liquid phase, i.e., solution, as thermodynamic control is unlikely [115], and also lacks solid experimental evidence for organic crystals [118, 116].

Growth morphology

The morphology of solution-grown crystals is determined by kinetics, such that the steady-state morphology will be dominated by the slow growing facets. This is because in a solution environment, the attachment of growth units onto the crystal surface defines the particle shape rather than the surface tension. Frank and Chernov described this growth morphology using an equation analogous to Gibbs' formulation [49, 119, 120]:

$$\frac{G_i}{H_i} = \text{constant} \tag{2.20}$$

Where G_i is the growth rate of facet i, and H_i is the distance of a given facet, i, from the growth origin (centre) of the crystal (Figure 2.8(b)). This model is based on an

assumption that the crystal remains faceted throughout the growth process.

2.3.4 Morphology prediction theories

As early as the 20th century, molecular structure of crystals has been used to predict their growth morphology. The widely used Bravais-Freidel-Donnay-Harkar (BFDH) theory proposed that the growth rate of a crystal facet (hkl), G_{hkl}, is inversely proportional to the d-spacing (interplanar spacing), d_{hkl}; thus, faces with the slowest growth rate will occupy the largest surface area on the crystal (high morphological importance) [10, 118, 121].

Hartman and Perdock [122, 123] proposed the Attachment Energy (AE) model, based on the understanding that crystals are anisotropic and contain Periodic Bond Chains (PBC). If a facet has a combination of weak and strong bonds in the PBC, then the growth rate will be controlled by the weakest bonds [10, 122], such that the slowest growing facet will have the highest morphological importance. AE is the bond energy released when a growth slice attaches onto the crystal surface.

$$E_{att}(hkl) = E_{cr} - E_{slice} \tag{2.21}$$

Where, E_{cr} is the energy of the crystal lattice and E_{slice} is the energy released when a growth slice of thickness d_{hkl} is formed. E_{cr} is found by summing the intermolecular interactions between the central molecule and all its surrounding ones in a crystal [10] and is constant for each face [118]. Two simplifications were introduced, where it was shown that the AE of a facet, $E_{att}(hkl)$, can be used as a proxy for the facet specific surface tension, γ, and E_{att} is directly proportional to the facet specific growth rate, G_i. AE models blur the distinction between equilibrium and growth morphologies by considering both arguments. In AE methods, the Frank-Chernov and Gibbs-Wulff conditions result in the same crystal morphology.

BFDH and AE morphologies are calculated under the assumption of a vacuum system.

They do not take into account external factors such as solvent effects, presence of impurities, and supersaturation and therefore do not tell the complete story of the facet [124]. Modified Attachment Energies (MAE) have been introduced that consider the solvent binding energy, E_s onto facet (hkl) by using the following correction [125, 126]:

$$E_{att,m}(hkl) = E_{att}(hkl) - E_s(hkl) \tag{2.22}$$

Molecular Dynamic (MD) simulations have been gaining traction for the molecular level understanding of the growth/dissolution process at the crystal surface, and work by solving the Newtonian equations of motion between interacting atoms [12]. MD simulations, with appropriate initial and boundary conditions and an interatomic potential that reflects the relevant physics, have demonstrated the ability to characterise the thermodynamics, kinetics, mechanisms, and final growth morphology of crystals like urea [127, 128], and calcite [129], even in the presence of external factors.

2.3.5 Growth mechanism and mechanistic models

The growth rate refers to the speed at which the crystal-liquid interface advances and is fundamentally determined by the mechanism through which growth units are incorporated into the crystal lattice. During crystal growth the following transport processes take place in series and usually the slowest of them is the rate determining step [130, 131]:

1. *Bulk Diffusion:*

   Movement of solute molecules through the boundary layer between the solid-liquid interface and the bulk solution via diffusion.

2. *Surface Integration:*

   Adsorption of solute molecules onto the crystal surface, followed by surface diffusion to the nearest kink site, followed by eventual integration into crystal lattice.

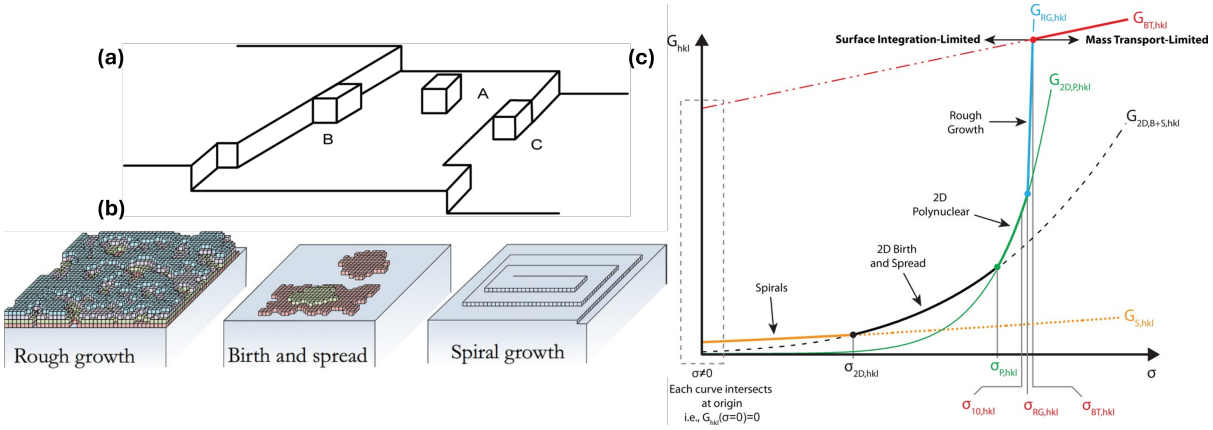


Figure 2.9: (a) Three possible sites on a crystal surface for growth unit incorporation; A: terrace, B: ledge, C: Kink, (b) The three growth regimes, rough growth, 2D nucleation, and spiral growth, (c) Diagram depicting the change in growth regimes with supersaturation. All images have been obtained with permission from [1, 12, 13] respectively.

As seen from Figure 2.9(a), there are three possible sites for the molecules to incorporate on a crystal surface: terrace (A), ledge (B), and kink (C). However, a kink site (C) is sterically and energetically the most favourable position of incorporation as it has the maximum number of neighbouring entities [1]. Therefore, growth on crystal surface occurs due to the presence of 'kink' sites. Any surface above 0 K will have kink sites [49, 132], however their density is dependent on the surface temperature and number of Periodic Bond Chains (PBCs) present, which are uninterrupted chains of bonds. Facets have been classified into 3 types depending on the number of PBCs they contain [122]:

- F-Faces: Flat and stable faces with two or more PBCs
- S-Faces: Stepped faces with one PBC
- K-Faces: Kinked faces with no PBCs

Diffusion limited growth

If the growth is diffusion limited, it either means that the mass transfer is very slow or the surface integration step is very fast. In the former case, solution hydrodynamics will affect the growth rate and faster mass transfer will mean faster growth rates. Rapid

surface integration is mainly dominating on S and K facets due to the abundance of kink sites, especially at higher supersaturation, thus solute molecules can attach onto the surface with ease in any orientation [49], hence also known as continuous or rough growth (Figure 2.9(b)). Due to a lack of control, this growth mechanism is never desired during organic molecule crystallisation and is postulated to be directly proportional to the supersaturation [133]. The growth rate in this regime can be defined using the following equation with A being a system dependent constant:

$$R_{hkl} = A\sigma \tag{2.23}$$

Surface integration limited growth

If surface integration (SI) is the rate limiting step, growth normal to the surface occurs as layers of solute molecules build on top of one another either via 2-D nucleation and growth or via spiral growth (BCF model) (Figure 2.9(b)). This growth type does not require an abundance of kink sites and can progress at low to moderate supersaturation, therefore predominantly occurs on F faces.

- 2D Nucleation and Growth: This mechanism resonates with homogeneous nucleation where the formation of a critical nucleus on the crystal face is essential for growth to begin. Once the nucleus exceeds the critical size, solute molecules can attach onto it such that the nucleus grows laterally leading to the formation of a layer, and such a build of layers from nuclei on the facet leads to crystal growth normal to the facet. This growth is defined via two characteristic times; τ_{birth}, and τ_{spread}, which are the time for the appearance of a single 2D nuclei and the time taken for the nucleus to spread over the entire facet area, respectively [12]. If, $\tau_{birth} >> \tau_{spread}$, growth is 'mononuclear' because formation of multiple nuclei is time consuming. If $\tau_{birth} << \tau_{spread}$ growth is 'polynuclear', when multiple nuclei form on the edges and corners of the facet and the layers resulting from them merge together to form one single layer covering the surface. But if $\tau_{birth} \approx \tau_{spread}$,

then nuclei form and spread simultaneously, known as the 'Birth and Spread'(B&S) regime. Under 2D nucleation, the facet specific growth rate, R_{hkl} has an exponential dependence on the supersaturation [133]:

$$R_{hkl} = A_1 \sigma^{5/6} \exp\left(\frac{A_2}{\sigma}\right) \tag{2.24}$$

Where A_1 and A_2 are system-specific constants.

- Spiral Growth: This theory developed by Burton, Cabrera, and Frank (BCF) [134, 132], is based on the formation of kink sites from screw dislocations (Section 2.4.1). The dislocation exposes an edge on which, after it exceeds critical length, solute molecules adsorb onto the kink sites resulting in the step to grow laterally in a perpendicular direction to the facet. As the step is growing, an edge always remains exposed, forming a continuous spiral. The BCF growth rate of a facet can be expressed as [133]:

$$R_{hkl} = A\sigma^2 \tanh\left(\frac{B}{\sigma}\right) \tag{2.25}$$

Where A and B are temperature dependent constants. When $\tau_{birth} >> \tau_{spread}$, it is energetically more favourable for growth to occur via the already present surface dislocations rather than a 2D nucleation regime [12].

The direction of PBCs in a facet governs the direction of facet growth. Therefore the PBC direction can be approximated by examining the edges of the 2D nucleus and the spiral where each new edge corresponds to the adjacent PBC [49, 132, 135]. The growth mechanisms as a function of supersaturation are depicted in Figure 2.9(c) [49, 13]. At low supersaturations, BCF dominates over B&S due to a high energy barrier for 2D nuclei formation. As supersaturation increases, B&S model dominates followed by rough growth at extremely high supersaturations. It is important to note that this dependence on supersaturation only holds true, if either of the mechanisms: diffusion or SI, largely dominate over the other. At low supersaturation, surface integration will only be limiting if mass transfer limitations are negligible (no stirring at very small volumes) or if mass

transfer is extremely fast (adequate mixing in a large volume). If SI and diffusion are both competing, then the mechanism cannot be deduced based solely on the supersaturation, and further investigations need to be carried out.

2.3.6 Measuring growth rates

Various analytical techniques like microscopy [136], Focused Beam Reflectance Measurement (FBRM), and Fourier transform infrared/attenuated total reflectance spectroscopy (FTIR/ATR) [137, 138, 24], are implemented to measure average crystal growth rates (m/s) in a batch crystalliser using the desupersaturation curves. However, when understanding the fundamentals of crystal growth, single crystals are normally used and two methods are generally used to measure their growth rates:

- Facet specific growth rate (m s^{-1}): Where the forward movement of facet (hkl) is measured over time [133, 20, 139, 140]

- Overall Linear Growth Rate (m s^{-1}): Which is the rate of change of the crystal's characteristic dimension, such as length and width, over time. This is particularly useful when crystal habit is such that capturing facet growth rate is difficult and hence an arbitrary crystal dimension can be defined to analyse a group of similar single crystals [141, 142, 143, 144].

Using these measurements, the growth rate, G, is calculated using the following equation:

$$G = \frac{dL}{dt} \tag{2.26}$$

Where L is the length of the characteristic dimension or the distance between the crystal centre and the facet (hkl), and t is the time. Crystal growth experiments are carried out in various crystallisation conditions and in most studies the crystal growth rates are

expressed as a function of supersaturation using an empirical power law equation [145]:

$$G = k_g(S-1)^g \tag{2.27}$$

Where g is the growth rate order, $S-1$ is the relative supersaturation (sometimes also replaced with Δc) and k_g is the rate constant, expressed as a temperature dependent, Arrhenius-type equation:

$$k_g = k_{g,0} \exp \frac{-E_a}{RT} \tag{2.28}$$

where $k_{g,0}$ is the rate constant pre-exponential factor, E_a is the activation energy, R is the universal gas constant, and T is the temperature in Kelvin. When it is certain that growth is SI limited, the growth rates are also fitted using either of the 2D nucleation (Equation 2.3.5) or BCF (Equation 2.3.5) models mentioned above, instead of the generic power law.

2.3.7 Effect of external factors on crystal growth

As understood from the above sections, the interplay of facet specific growth rates results in variation of end crystal habits. Crystals exist in various shapes including needle, cubic, plate, prisms etc., and some are preferred over the other depending on the application [89]. High-aspect ratio (needle) crystals are generally disliked in the pharmaceutical industry as they are more fragile and difficult to process compared to cubic or prismatic crystals. Crystal shapes are drastically influenced by external factors such as variation in the solvent used, supersaturation, temperature, and impurities [107], as will be seen below.

Variations in supersaturation were demonstrated to switch-on and switch-off specific facets in urea [146] and paracetamol crystals [20], leading to different morphologies. Whilst low supersaturation resulted in columnar habits in paracetamol, and needle-like habits in urea, high supersaturation led to more prismatic habits in both. Moreover, at lower temperatures it was shown that the area of (001) facet of 1,1-diamino-2,2-

dinitroethylene reduced considerably, resulting in low aspect-ratio diamond-like crystals, suitable for intended use [147].

Crystal anisotropy results in varied solute-solvent interactions on the different crystal facets and has hence been shown to affect the final crystal shape [148, 149]. MAE calculations and molecular modelling are extensively used to study these differences in habits [126, 150, 151, 152, 125, 153, 154]. For example the (110) facet on salicylamide crystals was shown to have reduced growth in ethyl acetate, resulting in a more plate like habit as opposed to a block-like habit [155]. Moreover, using a modelling approach, an ideal solvent was selected to reduce the aspect ratio of needle-like 2,6-dihydroxybenzoic acid form 2 crystals [156]. Experimental studies with paracetamol have demonstrated a columnar habit when using polar protic water, and a prismatic habit in other selected polar protic, aprotic, and non-polar solvents [157].

The presence of impurities and additives in the crystallisation cocktail has also proven to have extensive effects on the crystal growth process, as detailed in these reviews [158, 159, 160]. The step-blocking mechanism developed by Cabrera and Vermilyea, propose the cessation of layer propagation on a facet due to the adsorption of impurity molecules on the surface, and is utilised by multiple studies [161, 162, 163]. For example, amino acid impurities during L-alanine crystallisation [164], and p-acetoxyacetanilide impurity during paracetamol crystallisation [165], have shown to inhibit the growth of certain facets resulting in elongated structures.

2.4 Mechanical properties of crystals

2.4.1 Lattice defects

Imperfections in the crystal lattice are crucial when it comes to determining not only the chemical and mechanical properties of the crystalline solid but also the growth process. These defects are broadly categorised into four main types:

- Point Defects (0D): 'Vacancies' are a common point defect where 'holes' develop in the lattice due to missing molecular units [48].

- Line Defects (1D): In this case dislocations are characterised by line vectors and Burgers vectors, **b**. When the dislocation line vector is parallel to **b**, a partial step is produced on the crystal surface, and is called a screw dislocation [166, 101], useful for spiral growth.

  In edge dislocation, the line vector is perpendicular to **b** and occurs due to the insertion of an extra half plane within the lattice [101]. Dislocation occurs at the weakest point in the lattice, the 'slip plane' of the crystal [1, 48]. When force is applied, the crystal will shear at this plane as here it has the weakest interactions with its neighbouring planes [167]. Slip planes are important in a pharmaceutical context as their presence has been shown to increase the compressibility of crystals and therefore their tabletability [168]. Recent work has also shown their incorporation in computational models simulating compression of single crystals [169].

- Surface/Planar Defects (2D): Stacking faults or mismatch in boundaries such as 'twist' and 'tilt' boundaries lead to defects that can be seen on the face of the crystal [48, 166]. For example, twinning is a common stacking error where a mirror image of the face is created due to a change in the attachment order of molecular units [62].

- Volume Defects (3D): Is the incorporation of undissolved solids such as precipitates and dispersed particles, or gaseous species such as voids and bubbles into the crystal lattice [170].

2.4.2 Slip planes vs. cleavage planes

There are discrepancies in the literature about what slip planes and cleavage planes are, and in certain occasions they are used interchangeably. Cleavage is a form of crystal fragmentation that occurs in the direction perpendicular to the plane of least resistance

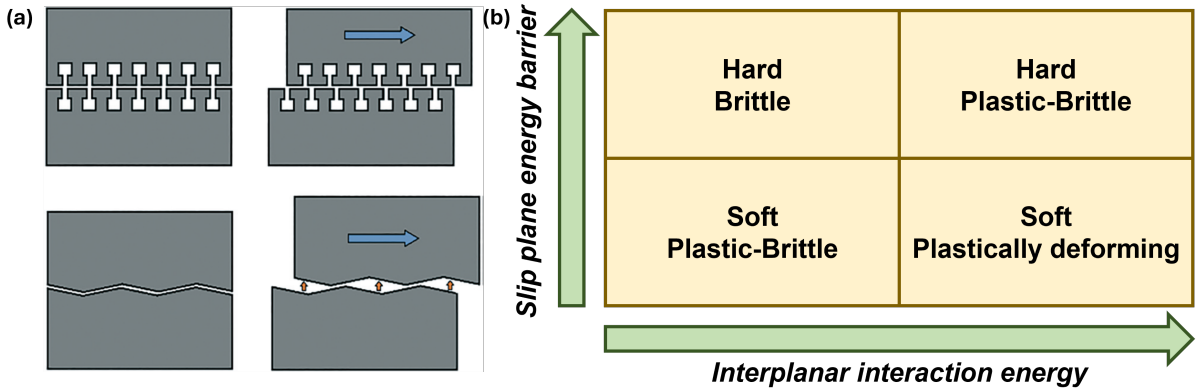


Figure 2.10: (a) Effect of surface corrugation on slip propensity. Top: High corrugation but no interpenetration between 2 layers, hence highly likely to slip. Bottom: Less corrugation but high interpenetration between the 2 layers, thus more likely to cleave. Image obtained with permission from [14] (b) Matrix depicting the possible outcomes of the interplay between slip plane energy and the detachment energy, adapted from [15]

whilst slip is a form of plastic deformation occurring parallel (lateral displacement) to the plane of least resistance. While slip is the measure of crystal ductility, cleavage is the measure of crystal brittleness [15].

Traditionally, the d-spacing and the attachment energy of a facet are used to identify the slip and cleavage planes. Planes with higher d-spacing and/or low attachment energies are considered to be weakly interacting and hence more prone to slippage and cleavage. However, they are both deemed as inadequate at accurately predicting mechanical properties of a crystal [15, 171]. d-spacing does not take into account crystal anisotropy and fails for systems with 1D and 2D hydrogen bonding dimensionality. Although attachment energies consider intermolecular interactions of a facet, they are predicted in vacuum and are not an extensive quantity. The AE theory only considers the energy required to attach a single molecule to the facet rather than the entire area of the facet.

Hence, although the d-spacing and attachment energy method can be used for an initial approximation, two other parameters need to be considered when identifying slip and cleavage planes.

1. Specific interaction energy [15]: the attachment energy normalised with respect to

the facet surface area, also known as the detachment energy:

$$\gamma_{hkl} = Z \times d_{hkl} \times |E_{hkl}|/2V \tag{2.29}$$

Where Z is the number of molecules in the unit cell and V is the volume of the cell. This quantity is essentially the work required to detach a layer of molecules in a direction perpendicular to the plane i.e. barrier to cleavage. Simplistically, a low interaction/detachment energy will mean a more brittle surface, which is likely to favour cleavage.

2. Surface corrugation [14]: The extent to which planes are physically intertwined (Figure 2.10(a)). This qualitative parameter indicates the energy barrier for the lateral displacement of the plane, i.e. for slippage. So, a smoother, less corrugated surface will result in higher chances of slip.

When a material experiences impact stress, it has two primary responses: it can either accommodate the stress by slipping along planes with the lowest energy barrier, or it can fragment at an interface with the lowest detachment energy. Based on the interplay of these two conditions, the mechanical behaviour of planes can be summarised into a matrix as seen in Figure 2.10(b) [15]. At the extremes, if the minimum detachment energy of a plane is lower than the slip energy barrier, it is more prone to fracture. Conversely, if the slip energy barrier is lower than the minimum detachment energy, the plane is more likely to exhibit plastic behaviour. However, due to crystal anisotropy, planes can lie anywhere in between the spectrum of plastic to brittle. Thus, mechanical responses are not straightforward where the slip barrier and the inter planar interaction energy are both similar to each other. In that case, the orientation of the crystal to the applied stress and its magnitude will impact the mechanical behaviour. As paracetamol is the system of interest for regeneration studies, a detailed analysis of its mechanical properties and cleavage plane identification can be found in Section 4.3.1 of the first results chapter.

2.5 Current understanding of crystal breakage and growth

The crystalline structure of organic molecules has long puzzled scientists. As attractive is the highly ordered nature and purity of the crystal products, it is equally difficult to decipher the crystalline lattice, and its critical quality attributes. Approaches to determine crystal morphology have evolved over the years, as detailed in Section 2.3, but it is surprising to see that very little is known and studied about the effect of mechanical breakage on the final crystal structure, shape and size. Population Balance Models (PBMs), are mathematical models used to determine the number density of particles in the crystalliser i.e the Particle Size Distribution (PSD), using kinetic data of various crystallisation mechanisms such as nucleation and growth [172, 173]. A reliable model for simulating the crystallisation process is highly desirable, as it allows thermodynamic and kinetic parameters to be optimised for the final product before implementation, saving time and cost compared to trial-and-error methods. However, comprehensive models that account for all process mechanisms, including crystal breakage and post-breakage behaviour, are rare. This is due to the complexity of PBMs, which become less feasible to solve as more dimensions and parameters are added, and the limited understanding and experimental data on crystal behavior after breakage itself, which makes modelling them even more difficult [174, 175].

Firstly, crystal breakage is generally deemed insignificant and ignored for crystals below the 10 μm size range [7]. However, crystals used for oral dosage, are around 200 μm [176] and thus understanding their breakage, and growth and shape evolution post breakage is crucial. Crystal-Impeller (CI), Crystal-Crystal (CC), and Crystal-Wall (CW) interactions are very prevalent in industrial crystallisers, making attrition a highly studied phenomena. Gahn and Mersmann in 1999 developed a mathematical model predicting the fracture behaviour of the crystals depending on the impact forces applied [177] and consequently a growth model for the resulting fragments [178]. Bosetti and Mazzotti in 2019 used these

findings to develop a population balance model that took into account this attrition and size dependent growth [179]. Along similar lines, Tyrrell et. al., developed a model to specifically account for different types of crystal fragmentation, however they still utilised size dependent growth for particle size determination [180]. Moreover, the simultaneous prediction of PSD and crystal shape is an emerging field of 'Crystal Shape Evolution' [174, 181, 49], which takes a step closer to accurately determining the final crystal properties. Recent work by Doherty, uses facet specific growth rates and shape factors to derive a 1-D PBM that determines the shape and size evolution in a Mixed Suspension Mixed Product Removal (MSMPR) crystalliser [174, 181]. However, none of these models take into consideration specific post breakage growth kinetics, and assume that growth of fragments will follow the same trajectory as unbroken crystals. Very recently, steps have been taken in understanding the facet development of fractured crystals through 4D tracking in studies observing the growth of fractured aluminium potassium sulfate crystals [182]. Additionally, simulations have been employed to predict the growth rates of the facets of para-aminobenzoic acid crystals exposed by breakage [183]. On the process modelling side, an MSMPR model has been developed, designed to utilize broken crystals as seeds as a means of enhancing product yield due to their faster growth rates than unbroken crystals [184]. However, still, large knowledge gaps exist in the understanding of the specifics of the post-breakage crystal growth behaviour due to a lack of experimental evidence.

Recent work has also shown many peculiarities in the behaviour of organic crystals in response to external mechanical forces, regarding them as dynamic crystals [185, 186, 187]. Some molecular crystals have been shown to 'self-heal' into a single entity after its two broken pieces were pushed together [188, 17, 189] (Figure 2.11(b)), whilst some have shown to self-heal the surface cracks by bridging their inter-molecular network [37]. Another example is of ferrooelectric crystals that show elasticity and thus return to their original shape after lateral compression [18] (Figure 2.11(c)). Moreover, Malla Reddy's work on 'bending crystals' (Figure 2.11(a)) show that the activation of slip-planes in a certain direction play a huge role on the elasticity and plasticity of crystals [16, 190, 39].

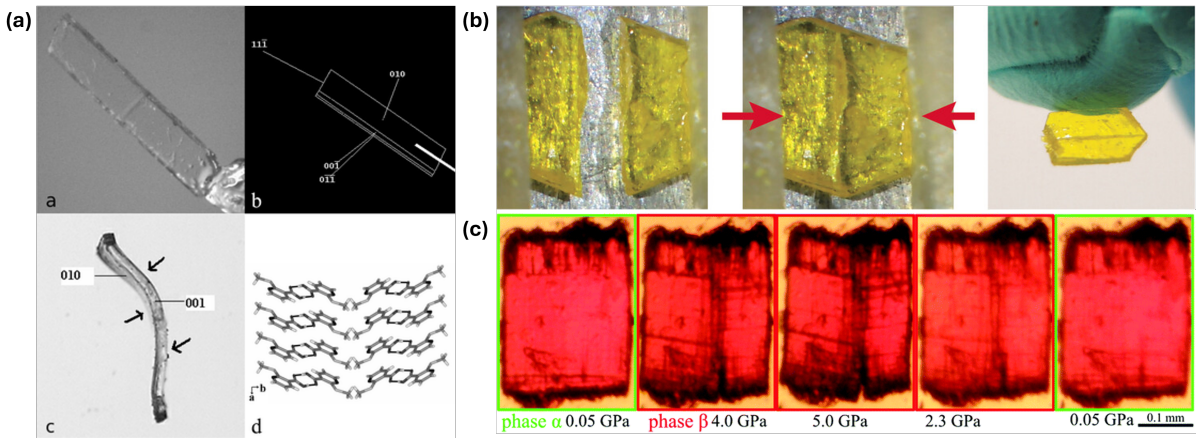


Figure 2.11: (a) 2-(Methylthio)nicotinic acid crystal bent on the (010) face (b) self-healing dipyrazolethiuram disulfide crystal after application of moderate mechanical compression (c) Self-healing of the cracks in a ferroelastic crystal AMU3. Images have been obtained with permission from [16] [17], and [18] respectively

This emphasises that there are eccentricities in the way organic molecular crystals behave in the presence of mechanical pressure and thus their behaviour cannot be ignored.

2.6 Crystalline state of paracetamol

Paracetamol, also known as Acetaminophen, is a very common analgesic and antipyretic drug used in modern medicine. It is an aromatic compound with a carbonyl, amide and hydroxyl group attached on *para* position (Figure 2.12) which leads to hydrogen bonding within the crystal lattice. So far nine anhydrous polymorphs of paracetamol have been discovered, with forms I, II, and III being the only ones produced by solution crystallisation [191]. The stability of the three polymorphs varies in the order I > II > II, such that monoclinic form I is the most stable [192], followed by the metastable form II (orthorhombic) [193] and the least stable form III [194]. Due to the high instability of form II and form III, they convert instantly after generation into the stable form I, thus making their isolation tricky. However, efforts have been made in recent years to produce and isolate the two polymorphs as they provide improved solubility and compressibility compared to the form I paracetamol. Despite recent successes in crystallising the elusive Form III in confined conditions, such as vacuum-sealed glass capillaries and observing it in situ

using Differential Scanning Calorimetry (DSC) [106, 195], large-scale production remains a challenge. Form II has been successfully isolated using batch and continuous processes with the aid of additives such as metacetamol [19, 196, 197], and other carboxylic acids [191]. The flat arrangement of hydrogen-bonded planes in form II offers enhanced compressibility, making form II the preferred polymorph for tableting purposes [198]. The herringbone lattice of Form I paracetamol makes it inherently brittle [199], causing it to preferentially fracture along the (010) plane during milling [200]. The difference in their internal structure also leads to different habits where form I is prismatic while II is more elongated, Figure 2.13(a) [19].

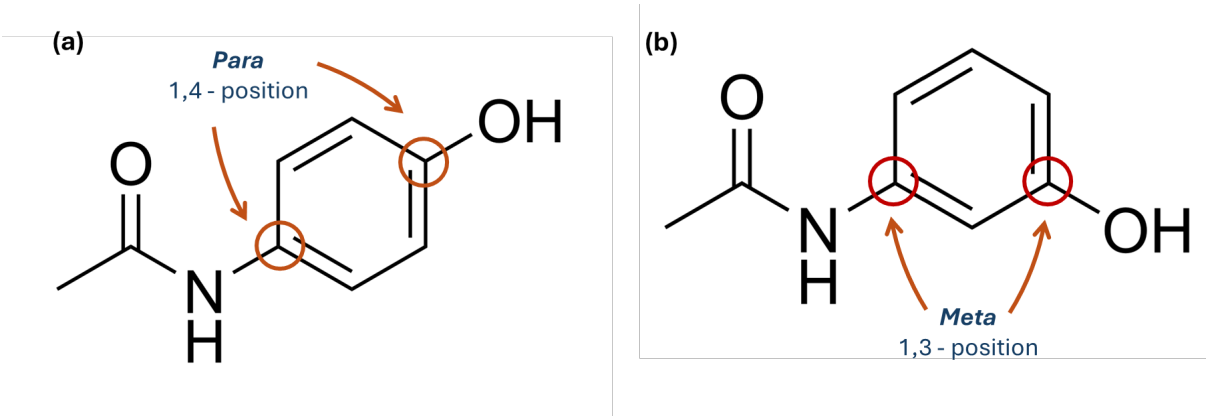


Figure 2.12: Comparison between the chemical structure of (a) paracetamol and (b) metacetamol, highlighting the difference in the *para* and *meta* positions of the amide and hydroxyl functional groups

Throughout the years extensive amount of research has been done on the crystallisation of paracetamol by evaporation [40, 142], cooling [201, 202, 203], melts and antisolvent. Multiple papers can be found in the literature that have studied the growth of paracetamol crystals in batch crystallisation environment, as well as in single crystal environment. The nucleation and growth of form I paracetamol has shown strong dependence on supersaturation [20] (Figure 2.13(c)), temperature [204, 24], solvent [157, 205] (Figure 2.13(b)), and flow conditions [145], as detailed in above Sections 2.2.2 and 2.3.7. Paracetamol crystals are largely anisotropic and their facet specific properties have been studied using various characterisation techniques such as X-ray Photoelectron Spectroscopy (XPS) [40] for surface chemical composition, Atomic Force Microscopy (AFM) to study surface roughness and growth mechanism [206], Time of flight secondary ion mass spectrometry (TOF-

SIMS) to study impurity distribution mapping [207], as well as optical interferometry to study surface defects [208].

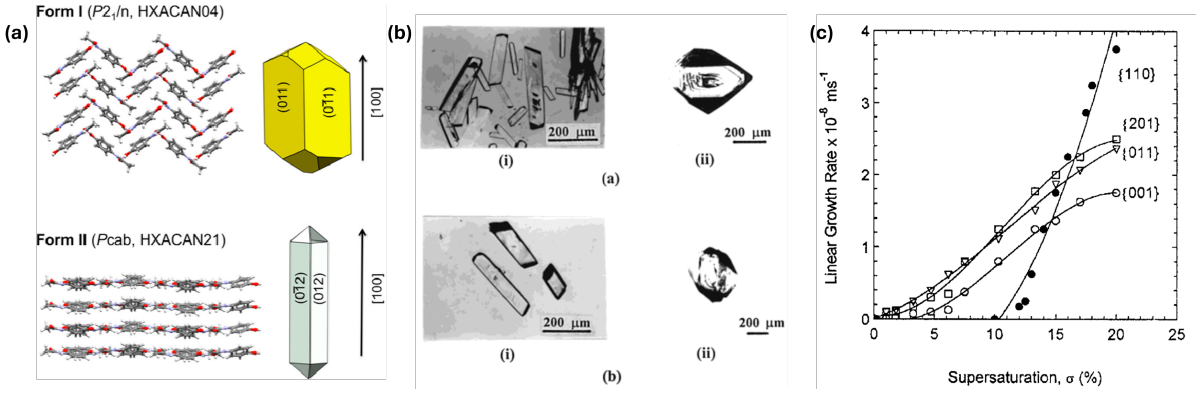


Figure 2.13: (a) The packing and morphology of form I and form II paracetamol, used with permission from [19], (b) form I paracetamol grown in top: ethanol, bottom: water vapour at (i) low and (ii) high supersaturation, (c) facet specific growth rates of form I paracetamol as a function of supersaturation. (b) and (c) used with permission from [20]

Although numerous studies exist on the growth of paracetamol single crystals, the understanding of their growth behaviour after breakage remains limited. This thesis aims to systematically study the growth of paracetamol crystals after breakage and draw conclusions that could be translated across organic crystals for improved prediction capabilities of their end size and shape.

Chapter 3

Materials and Methods

3.1 Materials

Investigations on regeneration were predominantly carried out on form I paracetamol crystals. Paracetamol, meeting USP testing specifications (CAS: 103-90-2), was acquired from Sigma Aldrich with a purity of >98.0%. Additionally, other organic pharmaceutical compounds were tested for regeneration, as will be seen in the future works section (chapter 7), such as Carbamazepine (CBZ), and Aspirin. Carbamazepine (CAS: 298-46-4) and aspirin (CAS: 50-78-2) of purity >98.0% and both meeting USP testing specification, were purchased from Sigma Aldrich. Three solvents were used to study crystal growth and regeneration; ethanol, acetone, and tetrahydrofuran (THF). Ethanol (CAS: 64-17-5) with 100.0% purity and acetone (CAS: 67-64-1) with 100.0% purity were purchased from VWR Chemicals. THF (CAS: 109-99-9) with 99.8% purity was purchased from Thermo Scientific. All chemicals were used as received without any further purification.

3.2 Solubility determination

The most common procedure of measuring the solubility involves stirring an excess amount of solute in the desired solvent for a prolonged period of time, until a thermal equilibrium is reached. Following this, the concentration of the clear solution is determined [22]. A similar approach was undertaken for determining the solubility of paracetamol. An excess of as received paracetamol was mixed with 100 ml of solvent and stirred using a magnetic stirrer at 200 rpm for 24 hours at the desired temperature. The temperature was controlled using a circulating water bath, Grant GR150, which has a temperature range from -5 to 150 °C and a sensitivity of +/- 0.005 °C. A jacketed vessel was connected to the waterbath and filled with enough water to immerse the jar such that effective heat transfer between the jacket and the jar took place. Following a mixing period of 24 hours, the solution was allowed to settle for 2 hours and subsequently two 5 ml samples of the supernatant were taken. The concentration of the supernatant can be measured using various techniques such as UV-Vis [209], FTIR [96], HPLC [210] or gravimetric analysis [22, 19]. In this case gravimetric analysis was used. The 5 ml samples were filtered through a 0.2 µm cellulose acetate membrane into eppendorf vials and allowed to evaporate until no traces of liquid were left. The mass of the solution before and after evaporation was measured and the concentration of the solution was calculated using equation 3.1 [22]. This was repeated thrice for each temperature and hence an average concentration over six samples was calculated to determine the solubility curve.

$$c = \frac{(m_{vdr} - m_v)}{(m_{vs} - m_{vdr})} \tag{3.1}$$

Where m_{vdr} is the combined mass of the dried solute and the vial, m_vs is the combined mass of the solution and the vial, and m_v is the mass of the empty vial.

3.2.1 Metastable zone width determination

For the purpose of this work, cloud point temperatures were measured to determine the MSZW. Following up from the above Section 3.2, at each temperature being investigated, after taking samples for gravimetric analysis, the rest of the supernatant was filtered into three 30 ml vials. A small PTFE stirrer bar was placed in the vials and they were put back into the jacketed vessel. At a cooling rate of 0.1 °C/min and agitation of 200 rpm, the solution was cooled until spontaneous nucleation occurred, monitored using a Nikon D90 DSLR camera with a Nikon AF-S 18-105 mm lens, which took images every 1 min using an external timer. The images were analysed manually to note the time taken for the solution to turn cloudy and consequently calculate the corresponding temperature using the cooling rate. As 3 vials were studied at the same time, an average cloud point temperature was obtained and eventually a supersolubity curve was determined.

3.3 Macroscopic single crystals

Macroscopic single crystals were used across all the experimental work detailed in this thesis. Since this work investigates a unique phenomenon that has not been reported before, it is crucial to be able to visualise the process as clearly as possible. With microscopic crystals any growth process occurs relatively quickly compared to macroscopic crystals making it difficult to capture. As the regeneration process would take place over a prolonged period of time in macroscopic crystals, this increases the feasibility of capturing the process via imaging techniques, thus enabling superior elucidation of the phenomenon which could further be translated onto microscopic crystals.

3.3.1 Seed preparation

Single crystals for the regeneration experiments were obtained via slow solvent evaporation at room temperature, irrespective of the solvent. Firstly, a saturated solution of

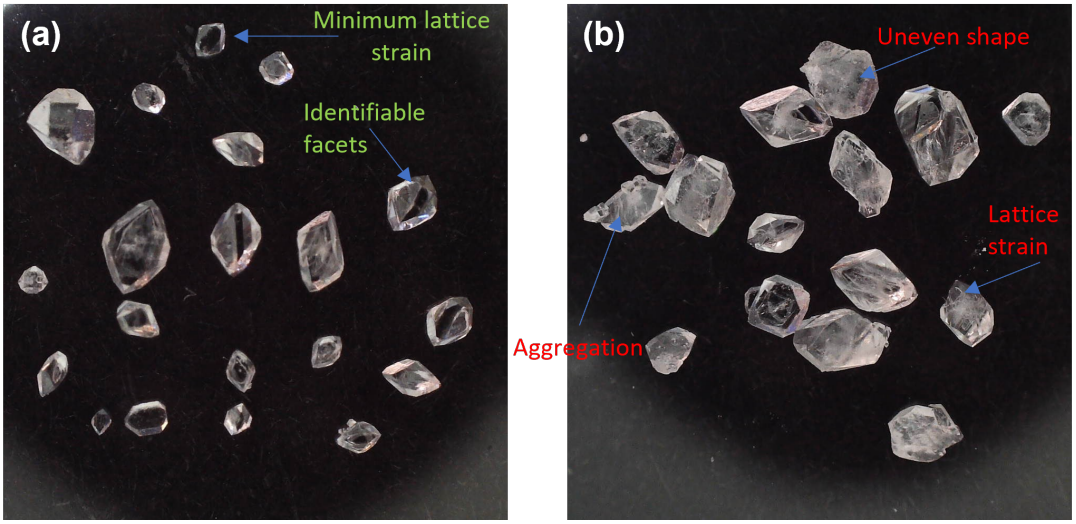


Figure 3.1: Representative image showing a broad classification of (a) High quality seeds and (b) Poor quality seeds

Paracetamol and the desired solvent at room temperature was prepared by mixing an excess of solute in a 500 ml glass bottle with the solvent. The contents were then stirred for 24 hours using a magnetic stirrer. Consequently, the solution was allowed to rest until the excess solids settled to the base of the bottle and the saturated solution above could be extracted.

The supernatant was extracted using a plastic syringe and filtered through a 0.45 µm PTFE filter into a 50 ml borosilicate glass crystallisation dish. Once the dish was three quarters of the way full, it was covered using parafilm which was pierced using tweezers to make approximately 1 mm diameter perforations. It was then placed in the fumehood to allow for slow evaporation of the solvent. After having left the crystallisation dish in the fumehood for a few days, depending on the rate of evaporation of the solvent, approximately 1-2 mm diameter seeds of paracetamol could be seen at the base of the dish. These seeds were carefully extracted using blunt tweezers, immediately placed on a soft tissue and pat dried to avoid encrustation on the crystal surface. These seeds were stored away in an air tight glass vial until further use.

It was ensured that only high-quality seeds were selected and used in subsequent steps. To broadly define 'high quality', seeds obtained from the same dish under identical crystallisation conditions were categorised into two groups: "good" and "bad," as shown in

Figure 3.1. 'Good' or 'high-quality' crystals met two key criteria. First, they needed to be relatively pristine, with minimal to no stress accumulated in the crystal lattice and minimal to no surface defects. Second, the four major facets—(001), (011), (201), and (110)—had to be clearly identifiable.

3.3.2 Growing large single crystals

Different techniques were used in order to grow the seeds further into the desired size. In order to grow the seeds into 4-5 mm (small) sized crystals they were individually placed in 10 ml vials containing the supersaturated solution. The vials were covered with parafilm, perforated as mentioned above and placed in the fumehood for 1 week to enable evaporative crystallisation. The solution was continually refilled so that the vials do not dry out during the experiment. Once the crystals reached an approximate size of 4-5 mm they were extracted and stored using the same procedure as mentioned above.

In order to grow 7-8 mm (large) sized crystals, the aforementioned small crystals were looped on a string made of a few strands of Kevlar fibres. The crystal was carefully looped around its centre with the knot resting on the top of the crystal such that growth occurred around it, eventually engulfing the knot. The looped crystal was consequently immersed into in a 30 ml glass vial filled with the saturated solution, using a stainless steel rod (Figure 3.2(c)). Kevlar fibres were utilised for their high tensile strength despite the strands being thin. This enabled the crystal to grow large without snapping the string as well as aided good quality imaging. The vial was covered with parafilm which was perforated in a similar manner as detailed previously and the crystal was let to grow for a period of 1 week via slow evaporation. Crystals were hung in solution in order to minimise contact with the walls and base of the vial to prevent growth inhibition of facets. This was particularly important when growing large crystal as they are in solution for a long period of time. A few important points to note:

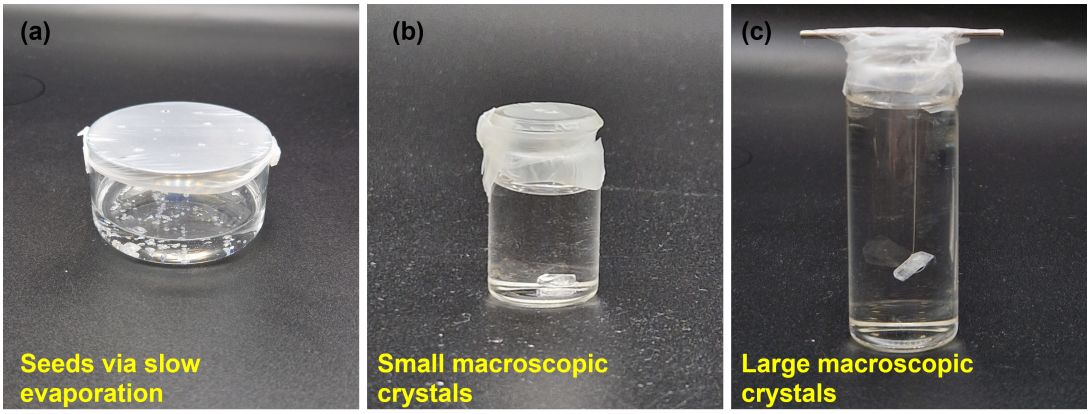


Figure 3.2: Slow solvent evaporation procedures for (a) obtaining paracetamol seeds, (b) isolating the seeds to grow small macroscopic crystals, and (c) dangling the small crystals in solution using kevlar fibres to obtain large crystals

1. Room temperature in this context is approximately 25 °C ± 2 °C.

2. The 'size' of the crystal refers to an approximation of the longest edge to edge distance of a crystal.

3. Prior to using any stored seed or crystal, they were washed with ice cold (4 °C) de-ionised water and pat dried using white tissue in order to wash away any macroscopic impurities on the crystal surface. As solubility of paracetamol in water is low especially at lower temperatures (8.2 g/kg_{water} at 5 °C [22]), this enables cleaning the crystal without dissolving the facet surfaces.

3.4 Crystal cleaving

Cleaving a crystal involves cutting the crystal along its most brittle plane such that its internal counterpart is exposed. In the context of this thesis, all crystal cutting was done by applying mechanical force on the crystal to mimic the mechanical breakage undergone by crystals in an industrial crystalliser. A Swann Morton No 26 scalpel blade was used to break the crystals which had a tip size of approximately 1 × 0.5 mm. Point pressure was applied on the (001) facet of the macroscopic paracetamol crystal led to a self-propagating crack along the (001) facet in the a direction. This resulted in the crystal snapping into

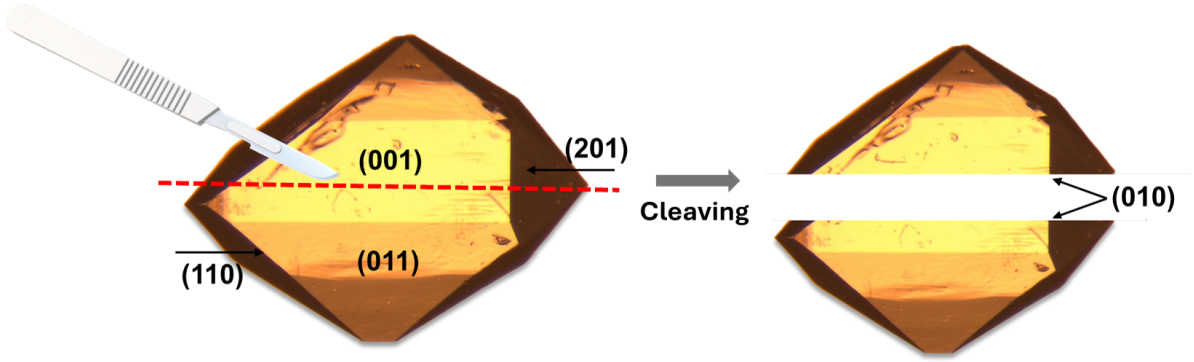


Figure 3.3: left: Macroscopic paracetamol crystal grown in ethanol being cut using a scalpel by applying point pressure on the (001) facet, Right: Paracetamol crystal after cleavage, with (010) plane exposed

two clean halves exposing the cleavage plane, (010). For all regeneration experiments, freshly cut crystals were used. Once the crystals were cut, they were quickly rinsed with ice cold water to wash away any crystalline debris generated as a result of mechanically breaking the crystal. Following this, the crystals were pat dried with white tissue to dry out any excess water prior to starting the regeneration experiment.

3.5 Crystallisation techniques for crystal regeneration

Crystal regeneration was investigated via two major techniques: evaporative crystallisation and isothermal crystallisation:

1. Evaporative crystallisation: Crystal growth via solvent evaporation although is not an industrially relevant technique, is commonly used for lab scale experiments for slow and controlled crystal growth. All evaporative crystallisation experiments in accordance with this thesis, have been carried out at room temperature and pressure with no active temperature control and was limited to the paracetamol-ethanol system. As most laboratory apparatus is resistant to ethanol, it was possible to allow the solution to evaporate slowly over a prolonged period of time, avoiding drastic changes to the concentration of the mother liquor. This was due to a continuous

creation and depletion of the supersaturation during the growth of crystals, resulting in a self-regulating steady state. The maintenance of a low supersaturation over a long period of time enabled capturing the phenomenon clearly via imaging.

2. Isothermal crystallisation: To quantify the rate of crystal regeneration and crystal growth more accurately, an isothermal crystallisation set-up was designed and utilised. This will be discussed in detail in 5. The working principle of this method involves making a saturated solution of the system of interest at a desired temperature followed by cooling it down to a temperature corresponding to the needed supersaturation. Once the solution has equilibrated at the lower temperature, the crystal is inserted and growth is monitored (Figure 5.1). The temperature for the required supersaturation is calculated using the solubility data of the solute in the respective solvent. It is also crucial to ensure that the chosen range of temperature is within the metastable zone of the system to prevent any primary nucleation.

3.6 Imaging techniques

To capture the regeneration phenomenon, distinct imaging set-ups were designed to work in conjunction with the desired crystallisation approach. Two major types of imaging techniques were implemented; optical microscopy using a streo microscope, and macrophotography using Digital Single-Lens Reflex (DSLR) cameras, as elaborated below.

3.6.1 Optical microscopy

Stereo microscopy is a type of optical microscopy commonly used in biological and biomedical applications for 3D imaging and analysis of biological objects such as cells, tissues, and embryos [211, 212]. For imaging single crystals in the context of this work, Leica M60 stereo microscope was jointly used with the Leica MC120 HD camera. Leica

Application Suites (LAS Core V4.13) software was then utilised to analyse the images and obtain crystal dimensions. Since macroscopic crystals, of 4 mm size range, were used for the experiments, a stereo microscope was used rather than a compound microscope. Although both are types of optical microscopes, stereo microscopes are more adequate for larger objects as they have a lower optical range: 6x to 50x magnification. Even with a low optical range, the images produced are more three dimensional than those from a compound microscope as the stereo microscope has separate optical pathways for the two eyepieces and objective lens [213]. This, in combination with a longer working distance which allows for manipulation of crystals when on the stage plate, enabling high quality crystal visualisation and facet identification.

3.6.2 Macrophotography

For real time imaging of crystals under certain crystallisation conditions (for example, in the presence of agitation, or observing crystals larger than 4 mm), microscopic imaging can be challenging. Hence macrophotography with the help of DSLR cameras was implemented. In simple terms, this involves taking extreme close-up photographs of small objects such that the object in the photograph is not only larger than in real life, but also the fine details of the subject are captured [214, 215]. This type of photography is commonly used for capturing details in nature eg., dewdrops on leaves, flower buds and filaments, as well as features of an insect. This is only possible if the camera lens being used allows for 1:1 magnification, meaning, the size of the object as appears on the camera sensor is equal to the objects size in the real world. Hence the object of interest should be smaller than or equal to the size of the camera sensor. Such lenses also mean a long focal length wherein the field of view is narrow but the depth of field is longer. As such it is possible to bring the camera close to the object, without losing focus, allowing the object to occupy most of the sensor area and therefore capturing more details of the object. For the purpose of the experiments explained further in the thesis, Nikon D90 DSLR cameras [216] were used, with a sensor size of 23.6 $\times$ 15.7 mm, for crystals of a

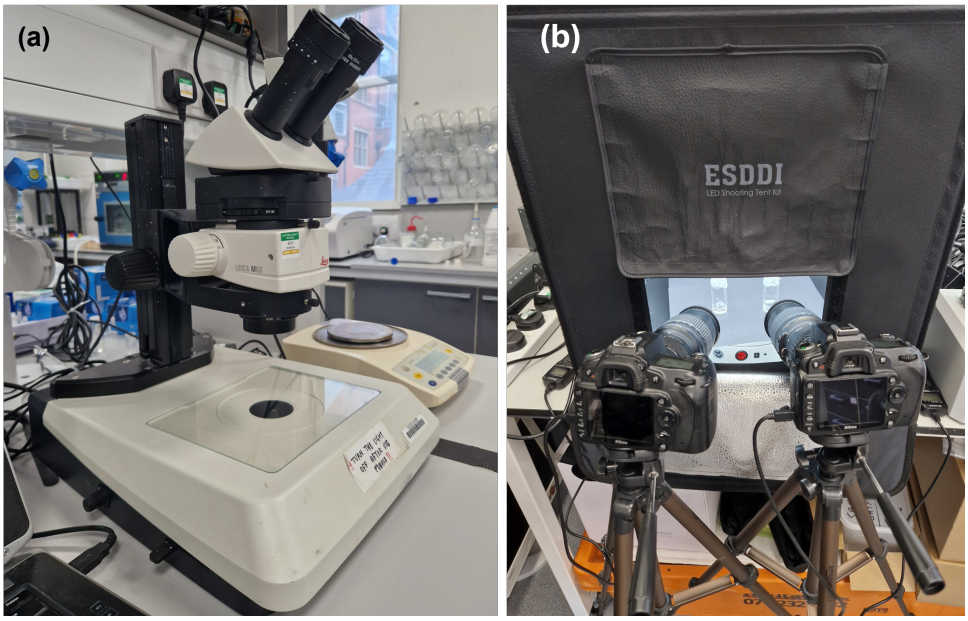


Figure 3.4: (a) Leica M60 stereo microscope used for optical microscopy of single crystals (b) Macrophotography set-up designed for single crystal imaging

size range 4-8 mm. The camera was attached with a Nikon AF-S 18-105mm lens and 68 mm Newer extension tubes, to take high resolution macro photographs.

3.7 Measuring crystal growth rate

Crystal growth rates in the context of this thesis were measured in one of the two following ways:

- Change in characteristic dimensions: Two characteristic dimensions of the crystal were measured over time; length a, normal to the cleavage plane, and length b, parallel to the cleavage plane (figure 3.5(a)).

- Facet propagation: To get a more accurate representation of the rate of regeneration, facet specific growth rates of two facets, (010), and (110) were measured. This was done by measuring the growth normal to the facets such that facet advancement over time could be recorded (Figure 3.5 (b)). As imaging was only done from one direction, only the aforementioned facets could precisely be identified and tracked. The dihedral angle between (010) and (110) was found to be 37.4°from

the predicted vacuum morphology in Materials Studio. This was further consolidated by manually measuring the angle using Image J for images at time = 0 for 5 randomly selected experiments and obtaining angles between 35-37 °. Using this angle, the length of (110) at a given time was calculated by the following Equation 3.7:

$$L_{(110)} = x \times \cos(90 - \theta) \text{ where } \theta = 37.4^{\circ} \tag{3.2}$$

Where $L_{(110)}$ is the length of facet (110), and θ is the dihedral angle between (110) and (010), and x is the perpendicular distance between (010) and the topmost edge of the crystal (Figure 3.5(b)).

The crystal growth rate was then calculated using Equation 2.26.

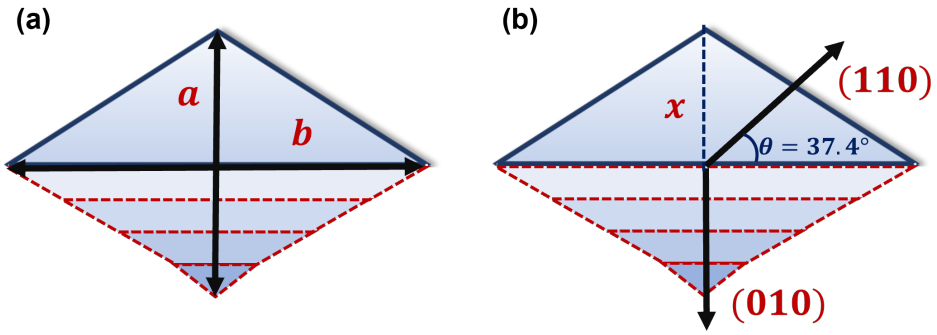


Figure 3.5: Diagram depicting the measurement of (a) Characteristic dimensions: length a and b (b) Facet propagation of (010) and (110), on a simplified drawing of a paracetamol crystal as viewed through the microscope and camera

3.7.1 Automated image analysis using MATLAB

To make the image analysis more efficient, a MATLAB (version R2023b) code was developed in house to measure the characteristic dimensions as well as the facet propagation of crystals. The basis of the script is essentially an edge detection algorithm that discretely identifies the crystal boundary, and therefore the desired dimensions.

The essential steps for successful edge detection are outlined below, with the primary MATLAB default functions emphasised in *italics*:

1. **Image cropping:** First the original Red Green Blue (RGB) i.e., coloured image, is cropped using the function *imcrop*, to remove the excess background such that the crystal occupies majority of the frame. Cropping the image depends on the measurement of interest. For characteristic dimensions, the entire crystal needs to be in the cropped frame. For facet-specific measurements, only the regenerating part should be considered for (010), while for (110), the non-regenerating part should be taken into account.

2. **Pre-processing of image:** Following this the image is converted into greyscale (*rgb2gray*) and treated with a median filter (*medfilt*) to remove any extra bright hotspots, 'noise'. As the crystal is mainly transparent, to improve the contrast with the background, the image is equalised using an adaptive histogram (*adapthisteq*). Meaning, multiple histograms are generated for the various parts of the image and eventually redistributed into a single histogram, such that tonal intensities of the image are evened out across the image.

3. **Conversion to binary image:** Following conversion into grayscale, the image is binarised: each pixel now has a value of either 0 (white) or 1 (black), with the objects of interest being the white pixels. This is achieved by thresholding the grayscale image. Each pixel on the grayscale has a value between 0 and 256, with 0 being the brightest pixel and 256 being the darkest. During thresholding these values are binned such that, pixels below a certain value are assigned a value of 0, whilst the ones above are assigned as 1. This binary image then undergoes morphological dilation followed by an erosion (*imclose*). During erosion, all the stray black pixels are removed whilst the small white pixels close to the edge of the white objects are incorporated into the object based on the specified constraints.

4. **Removal of undesired objects:** On certain occasions, even after histogram equalisation, there remain bright spots on the image due to reflections from the

glass rod (experimental set up detailed in Section 5.2.2), glass bottle, and even the crystal itself. These brigh spots get converted into white objects during binarisation and are engulfed into the crystal boundary. To remove them and prevent the script from overestimating the crystal size, a *watershed* function is used. This watershed function treats the image as a 2D surface and categorises bright areas as 'low' points and dark areas as 'high' points. The region where the two attached objects meet is treated as a dark area due to do the discontinuity in the boundary and sudden decline in white pixel density. This results in a line between the objects, thus detaching them. Finally, once all unwanted objects are detached from the crystal, a quick area selection is done to only keep the biggest object i.e. the crystal, in the frame.

5. **Determining crystal boundary:** To refine the edges of the binary crystal, its convex hull is calculated, using *bwconvhull*, such that a smooth shape, joining all the outermost pixels of the object, is created. At this point only one large white object remains in the image, of which the boundary is detected. This boundary is also superimposed on the original RGB image to confirm acceptable crystal edge detection.

6. **Measuring crystal dimensions using bounding box:** To measure the characteristic lengths or the facet propagation of the crystal, a minimum bounding box around the detected crystal boundary is drawn. This box has the smallest dimensions feasible in order to fit all the points of the crystal boundary. The length and width of the bounding box are therefore the measurements of interest.

7. **For-loop for processing image folder:** All the above steps are enclosed in a loop such that a folder containing all the images from one experimental condition can be analysed at once. As a result a plot of the crystal dimensions as a function of time is produced. The crystal dimensions are by default measured in pixels and therefore a calibration value needs to be inputted into the script in order to convert all measurements into millimetres.

Figure 3.6 depicts a summary of the image analysis script for a representative crystal image. The full code can be found in Appendix A.3

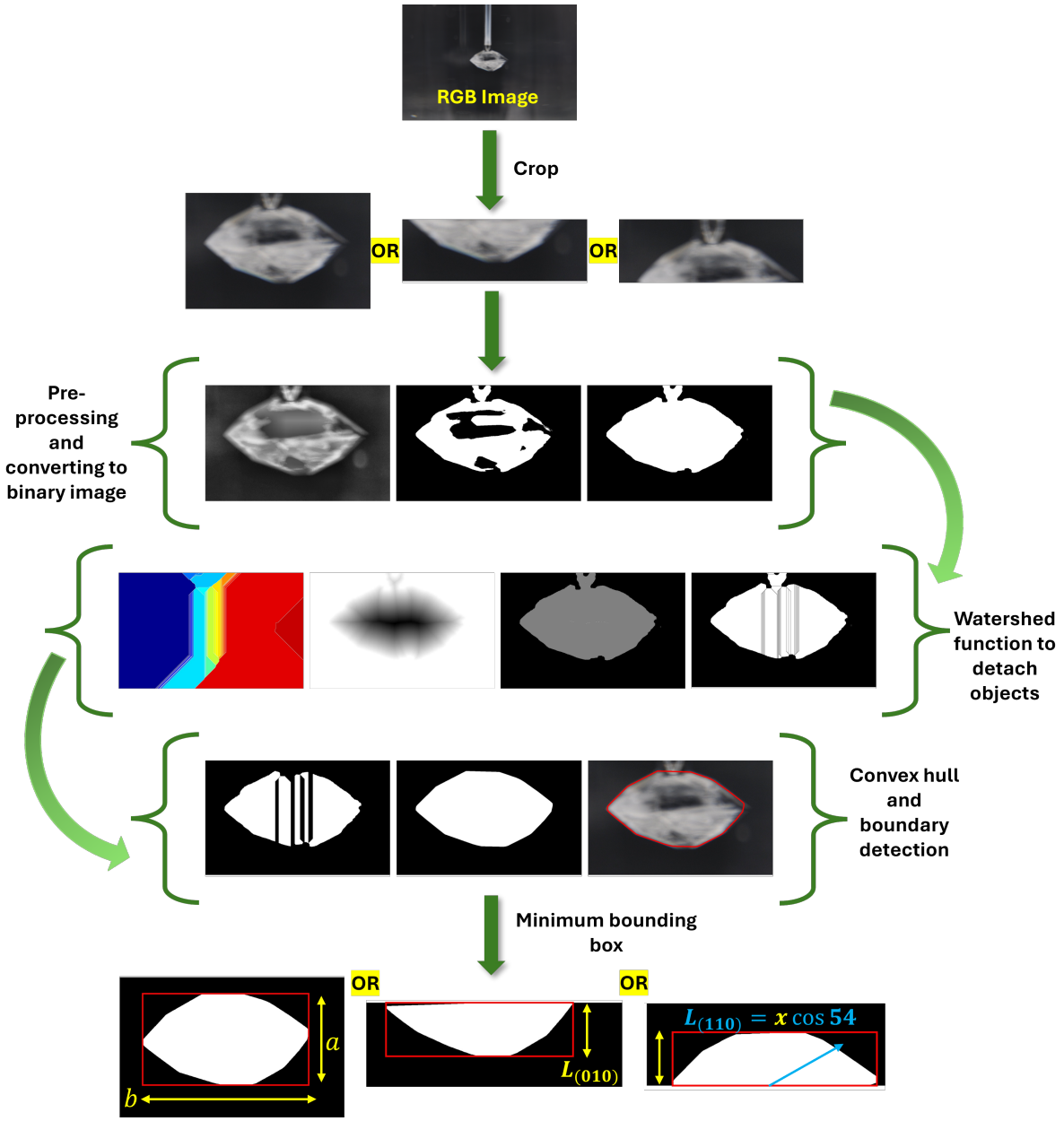


Figure 3.6: A summary of the steps used in the MATLAB script to analyse crystal images, starting from preprocessing into binary image all the way to edge detection and obtaining measurements

3.8 Characterisation techniques

3.8.1 Powder X-Ray Diffraction (PXRD)

Powder X-ray diffraction is commonly used to acquire diffraction patterns of powder samples in order to obtain information about their crystal structure [116, 110, 106, 217]. As high quality single crystals are not required for this technique, as in the case of single crystal X-ray diffraction (SC-XRD), PXRD is a convenient technique to check powder samples firstly for crystallinity as well as polymorphism. Due to the three dimensional regularity of atoms in crystals, all crystalline species will produce a diffraction pattern, distinct to the structure being investigated.

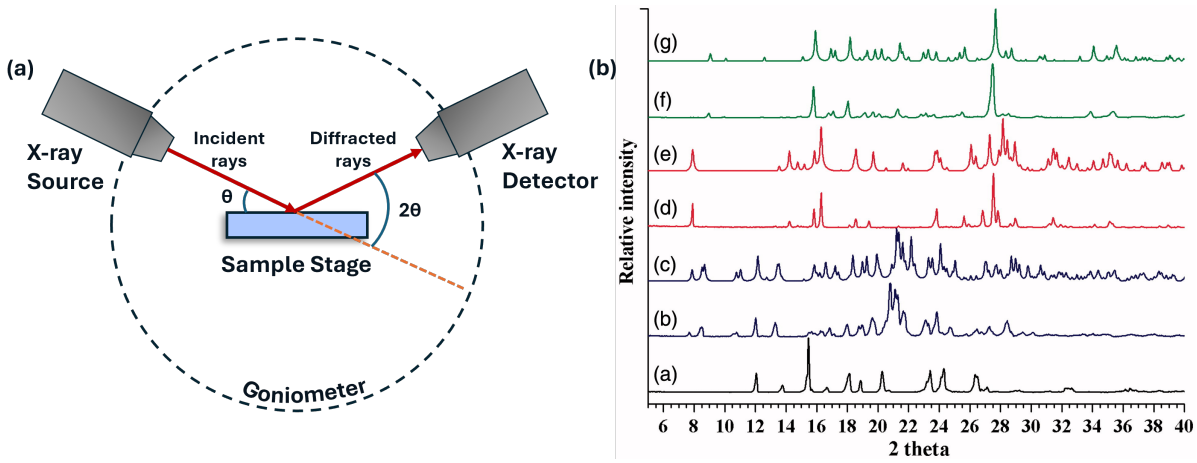


Figure 3.7: (a) Visual representation of the working principle of PXRD (b) Typical PXRD pattern obtained from a powdered sample of *(a)* form I paracetamol, and *(b)-(g)* its cocrystals and salts - image used with permission from [21]

The working principal of PXRD (Figure 3.7) involves producing electrons by heating up a tungsten filament in a cathode ray tube and accelerating them at a voltage of 10 kV to 60 kV towards a metal anode [218, 219]. The most commonly used metal anode is copper (Cu) and once in contact with the high energy electrons, the metal atoms ionise, consequently decelerating the electrons and emitting X-ray radiation. The Kα type of radiation is the strongest that is emitted, which has a wavelength, λ, of 1.5405 Å for Cu. This wavelength is filtered amongst another wavelengths to eventually be targeted at the sample. A goniometer sets the angle between the source, sample, and the detector. The

angle between the incident beam and the sample stage, θ, is varied, and depending on the interplanar spacing, d_{hkl}, of the crystalline plane, incident beam only at a specific angle will be diffracted. This diffraction will lead to the constructive interference of the waves such that Bragg's Law (Equation 3.3) is obeyed:

$$n\lambda = 2d_{hkl}sin\theta \tag{3.3}$$

Where n is the order of diffraction and is an integer (1, 2, 3,...), d_{hkl} is the interplanar spacing of the crystal facet, and θ is the X-ray incident angle.

PXRD investigations for this thesis was carried out using PANalytical X'Pert PRO X-ray diffractometer. As standard PXRD protocol, the crystals were ground to fine powder in a pestle and mortar to minimise any preferred orientation. The powder was then pressed flush against the sample holder using a glass slide to flatten it and excess powder on the edges of the holder was brushed off using soft tissue prior to being placed inside the machine. The X-ray diffraction measurement was performed using Cu Kα radiation (1.5405 Å) at 40 kV and 20 mA. All samples were conducted at a scanning rate of 50 seconds per step, with a step size of 0.013°, over a diffraction angle range from 5° to 35°.

3.8.2 Scanning Electron Microscopy (SEM)

To capture topographical details of a solid sample, SEM is a broadly used characterisation technique. As electron waves have drastically shorter wavelengths compared to light waves, SEM can capture finer details and achieve higher resolution images (2 nm) compared to an optical microscope. Electrons in an SEM are produced by heating up a tungsten filament, which are then accelerated using a voltage of upto 40 kV [220, 221]. This primary electron (PE) beam is focused onto the sample using an electromagnetic lens, which scans the sample surface in a pattern of parallel lines. Once in contact with the specimen, two types of scattering of the electron beam can occur; elastic and inelastic [222]. In the inelastic scattering, the PEs collide with the atoms in the sample, transfer-

ring their kinetic energy onto the atom's electrons and resulting in their emission. These are called secondary electrons (SEs) which are generally low in energy (<50 eV) and are picked up by specialised detectors that convert the electron intensity into an electrical signal. Hence, a grey scale image is generated where the brightness is proportional to the electron density and therefore the surface rugosity. Meaning, elevated points on the sample surface will result in more SE emission compared to the troughs of the surface, corresponding to the brighter and darker aspects of the image respectively. Elastic scattering on the other hand is when the PEs are reflected after interacting with the nuclei of a specimen atom. These are called backscattered electrons (BSEs) and are relatively high in energy as the PEs do not lose much kinetic energy during scattering [223]. The intensity of BSEs is directly proportional to the weight of the element, where a heaver element results in brighter spots on the image and vice versa. Therefore, BSEs are used to identify the elemental distribution on the sample surface [224]. The working principle of SEM can be seen in Figure 3.8(a).

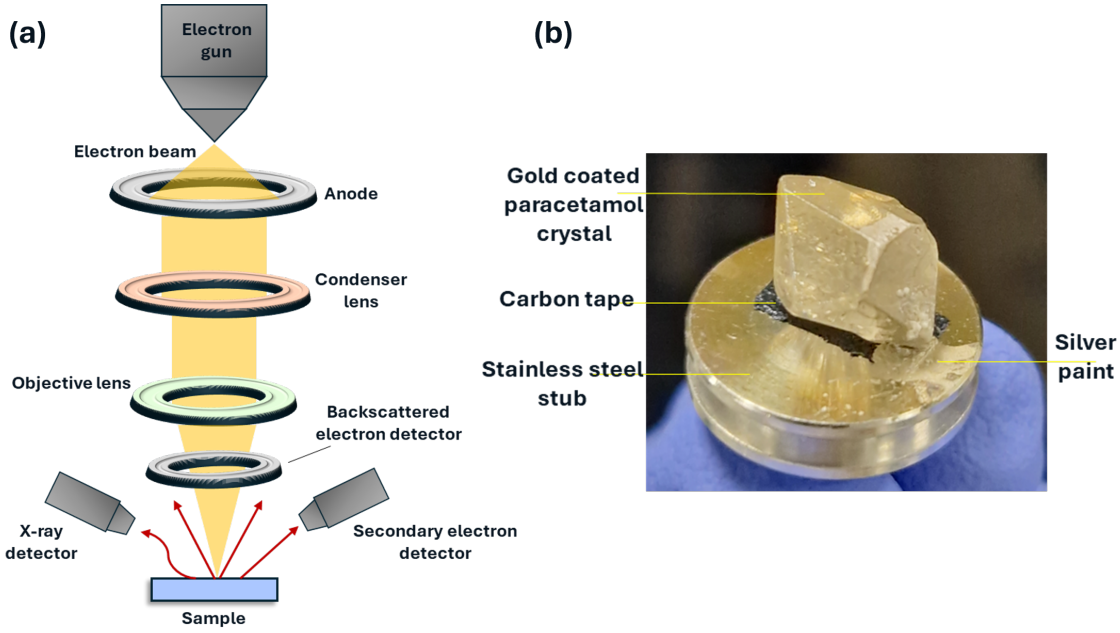


Figure 3.8: (a) Visual representation of the working principle of SEM (b) A macroscopic paracetamol crystal, coated in a thin layer of gold, and placed on a stainless steel stub using carbon tape in preparation for SEM imaging

SEM of paracetamol crystals was conducted using a JEOL 6010LA scanning electron microscope. Crystals were mounted on a stainless steel stub using carbon conductive

adhesive tape and gold coated in a Emitech K575X pumped coating system (Figure 3.8(b)). Coating was done at a sputter current of 20 mA for 30 seconds to obtain an Au coating of approximately 15-20 nm thickness. As the crystals are non-conductive, coating the surface with a layer of heavy metal inhibits charging of the sample and enhances SE emission. The gold-coated sample was then analysed with an accelerating voltage of 10 kV and at a working distance between 13-14 mm.

3.8.3 X-Ray Photoelectron Spectroscopy (XPS)

XPS is a widely used surface analytical technique which is based on the photoelectric effect described by Einstein [225, 226]. An X-ray source, typically a metal anode; aluminium (Al) or Magnesium (Mg), is used to irradiate the sample with low energy X-rays (6 keV). When X-ray photons reach the sample, electrons in the orbitals absorb the energy of the photon resulting in their emission. The binding energy of the electrons in the atom will depend on the element and orbital to which they belong. The kinetic energy of the emitted electrons is therefore a function of the energy of the photon, as well as the binding energy of the electron, and represented by the Equation 3.4:

$$E_{binding} = h\nu - E_{kinetic} - \varphi \tag{3.4}$$

Where $E_{kinetic}$ us the kinetic energy of the emitted photoelectron and is a known and fixed value depending on the instrument being used. $E_{binding}$ is the binding energy of the electron in the orbital, calculated using, $h\nu$, where h is the Planck's constant and ν is the frequency of the X-rays. φ is the constant work function, which the minimum energy required to remove an electron from a material at 0K. The emitted photoelectrons are analysed by a detector and their kinetic energy is measured, following which the binding energy is calculated. Figure 3.9(a) shows a diagram depicting the working principle of XPS.

A 'fingerprint' spectra is produced, which essentially presents the photoelectron counts

as a function of their binding energy (eV), and is useful to determine the elemental composition of the sample. More detailed spectra of a certain element is also produced such as the $C1_s$ spectra. The binding energy of core electrons will change depending on the bound state of the element. For example, increased oxidation state (removal of valence electrons) during bonding will increase the binding energy of the electrons and thus result in a shift in the XPS peaks [40, 227]. These unique binding energies for each bonding environment can be identified from the atomic spectra using databases such as the National Institute of Standards and Technology (NIST) database [228].

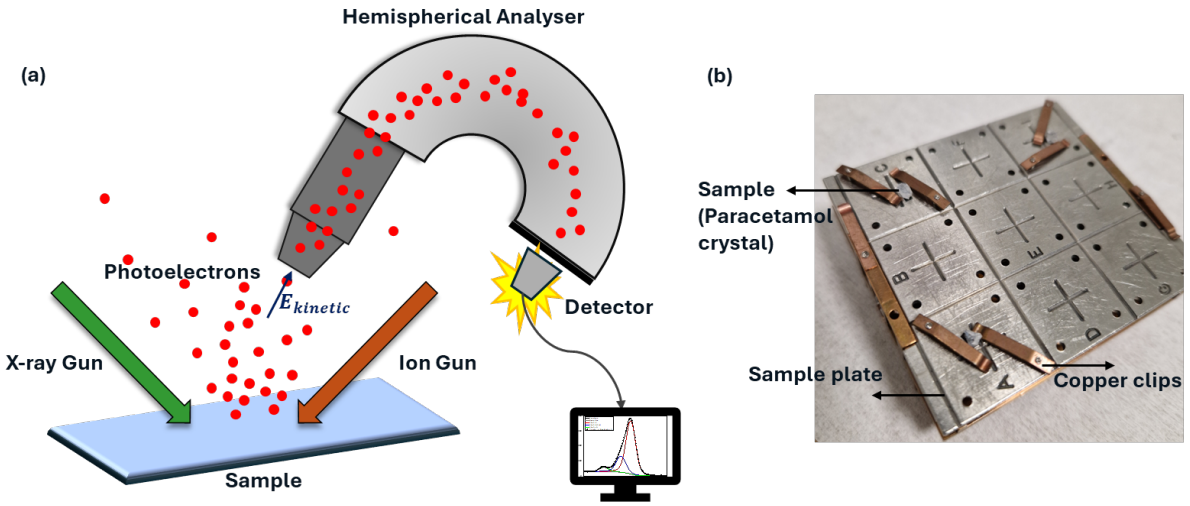


Figure 3.9: (a) Visual representation of the working principle of XPS and (b) paracetamol crystals mounted on a sample holder in preparation for XPS

XPS was performed on the 5 major facets of paracetamol form I; (001), (010), (110), (011) and (201), using Thermo Fisher K-Alpha+ that uses a Monochromated Al Ka Micro-focused X-ray source. A strong agreement was observed between the experimentally determined crystal habits and those reported in the literature [40, 157]. Facets were identified by superimposing the experimental habits onto those from previous studies. Additionally, the facets were further verified by measuring their dihedral angles under a microscope which were compared to those calculated during the vacuum morphology prediction (Section 3.9.3), rendering Single Crystal X-ray Diffraction (SC-XRD) unessential. Paracetamol crystals were stuck on a stainless steel plate mounted on a copper holder (Figure 3.9(b)), under an hour of taking out from solution to minimise exposure to the environment. Crystals from the same batch were used and mounted at angles such that

the desired facet was parallel to the plate and therefore in direct path of the X-rays. This was achieved by using crystals with a facet area of around 9 mm^2 that were mounted on the plate using carbon tape and copper clips. Moreover, flood gun was on at all times to minimise surface charging due to the X-rays. Multipoint analysis was carried out by scanning 5 randomly chosen points of spot size 400 µm on every facet and the $C1_s$, $O1_s$ and $N1_s$ spectra were acquired at 20 eV pass energy. All spectra were Shirley background subtracted and peak fitted using a Lorentzian/Gaussian (25:75) mix. Fitting was carried out using the Thermo Avantage V5 software using minimum number of peaks required to minimise R-factor. The quantitative analysis carried out for each facet was averaged over the 5 points and the standard deviation was calculated.

3.8.4 Nanoindentation

Nanoindentation is a common technique used to measure the hardness and elastic modulus of solid materials [229]. Although it is widely used for inorganic materials, the use of nanoidentation to measure the mechanical properties of the organic crystals is rapidly gaining traction [199, 230]. Data is obtained by pressing an indenter tip into the sample surface using a specified amount of load, P (mN), and rate (mN/s). The material and geometry of the tip depends on the solid being characterised, however in the case of organic crystals and hence in this study of paracetamol crystals, a diamond Berkovich pyramidal tip is used. During the test, a load (mN) against displacement (nm) curve (P-h curve) is produced to show the loading and unloading profile of the tip as it digs into the surface and eventually pulls out. The loading and unloading data is generally fitted using a power law fit, also known as the Oliver and Pharr fit [231]. A representative P-h curve can be seen in Figure 3.10, using which the hardness (H), and reduced modulus (E_r) are calculated with the following equations:

$$H = \frac{P_{max}}{A} \tag{3.5}$$

Where P_{max} is the maximum indentation load, and A is the projected contact area, estimated using Equation 3.6 for a Berkovich indenter:

$$A = 24.56 \times {h_c}^2 \tag{3.6}$$

Where h_c is the contact depth, defined as the depth of the indenter in contact with the sample under load, but corrected for the extra depression of the sample around the indentation [232]. Equation 3.6 is an empirical equation found by performing a series of indentations at different depths on a material of known modulus, mostly Quartz, and measuring the contact area at each of these depths [231].

The elastic modulus of the material of interest can also be measured by first calculating the reduced modulus (E_r) of the system. The reduced modulus accounts for the elasticity of the material as well as the identer tip and is found using the equation:

$$E_r = \frac{\sqrt{\pi}}{2} \times \frac{S}{\sqrt{A}} \tag{3.7}$$

Where S is the gradient of the tangent of the unloading curve. The value of E_r can further be used to calculate the material's elastic modulus as follows:

$$E = \frac{1 - \nu^2}{\frac{1}{E_r} - \frac{1-{\nu_i}^2}{E_i}} \tag{3.8}$$

Where E and ν are the Young's modulus and Poisson's ratio of the material,whilst E_i and ν_i are the equivalent for the indenter.

The hardness and Young's modulus of the different facets of single paracetamol crystals were measured to study their mechanical properties post regeneration. The Micro Materials SPM Nanopositioner was used to perform indentations, which were analysed by the NanoTest Vantage software. Indents were made using the Berkovich diamond indentor with a maximum load of 5 mN at a loading and unloading rate of 0.5 mN/s as well as a dwell time of 10 s. On each facet 9 indents were made in the form of a 3×3 grid, with 50

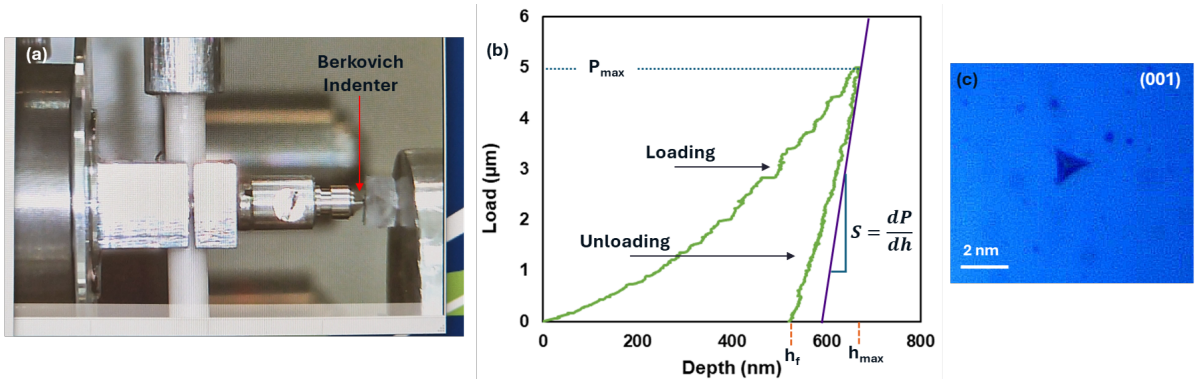


Figure 3.10: (a) Paracetamol crystal being indented in the SPM nanopositioner using a Berkovich diamond tip (b) A representative Load vs depth (P-h) curve showing the loading and unloading profiles fitted using the Oliver and Pharr fit, where h_f and h_{max} are the final indentation depth and indentation depth at maximum load respectively (c) representative image showing the pyramidal indent post tip unloading on a paracetamol facet

μm spacing between each indent. 3 different crystals were tested for every desired facet, such that an average H and E was calculated for every facet along with the standard deviation.

3.9 Computational Methods

Computational studies with context to this thesis were carried out as a means to aid the discussions leading on from the experimental findings. Therefore, the following tools were used to provide validation to the conclusions drawn from the experimental observations rather than provide any fundamental quantitative information.

3.9.1 Cambridge Structural Database (CSD)

For all computational studies, crystal structure of monoclinic form I paracetamol was obtained from the Cambridge Structural Database (CSD) (refcode: HXACAN01 [192]), of space group $P2_1/a$ with lattice parameters: $a = 12.93$ Å, $b = 9.40$ Å, $c = 7.10$ Å and $\alpha = 90°$, $\beta = 115.9°$, $\gamma = 90°$, with four paracetamol molecules in the unit cell. For the metastable orthorhombic form II, HXACAN21 [233] was used with unit cell parameters

$a = 7.1986$ Å, $b = 11.782$, $c = 17.183$ Å, and $\alpha = \beta = \gamma = 90°$, of Pcab space group.

3.9.2 CSD Mercury

Mercury (version 2024.1.0, CCDC, Cambridge, U.K.) was used to predict the powder XRD patterns of form I and form II paracetamol, HXACAN01 and HXACAN21 respectively (Section 3.9.1). Moreover, to better visualise the molecular arrangement in the crystallographic planes of interest, the embedded 'Packing and Slicing' tool was used. Using this tool, the packing along any facet could be viewed across the desired area and depth.

CSD-Particle BFDH Morphology

The BFDH morphology of form I paracetamol (HXACAN01) was calculated using the 'Morphology' tool on Mercury. This was predicted based on the interplanar spacing, d_{hkl}, and therefore the slow growing facets with the highest d_{hkl} occupied a larger proportion of the crystal surface area and vice versa. The theory behind the morphology prediction using BFDH rules can be found in Section 2.3 of the literature review.

CSD-Particle Surface Analysis

The 'VisualHabit' tool was used to predict the morphology of form I paracetamol (HXACAN01) in order to isolate and analyse the the various planes of the crystal. The 'Surface Analysis' tool on Mercury allows visualisation and quantification of the surface properties of the desired crystal plane. Here the h,k,l values of the desired plane were inputted, based on which a slab of wanted thickness and length is generated. The tool then analyses the surface properties of the slab and the following information was outputted:

1. *Topology:* This calculates the 'projected area (Å^2)' of the surface, i.e., the total surface area of the surface based on the initially specified size, and the 'surface area

(Å^2)', calculated based on the physical properties of the surface. If the surface has multiple peaks and troughs due to the orientation of chemical moieties, the surface area will be large compared to a flatter surface. Therefore based on these values, the 'rugosity' is calculated using the equation:

$$\text{Rugosity} = \frac{\text{Surface Area}}{\text{Projected Area}} \tag{3.9}$$

2. *Atom properties:* The density information of the chemical functionalities of the surface are calculated. This includes the density of aromatic bonds, hydrogen bond donors, hydrogen bond acceptors, and the unsatisfied hydrogen bond donors on the surface, in the units, number/Å^2.

3.9.3 Accelrys Materials Studio 7.0

This software was used to predict the vacuum morphology of form I paracetamol (HXACAN01) and perform Molecular Dynamic (MD) simulations.

Forcefield selection

All simulations were performed in Accelrys Materials Studio 7.0 software. Prior to any simulations, the crystal structure was geometry optimised using the 'Forcite' module using 3 forcefields: COMPASS II [234], Drieding [235], and Universal [236], that are commonly used for organic molecules. COMPASS II was chosen as the forcefield going forwards as the relative error associated with the optimised cell parameters was the least (Table 3.1).

Table 3.1: Lattice parameters of HXACAN01 before and after optimisation using COMPASSII forcefield and the associated relative error

Lattice parameter	*a* **(Å)**	*b* **(Å)**	*c* **(Å)**	*β* **(°)**
Initial	12.93	9.40	7.10	115.90
COMPASS II opt.	12.65	8.86	7.24	114.76
Relative error (%)	2.16	5.74	1.97	0.98

Vacuum morphology

Following geometry optimisation, the crystal habit in vacuum was predicted using the 'Morphology' tool in Materials Studio. The 'Growth Morphology', which is based on the AE model, was executed using the COMPASS II forcefield and a list of important facets that determine the morphology was obtained.

Interaction energy calculation

Based on the vacuum morphology, the crystal was cleaved parallel to the (010) surface and a periodic supercell of 3 × 3 unit cells and 4 × d_{hkl} depth was created. The solvent layer was then constructed using the 'Amorphous cell' tool by creating a cell of 400 randomly distributed solvent molecules of the desired solvent; ethanol, acetone and THF. The dimensions of the solvent layer were chosen to match that of the superstructure of the crystal surface and the target density was set to the solvent density at room temperature (298 K): ethanol – 0.789 g/cm^3, acetone – 0.784 g/cm^3, and THF – 0.888 g/cm^3. The amorphous layer was then subject to geometry optimisation and cell relaxation by molecular dynamics using the NVT ensemble at 298 K for 300 ps controlled by the Anderson thermostat [237]. The NVT ensemble ensures that a constant number of moles, volume, and temperature of the system is maintained. Subsequently, a bilayer was built with the solvent layer placed above the crystal surface along the c axis. A 50 Å vacuum slab was placed above the solvent layer to avoid the effect of additional free boundaries. All except the topmost layer of the crystal were fixed along the *a*, *b*, and *c* directions. The entire system was then geometrically optimised and the MD was assessed by the Anderson thermostat using the NVT ensemble at 298 K with a step time of 1 fs. The

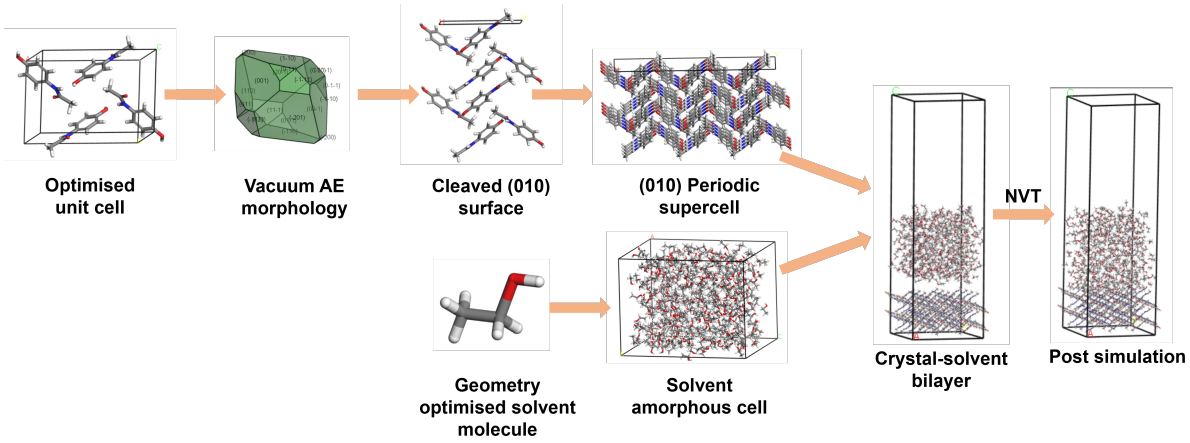


Figure 3.11: Diagram summarising the MD simulation set-up on Materials Studios for calculating the surface-solvent interaction energy

electrostatic interactions were calculated using the Ewald method with an accuracy of 0.0001 kcal/mol, whilst the atom-based summation method with a cut-off distance of 15.5 Å was used van der Waals forces. Two sets of MD simulations were run, first to equilibrate the whole system for 100 ps followed by another MD simulation for 50 ps to obtain the energy values. Figure 3.11 shows a schematic representation of the simulation approach for this study.

The total potential energy, E_{tot}, of the simulated crystal-solvent layer was used to the calculate the interaction energy, E_{int}, using Equation 3.9.3:

$$E_{int} = E_{tot} - (E_{cry} + E_{sol}) \tag{3.10}$$

Where E_{crys} and E_{sol} are the energy of the crystal and solvent layer respectively.

Chapter 4

Crystal regeneration - a proposed growth mechanism in crystals post breakage

4.1 Overview

This chapter introduces the phenomenon of 'crystal regeneration' and establishes the groundwork for the subsequent chapters of this thesis. Here, imaging setups compatible with evaporative crystallisation were developed to monitor the growth of macroscopic single crystals of paracetamol. The study revealed that a cleaved paracetamol crystal exhibited a remarkable ability to restore its original shape via rapid growth of the cleavage plane (010) and, once restored, growth resumed in the same fashion as prior to breakage. This extrinsic self-healing behaviour was found to be influenced by the direction of the breakage, with crystals broken parallel to the cleavage plane exhibiting regeneration, while those cut perpendicular did not. Characterisation techniques, such as PXRD, SEM, and nanoindentation, also confirmed that the regenerated crystals retained the original form, shape and mechanical properties from before breakage.

Quantitative analysis demonstrated that during regeneration, growth perpendicular to facet (010) occurred approximately thrice as fast (0.06 mm/hr) than in unbroken crystals (0.024 mm/hr), whilst that parallel to the cleavage plane occurred at the same rate as unbroken crystals. Moreover, the majority of the regeneration process took place in the initial duration of the experiment, where the length perpendicular to (010) doubled in size, as opposed to a mere 20% increase each following day. Thus a two-phase regeneration mechanism has been proposed: an initial rapid regeneration phase followed by a slower one.

This discovery challenges conventional morphology prediction theories, which suggest that fast-growing facets, due to their rapid growth surpassing slower-growing facets, do not contribute to the crystal habit and are therefore disregarded in crystal growth. While this principle may apply to unbroken crystals, the study emphasises that in broken crystals, fast-growing facets play a dominant role in the regeneration process and cannot be dismissed as insignificant. The chapter concludes with a discussion of the potential factors contributing to this anomalous behaviour, including surface energetics, synthonic interactions within the crystalline lattice, as well as the implications of regeneration on the crystal properties.

4.2 Methods

4.2.1 Obtaining and cutting paracetamol crystals

Paracetamol and ethanol were the only two chemicals used in this study, the details of which can be found in Section 3.1. Macroscopic single crystals of paracetamol were grown in an ethanolic solution as elaborated in Section 3.3. To investigate the effects of the extent and orientation of breakage, a few different types of cuts were implemented on the paracetamol crystals, as summarised in Figure 4.1. Firstly, the crystals were cleaved using the same approach as detailed in Section 3.4. This was to cut the crystal in two

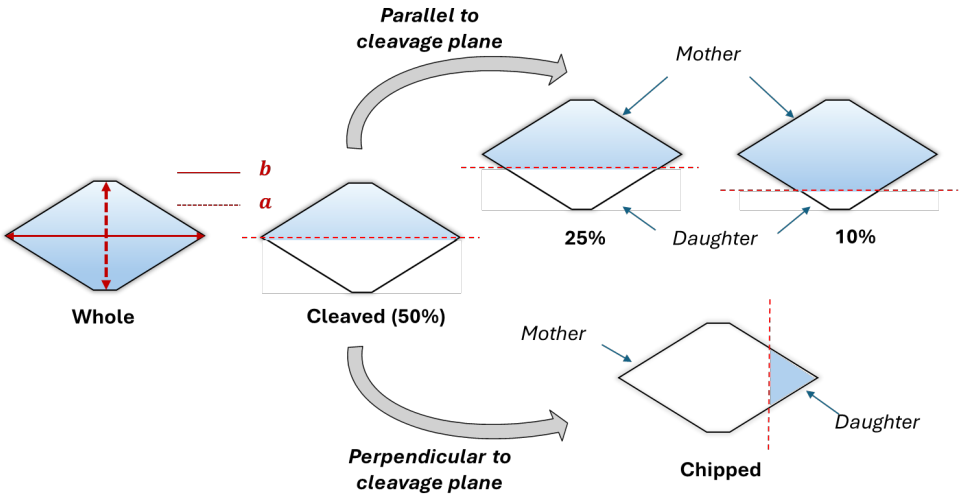


Figure 4.1: Summary of the extent and orientation of breakage studied: parallel to the cleavage plane - 50% (cleaved), 25%, 10% and perpendicular to the cleavage plane - chipped. Note: The crystal diagrams are simplified representations of a paracetamol crystal as seen through the microscope and camera. For a comparison with the actual crystal, please refer to Figure 3.3.

clean halves, also known as the 50% cut. To achieve the 25% and 10% cut, point pressure was applied on facet (011) approximately 25% and 10% respectively from the edge of the crystal, such that breakage was parallel to the cleavage plane. Finally, the crystal was 'chipped' by cutting the crystal perpendicular to the cleavage plane. This was done by going back and forth on the (001) facet in the b direction, using a scalpel, until two fragments were produced. The original crystal after breakage is referred to as the 'mother' while the fragmented piece is termed as the 'daughter'.

4.2.2 Bench top optical microscopy for small crystals

The pre-prepared cut crystal was placed in a 50 ml crystallisation dish, which was filled with 25 ml of saturated solution of paracetamol and ethanol prepared at room temperature. The dish was covered with a glass lid that resulted in an overhang of 1 cm. To prevent rapid solvent evaporation, parafilm was used to seal the edges of the enclosed dish, which was then placed in a fumehood for a week-long evaporation period. Every 5 hours during the day, crystal images were taken using a Leica stereomicroscope (Figure 3.4(a)). To better elucidate the regeneration phenomenon, the growth of small unbro-

ken whole crystals was also investigated in the same manner to eventually compare the growth rates of broken and unbroken crystals. Three cleaved and three unbroken crystals were studied and average growth rates were calculated. Leica Application Suite (LAS) 4 software was used the analyse the images and measure the characteristic dimensions, length a and length b of the crystals (Section 3.7), to eventually calculate the growth rates using Equation 2.26.

4.2.3 Macro photography for large crystals

The large crystals used were almost double in size compared to the small crystals thus making microscopic imaging techniques substandard. A more adequate imaging rig was designed that utilised a macrophotography approach. The cut crystals were hung in solution as described in Section 3.3, with the freshly exposed plane facing the base of the vial, and allowed to grow via slow solvent evaporation. A Nikon D90 DSLR camera attached with a Nikon AF-S 18-105 mm lens and 68 mm Newer extension tubes was used to take high resolution macro photographs. Due to the prismatic and transparent nature of the paracetamol crystal as well as the use of a clear solution and cylindrical glass vials to suspend the crystal, controlling the lighting for the set-up was crucial to minimise reflection and glare in the images. Hence, the vials were kept inside a photography light box, embedded with LED lights and a diffuser cloth for even dispersion of light. The camera was then pointed directly at the vial, with a front view of facet (001) directly in frame. Images were taken every 30 mins over a period of 2-2.5 weeks using a timer connected to the camera (Figure 3.4(b)). Using these images the characteristic lengths a and b (Section 3.7) of three cleaved crystals were measured with the aid of Image J and average growth rates were calculated using Equation 2.26.

4.2.4 Powder XRD

Powder XRD patterns of as received paracetamol powder, paracetamol seeds grown from ethanol, and crystals before and after regeneration were obtained using the methodology outlined in Section 3.8.1.

4.2.5 Scanning electron Spectroscopy

SEM of paracetamol crystals was carried out using the methodology detailed in Section 3.8.2. The aim was to image the (010) facet at various time points during the regeneration process. Hence the (010) facet was imaged before placing the cleaved crystal in solution (0 hours), 25 hours, and 50 hours. These were obtained by removing the partially regenerated crystals from solution at the desired time to quench their growth, followed by quickly patting them dry with a soft tissue. It is important to note that images for every time point correspond to a different single crystal. This is because, post SEM, crystals cannot be put back in solution firstly due to their gold coating and secondly, they have been exposed to the atmosphere which will inevitably affect their growth.

4.2.6 Nanoindentation

To investigate the effect of regeneration on the mechanical properties of crystals, nanoindentation was performed on two major facets of paracetamol; (001), and the freshly cleaved (010). For each facet, 3 whole and 3 regenerated crystals were studied and measurements were carried out using the methodology detailed in Section 3.8.4.

4.2.7 Computational methods

The attachment energy habit i.e., the vacuum morphology of form I paracetamol was obtained via Material Studios using the methodology detailed in section 3.9.3. Moreover,

the BFDH morphology as well as the surface analysis of the five major facets of paracetamol, (001), (010), (201), (011), and (110) was performed with the aid of Mercury (Section 3.9.2).

4.3 Results

4.3.1 Identifying cleavage planes of form I paracetamol crystals

Although (010) has been identified as the weakest plane/slip plane/cleavage plane in multiple publications ([238, 239, 240, 171]), there is immense ambiguity in the classification of these planes and at most times these words are used interchangeably. As detailed in Section 2.4.2, slip planes and cleavage planes have different properties and therefore an attempt has been made here to distinguish (010) as the cleavage plane of paracetamol using the decision making process outlined in Section 2.4.2. This nomenclature and classification is crucial so that the regeneration phenomenon can be attributed to a particular type of facets.

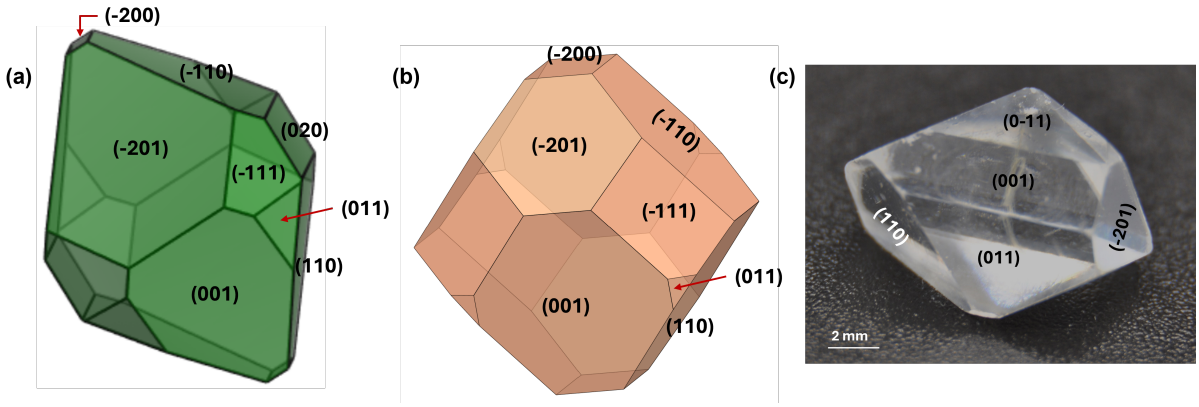


Figure 4.2: (a) Vacuum habit of form I paracetamol (HXACAN01) predicted by the attachment energy theory using Materials Studio (b) BFDH morphology of paracetamol calculated using Mercury (c) Experimental habit of paracetamol crystal grown in ethanol

As can be seen from Figure 4.2 (c), the experimental habit of paracetamol from ethanol is in excellent agreement with the literature [40, 142, 240, 239]. Facet indexing was done based on the habits reported in the aforementioned studies and therefore the four major

facets: (201), (001), (011), and (110) were identified. The facet (010) occupies negligible to no surface area of the experimental habit and is only exposed when the crystal is cut perpendicular to the (001) facet [239, 40].

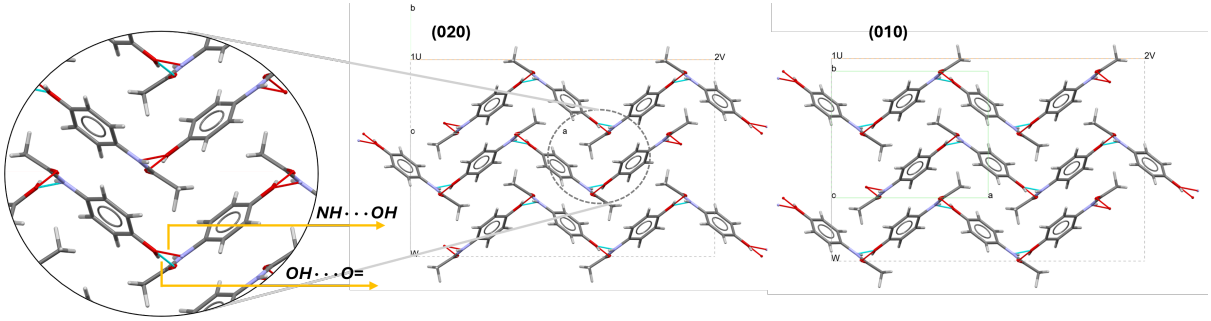


Figure 4.3: Depiction of the packing of corrugated (010) and (020) planes, highlighting the hydrogen bonding in the a and c direction

The attachment energy habit is generally in good agreement with the experimental habit of paracetamol (Figure 4.2 (a)). A 'prismatic' crystal shape is observed with major facets (110), (001), (201), and (011), (020), (111), and (200). Due to the effect of solvent environment and crystallisation conditions, some of these facets have no morphological importance on the experimental crystal habit. The attachment energy habit produced the (020) facet instead of the (010) facet. Following examination of the packing of the two planes on Mercury, not only were the two planes parallel to each other as they intersect the b axis, but they also expressed the same chemical moieties on the surface. The only difference being that the chemical groups were a mirror image of each other because the monoclinic form of paracetamol has an 'a-glide' plane, therefore (010) was just a reflection of the (020) plane along the plane intersecting the a axis (Figure 4.3). The (020) facet intercepts the b axis at 1/2 whilst the (010) at 1, thus the d spacing of the (010) will be larger than (020). The same explanation is true for facets (200) and (100) or (001) and (002) as they are all part of the same family of planes {100} as elaborated in Section 2.3.1. However when the BFDH morphology of the monoclininc paracetamol was computed, neither the (010) nor the (020) facets were observed (Figure 4.2 (b)), consolidating that both the facets still have the lowest interplanar spacing compared to the other major facets. Therefore due to these similarities in the 2 planes, (020) from the attachment energy habit was considered to be equivalent to the (010) facet. Table 4.1

Table 4.1: Interplanar spacing, d_{hkl}, attachment energy, E_{att}, specific interaction energy (SIE), and total facet area, of the major facets of the vacuum habit of paracetamol as obtained from Materials Studio

hkl	**Multiplicity**	$\boldsymbol{d_{hkl}}$	$\boldsymbol{E_{att}}$	**SIE**	**Total facet area**
		Å	kcal/mol/unit cell	kcal/mol/Å^2	(%)
(110)	4	7.01	-54.62	0.94	41.94
(001)	2	6.58	-68.09	1.10	14.41
(200)	2	5.74	-82.36	1.17	1.40
(201)	2	5.66	-53.11	0.74	22.56
(111)	4	5.56	-70.51	0.97	7.59
(011)	4	5.28	-74.42	0.97	3.16
(020)	2	4.30	-57.23	0.61	8.95

highlights the major facets on the vacuum habit of paracetamol in order of the percentage surface area they occupy, from highest to lowest along with their multiplicity, d-spacing (d_{hkl}), and attachment energy (E_{att}). The specific interaction energy (SIE) has also been calculated using Equation 2.29.

It can be seen that the (020) facet has the lowest interplanar spacing however a moderate attachment energy compared to other facets. This contradicts the attachment energies found by Prasad et al. in 2001 using the MOMANY molecular potential [239], where (010) was found to be the lowest attachment energy plane and therefore most likely to slip. This discrepancy was postulated to be due to advancements in the development of forcefields over the years as recent studies [171] have confirmed that attachment energy calculations using various forcefields, does not yield in a low attachment energy (010) plane for form I paracetamol. Thus, based on these findings, an initial approximation can be made that (010) is more likely to cleave than demonstrate slip.

Detailed surface analysis of the major facets was performed using Mercury (Section 3.9.2) as seen in Figure 4.4 to elucidate the surface rugosity and chemistry, results of which can be found in Table 4.2. Form I of paracetamol has been reported to have extremely corrugated and interpenetrating planes due to its herringbone lattice [19]. Relative to other facets, (010) has the highest rugosity, almost 15% higher than the flattest (201) facet. Therefore with lowest specific interaction energy, and high corrugation makes (010)

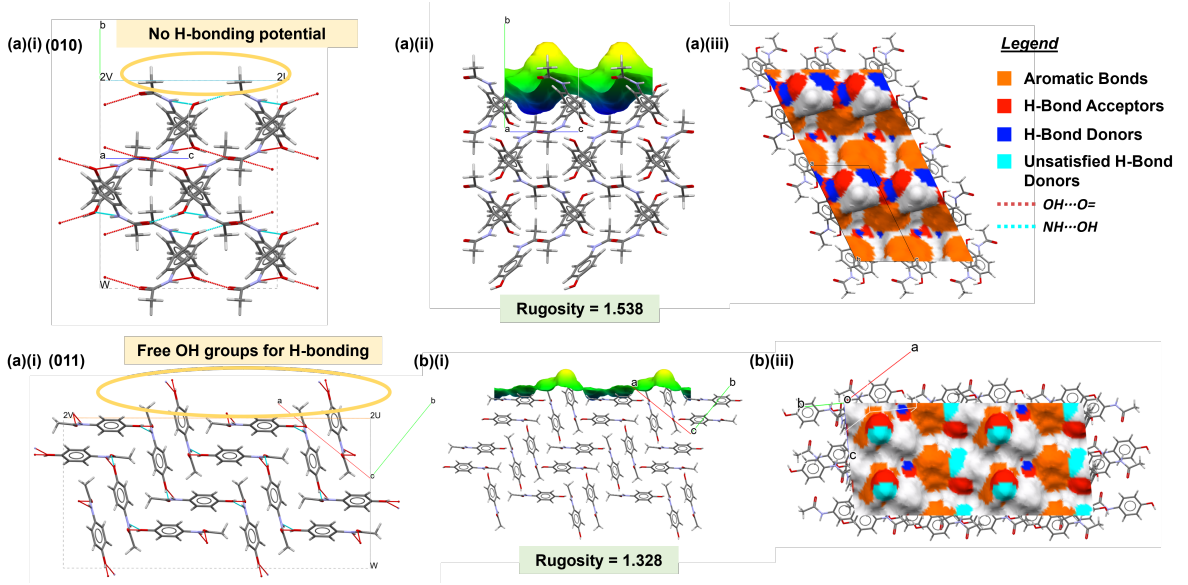


Figure 4.4: Analysed surfaces of planes (a)(010) and (b)(011) as obtained from Mercury depicting the (i) packing and hydrogen bonding, (ii) topological information, and (iii) surface chemical functionalities

Table 4.2: Surface analysis results including rugosity and the density of chemical moieties of the major facets of form 1 paracetamol

(hkl)	**Rugosity**	**Aromatic Bonds** counts/Å	**H-Bond Acceptors** counts/Å	**H-Bond Donors** counts/Å	**Unsatisfied H-Bond Donors** counts/Å
(201)	1.304	0.081	0.029	0.029	0.015
(011)	1.347	0.109	0.034	0.027	0.014
(110)	1.348	0.094	0.038	0.028	0.019
(001)	1.419	0.107	0.016	0.033	0.016
(010)	1.538	0.145	0.048	0.048	0.000

a brittle plane and, consequently, most susceptible to cleavage (Section 2.4.2).

The hydroxyl (OH) groups in a paracetamol molecule participate in hydrogen bonding by accepting a hydrogen bond from the amine (NH) group and donating it to the carbonyl (=O) group of an adjacent molecule, forming criss-cross layers in the a and c crystallographic directions (Figure 4.3). This leaves no hydroxyl groups available for hydrogen bonding along the b axis, hence leaving (010) with 0 hydrogen bonding potential where only methyl groups (-CH_3) protrude from the surface (Figure 4.4). The corrugated lattice as well as no hydrogen bonding potential makes (010) not only a brittle plane but also a apolar, weakly interacting plane. Therefore, the (010) plane is classified as the brittle

cleavage plane in a Form I paracetamol crystal. This plane is inherently a fast-growing facet, which is why it does not appear on the external crystal habit.

4.3.2 Effect of extent and orientation of breakage on regeneration

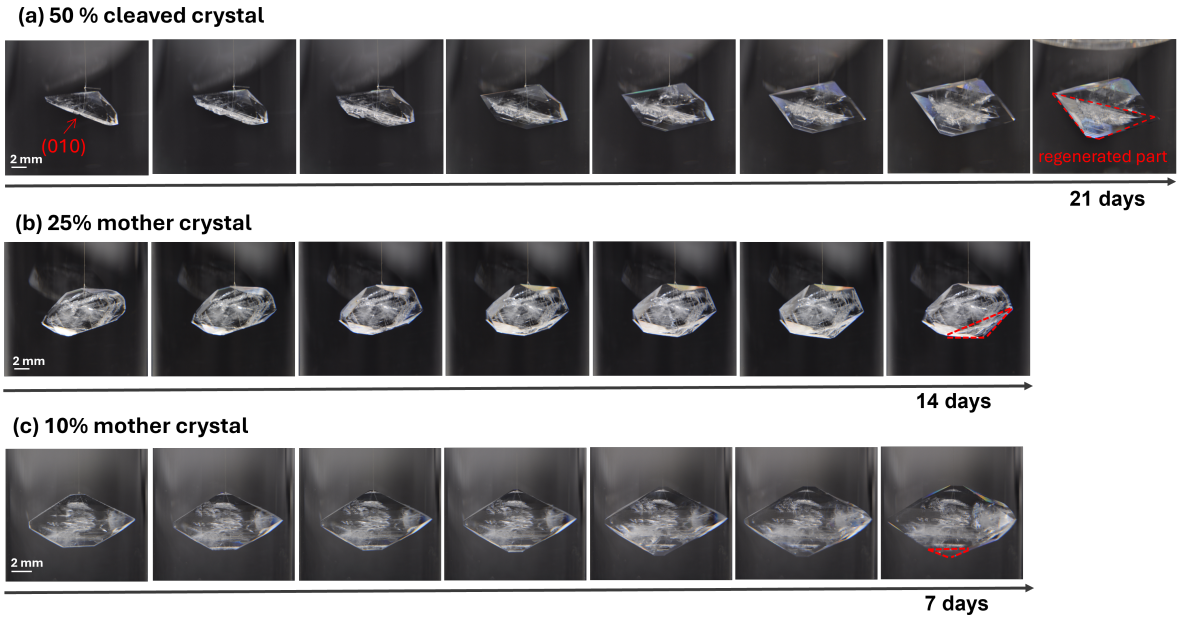


Figure 4.5: Regeneration observed in (a) 50% cleaved, (b) 25% mother, and (c) 10% mother paracetamol crystal

It was observed that regardless of the initial crystal size, cuts parallel to the cleavage plane resulted in regeneration (Figure 4.5 (a)-(c)). The cleaved (50%), 25% mother and 10% mother crystal regenerated their broken part and returned to their original shape. Crystals with a low degree of fracture demonstrated quicker repair such that the order of regeneration completion was as follows: 10% mother, 25% mother, 50% mother. This was due the low overall solute demand for smaller cuts. The daughter crystals from the parallel cuts also exhibited regeneration (Figure 4.6 (a)). However in this case, instead of the large mother segment reappearing on the crystal, it was more energetically favourable for the daughter fragments to regenerate into small whole crystals and eventually grow bigger. On the contrary, crystals that were cut perpendicular to the cleavage plane did not exhibit regeneration (Figure 4.6 (b)). Rather, they retain an overall shape similar

to the one spawned as a result of the breakage. Facets corresponding to the equilibrium morphology developed in accordance with the new shape and the crystal simply grew larger.

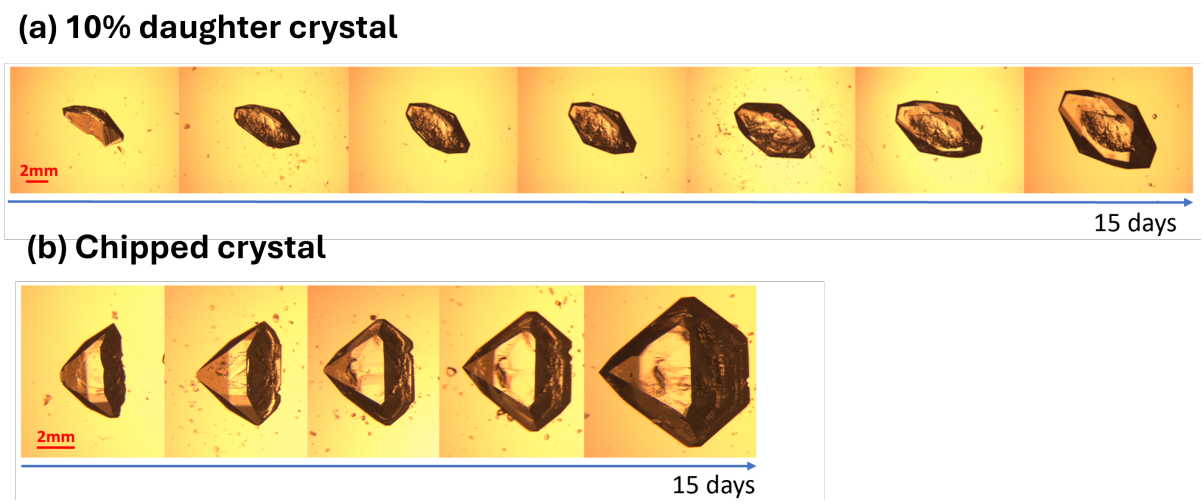


Figure 4.6: (a) Regeneration observed in a 10% daughter paracetamol crystal and (b) Growth behaviour of a chipped paracetamol crystal

This was postulated to be due to the plane exposed after breakage. In the case of 50%, 25% and 10% cut crystals, the plane parallel to the cleavage plane, i.e., a surface from the (0k0) set of planes, is exposed, resulting in analogous regeneration behaviour. However with the chipped crystals, no specific facet is exposed. Unlike the previous cuts, this type of breakage does not result in a 'clean' cut and requires moving the scalpel back and forth multiple times to slice through the crystal. This results in a surface that is an amalgamation of different facets and hence does not propagate as a traditional facet.

These observations emphasise the importance of the extent and orientation of breakage on the shape evolution of the crystal. Depending on the type of breakage, the eventual crystal shape and size can vary and result in undesired crystal shapes that can further hinder downstream processes.

4.3.3 Growth rates of cleaved crystals vs. unbroken crystals

Figures 4.7 (c) and (d), show plots of the average growth data obtained for small cleaved and small whole crystals respectively. The measured dimensions of length a and b were normalised, L_{norm}, to the total change in the characteristic dimension at the end of 325 hours, $L_f - L_i$, using Equation 4.3.3, for better visual representation of the growth trajectory.

$$L_{norm} = \frac{L - L_i}{L_f - L_i} \tag{4.1}$$

Where L_i and L_f are the initial and final length of the characteristic dimensions.

The end of regeneration was deduced visually at the point where crystal shape restoration is achieved (Figure 4.7 (a)) and is further consolidated using the gradients of the growth plot. In Figure 4.7 (c), at 100 hours, the change in the gradient of the curve for length a aligns with the end of the regeneration phase observed in the images, after which overall growth begins. After 168 hours, the cleaved crystal exhibits negligible growth, likely due to solute depletion caused by prolonged evaporation. Therefore, only the growth period between 100 and 168 hours was considered for analysis. For a consistent comparison, the growth of a whole crystal was also evaluated up to 168 hours, as shown in Figure 4.7 (b) and (d). Thus, further analysis on the growth rates was carried out taking into consideration only the first 168 hour time period.

The regeneration period was then segregated into 25 hour bins for clear demonstration of trends. For each 25 hour bin, the % growth of the crystals was calculated using Equation 4.2:

$$\%Growth = \frac{\Delta L}{L_i} \tag{4.2}$$

Where ΔL is the change in the characteristic dimension in the 25 hour period, and L_i is the initial length of the characteristic dimension at the beginning of a particular 25 hour period. Figures 4.7 (e) and (f) show the % growth of the cleaved and a whole crystals over the regeneration period of 100 hours. It can be seen that in the first 25 hours length a of the cleaved crystal grew by an extra 80% compared to its length b as well as length

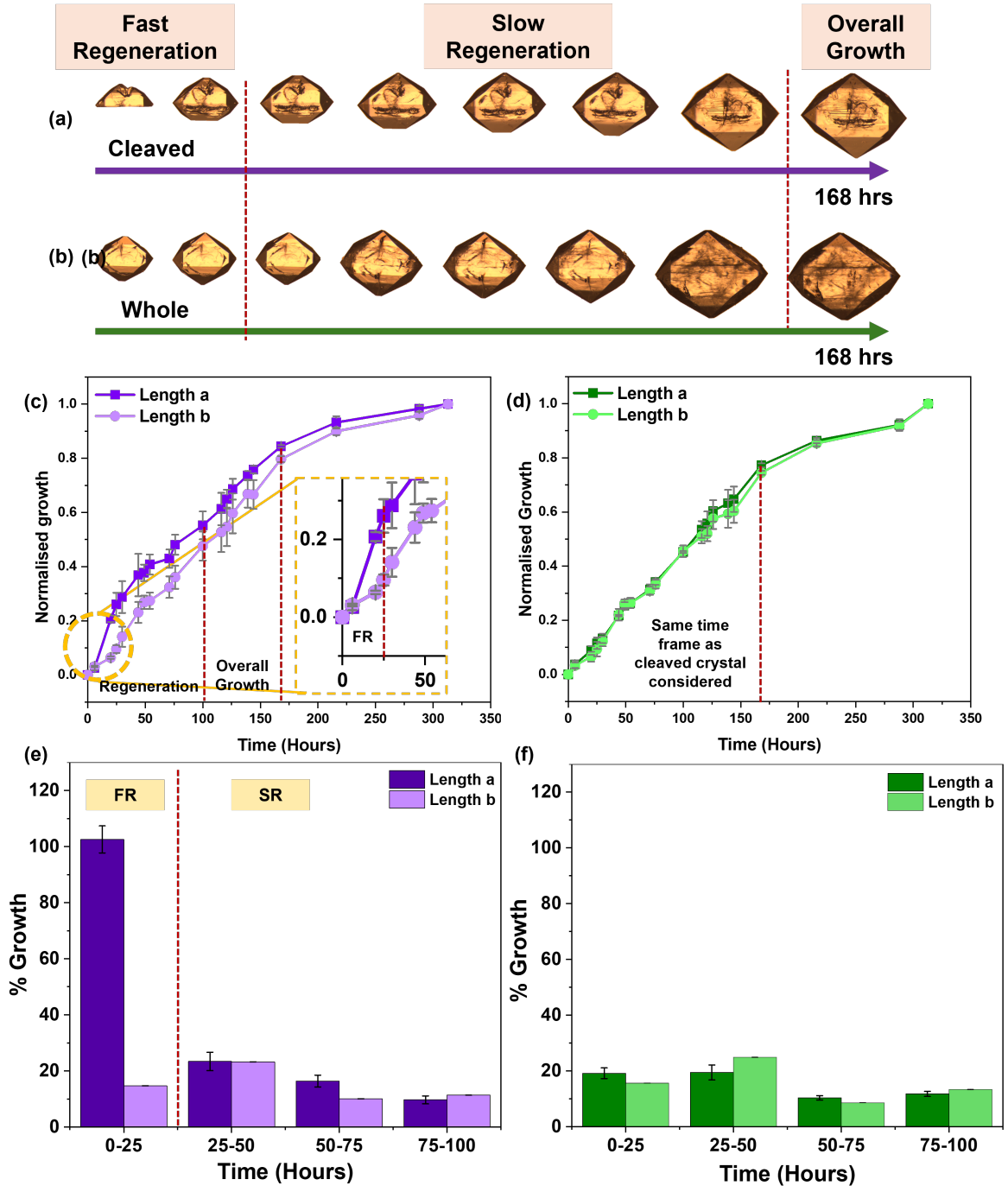


Figure 4.7: Snapshots of (a) a cleaved crystal regenerating post breakage and (b) the growth trajectory of a whole crystal. Averaged over at least 3 samples, the normalised growth behaviour of (c) cleaved crystals compared to (d) whole crystals during the entire 300 hours of the experiment. (FR and SR stand for 'Fast Regeneration' and 'Slow Regeneration' respectively)

a of the whole crystal. This emphasises two things: one, the propagation of facet (010) dominates during the regeneration process, and two, there exists an initial phase in the regeneration process, where the majority of the crystal regeneration is completed. It was postulated that as regeneration progresses, new facets like the (011) and (110) develop on the crystal, increasing the number of growing facets competing for solute molecules, which in turn slows down the regeneration process. Therefore the remainder of the regeneration takes place over a period of the subsequent 75 hours where growth in both directions resonated with that of an unbroken whole crystal.

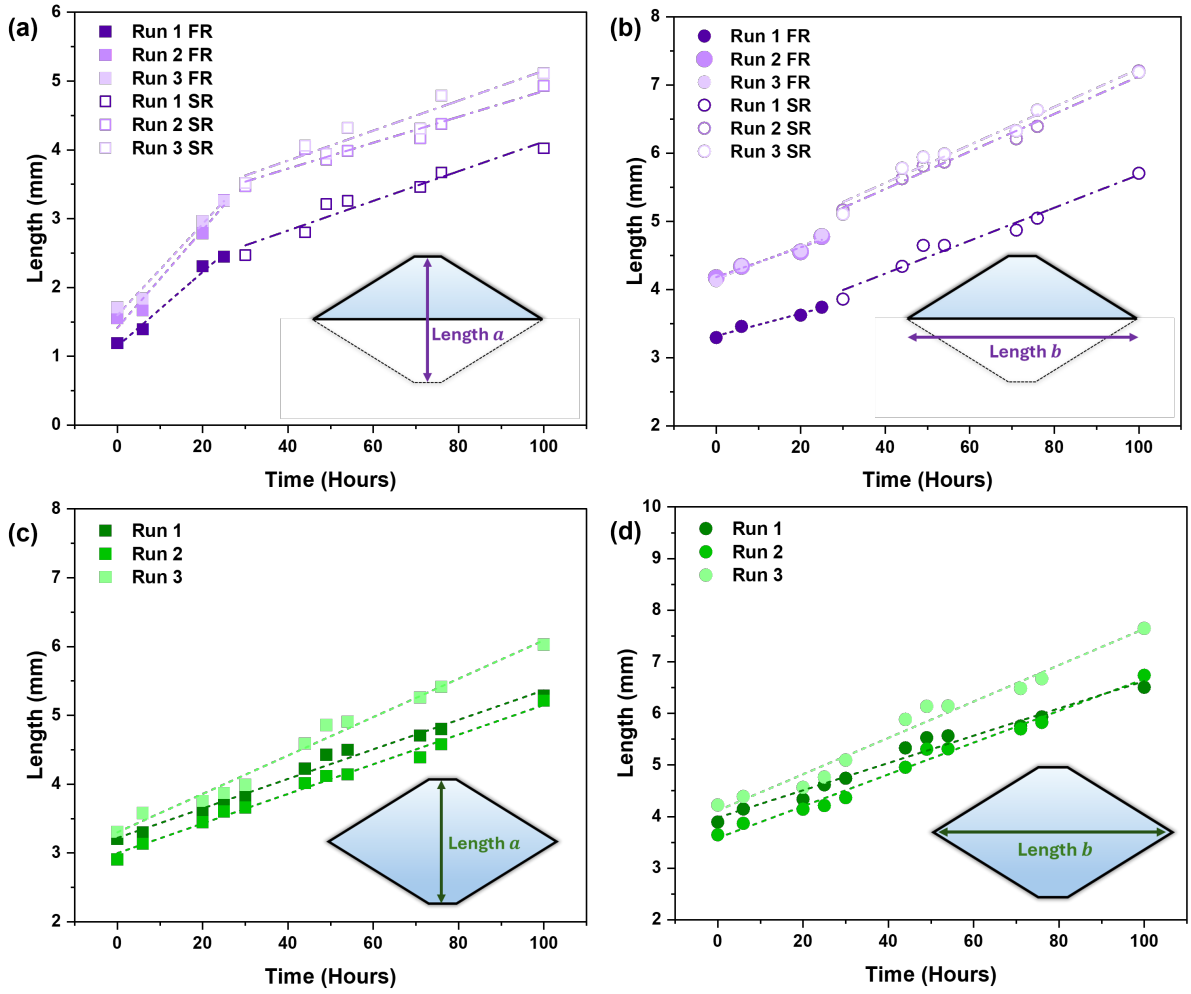


Figure 4.8: Propagation of characteristic dimensions a and b over time for 3 cleaved and 3 whole crystals: (a) Length a of cleaved crystal, (b) Length b of cleaved crystal, (c) Length a of whole crystal, and (d) Length b of whole crystal

Using the measured lengths, the growth rates during the regeneration period were determined as seen in Figure 4.8 using Equation 2.26, ΔL being the change in characteristic dimension. In Figure 4.8 (a), length a shows a clear change in gradient between 0-25

Table 4.3: Average growth rates of length a and b of cleaved crystals during fast regeneration, slow regeneration, and overall growth

Cleaved Crystal Growth Rates (mm/hr)										
Phase	**Length a**					**Length b**				
	Run 1	**Run 2**	**Run 3**	**Average**	**SD**	**Run 1**	**Run 2**	**Run 3**	**Average**	**SD**
Fast Regen	0.054	0.071	0.066	0.064	0.009	0.016	0.022	0.024	0.021	0.004
Slow Regen	0.022	0.019	0.022	0.021	0.002	0.024	0.028	0.028	0.027	0.002
Overall	0.028	0.020	0.027	0.025	0.004	0.030	0.023	0.032	0.028	0.005

Table 4.4: Average growth rates of length a and b of whole crystals during regeneration and overall growth of cleaved crystals

Whole Crystal Growth Rates (mm/hr)										
Phase	**Length a**					**Length b**				
	Run 1	**Run 2**	**Run 3**	**Average**	**SD**	**Run 1**	**Run 2**	**Run 3**	**Average**	**SD**
Regen	0.021	0.022	0.028	0.024	0.004	0.026	0.031	0.035	0.029	0.006
Overall	0.022	0.024	0.028	0.025	0.003	0.025	0.026	0.035	0.029	0.006

hours and 25-100 hours suggesting a growth rate 3 times faster in the initial stage on regeneration compared to the later stage. This interestingly also translates to a slightly slower growth rate of length b in the first 25 hours compared to the later 75 hours (Figure 4.8 (b)). When compared to the growth rates of whole crystals (Figure 4.8 (c) and (d)), it is evident that there is no change in the growth rates during the 100 hours irrespective of the characteristic dimension; length a and b advance uniformly at a constant rate of $\sim$ 0.026 mm/hr. Growth rates in all the stages are summarised in tables 4.3 and 4.4. Once regeneration is completed, the now regenerated crystals grow at the same rate as whole crystals in both directions. The growth rates of large crystals follow a similar trend and can be found in the Appendix A.1, however more experiments need to be carried out to deduce meaningful conclusions on the effect of crystal size on regeneration.

These results contradict the traditional morphological prediction theories (Section 2.3) that suggest slow growing facets dominate the crystal growth process and therefore the habit. This holds true for the growth of crystals from nuclei where fast growing facets instantaneously outgrow the slow growing facets and therefore have no morphological importance. Thus, the resulting growth of the seed crystals is dominated by slow growing facets. However, this does not apply to broken crystals where breakage exposes previously

non present facets. It is clearly seen that in the initial period of crystal growth post breakage, the fast growing facet dominates the crystal growth behaviour in a significant manner. It not only affects the growth rate of crystals but also the shape evolution.

4.4 Discussion

4.4.1 The proposed regeneration mechanism

Following on from the above results, a mechanism for post breakage growth has been proposed which can be categorised into three distinct regions: rapid regeneration, slow regeneration, and overall growth. This behaviour was unique to broken crystals because even though all experiments were carried out using the same mother liquor and under the same operating conditions, the whole crystals did not show these three regions (Figure 4.9).

As these experiments were carried out at ambient conditions in a fumehood, the rate of evaporation was not actively and rigorously controlled. However it was certain that the supersaturation was never too high because spontaneous nucleation was not observed. Moreover, since very slow yet continuous evaporation under stable room temperature and pressure was carried out over a period of multiple days, drastic changes in the concentration of the mother liquor were regarded unlikely. This was postulated to be due to a continuous creation and depletion of the supersaturation during the growth of crystals, resulting in a self-regulating constant concentration over the 150 hours. This can be be further consolidated by considering the growth of the unbroken crystals under the same conditions where growth rates for entire duration of the experiment have been constant. Hence the three distinct growth regions were associated with changes in the intrinsic growth behaviour of the crystal rather than due to variation in solution concentration.

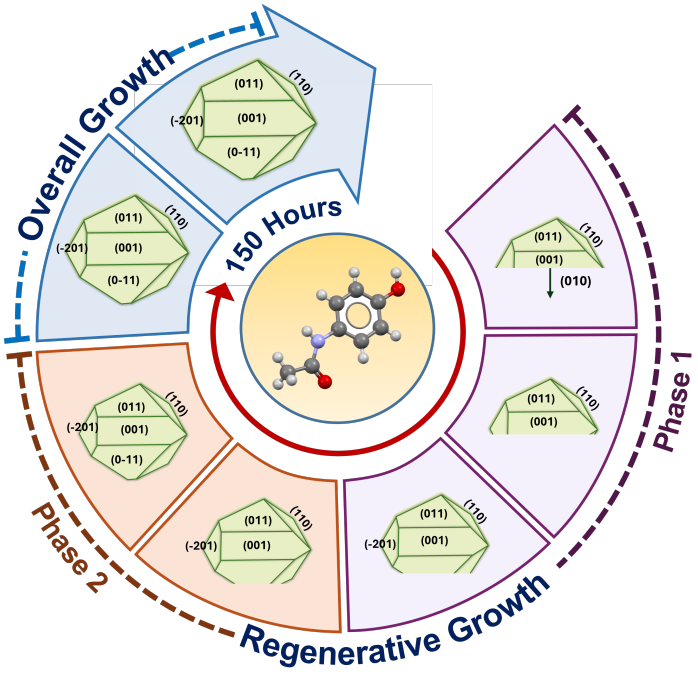


Figure 4.9: The proposed regeneration mechanism consisting of 2 phases; fast regeneration, and slow regeneration, followed by the overall growth of the crystal post shape restoration

4.4.2 Effect of regeneration on crystal shape and form

From Figure 4.10, it can be seen that predicted PXRD patterns of form I and form II of paracetamol are significantly different. As expected, the as-received paracetamol powder and the seeds grown from ethanol align with the form I PXRD pattern. Moreover, the regenerated crystals retained the monoclinic form of paracetamol with no observable differences in the peak positions of the unbroken and regenerated paracetamol crystals. The peak intensities observed for the seeds and regenerated crystals showed slight differences compared to the predicted pattern and the as-received paracetamol powder. This variation was attributed to sample preparation rather than any intrinsic alteration in the crystal properties. Since the seeds and regenerated crystals were macroscopic and required grinding before placement on the sample holder, inconsistencies in particle size could have resulted in variations in peak intensities.

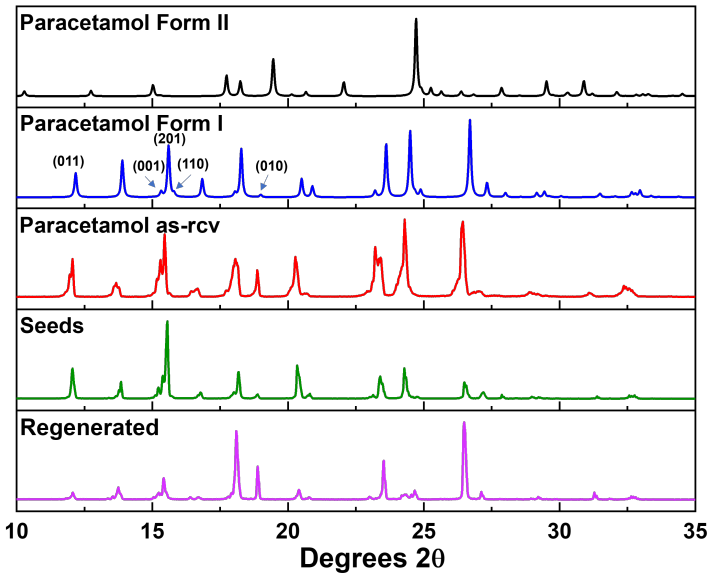


Figure 4.10: PXRD spectra of paracetamol crystals top to bottom, form II predicted using Mercury, form I predicted using Mercury, as received paracetamol powder, paracetamol seeds grown in ethanol solution, paracetamol crystals regenerated in ethanol solution

SEM was performed on the (010) facet of the crystal at various time points during the regeneration process; 0 hours (Figure 4.11 (a)), 25 hours (Figure 4.11 (b)), and 50 hours (Figure 4.11 (c)). The main aim was to track the advancement of the (010) facet which was not captured via the previously mentioned imaging techniques. It can be seen that at 0 hours, before the cleaved crystal was placed in solution, the (010) facet is relatively smooth, consolidating the claimed 'clean cut' from cleavage. The cracks that can be seen were generated from the point of pressure application and would be expected as a result of mechanical breakage. After 25 hours, (010) can be seen rugged as a result of growth on the facet. In comparison to the newly developed and smooth (011) facets, the (010) has more visible steps and ledges potentially due the multifold faster growth during rapid regeneration. Finally at 50 hours, a very thin remainder of the growing (010) facet can be seen along with the almost entirely developed (011) facets. Although the exact step heights and velocities cannot be deduced using SEM and will require more powerful techniques such as Atomic Force Microscopy (AFM), the rugosity itself is an indication of the rapid advancement of the (010) facet. These SEM micrographs support the proposed shape evolution of cleaved crystals during regeneration and confirm the restoration of their original, unbroken shape.

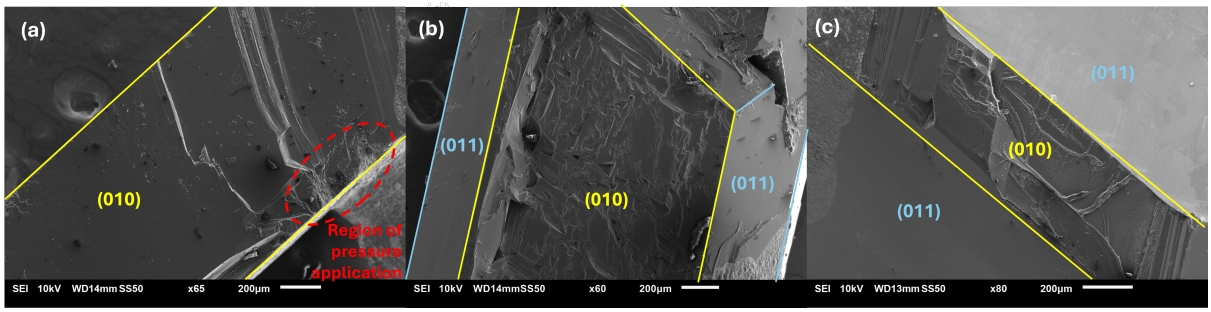


Figure 4.11: SEM images of (010) facet at different time intervals during regeneration (a) at 0 hours, (b) 25 hours and (e) 50 hours after cleaving.

4.4.3 Effect of regeneration on the fracture properties of crystals

The basis of regeneration is the existence of a brittle cleavage plane in paracetamol crystals which grows rapidly once exposed to achieve shape restoration. Preliminary studies have shown 'recyclability' of regenerated crystals such that a once regenerated crystal has the potential to be cleaved and regenerate again (Section 7.2.1). Hence it becomes crucial to understand, how regeneration affects the cleaving ability or the fracture properties of the crystal. Therefore nanoindentation was predominantly carried out on the two main facets associated with cleavage: (001), and (010). The load-displacement curves provide valuable qualitative information about the deformation behaviour of the facet being indented; in this case the effect of penetrating a Berkovich indentor at 90 °to the facet of interest. In general all curves, regardless of pristine or regenerated crystals, resulted in 'pop-ins' on the loading curve. As seen from the displacement curves of facets (001) and (010) of pristine crystals (Figure 4.12), the sudden increase in the penetration depth during the tip movement into the facet is a result of local dislocations, and a common observation in brittle organic crystals [241, 242]. Paracetamol crystals have been found to be brittle in nature [199] however due to anisotropy, differences in the deformation behaviour are observed. Very clearly, there are fewer and shallower pop-ins on the (001) facet as opposed to the (010) facet, potentially because indentation along the cleavage direction, [010] is this case, leads to a smoother curve [199]. Indentation normal to the (001) facet could also mean fracture along the [100] direction, but as reported

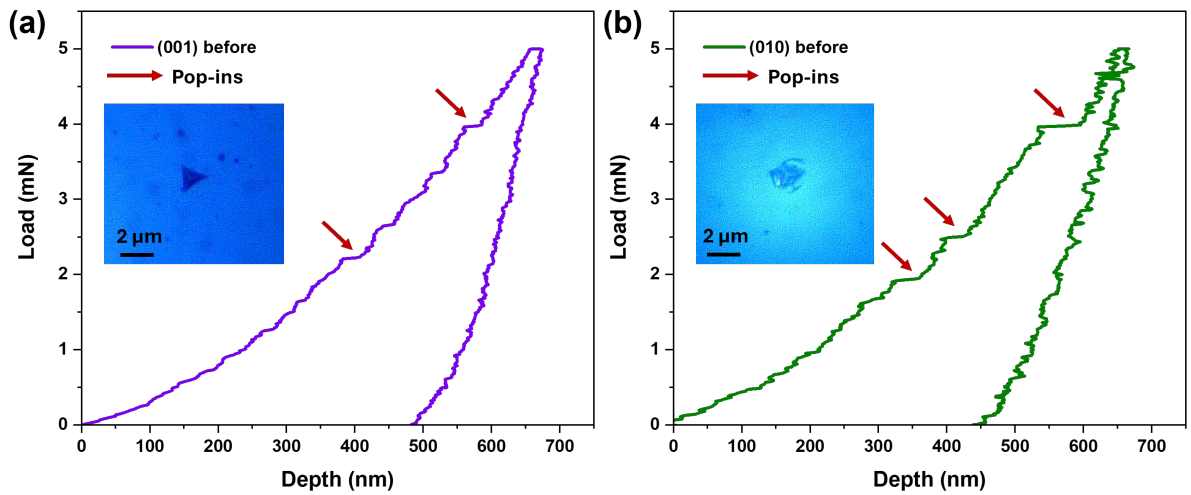


Figure 4.12: Example of the load-displacement curves obtained for the paracetamol facets,(a) (001) and (b) (010), before regeneration. The curves highlight the 'pop-in' behaviour commonly observed in molecular crystals along with micrographs of the indent

by previous indentation studies, and established in Section 4.3.1, [010] is the most likely cleavage direction and therefore responsible for the smooth curve. Since [001] and [100] are not the likely slip or cleavage directions, indentation on the (010) facet lead to more prominent dislocations as reflected by the pop-ins. This was further consolidated by the shape of the indentation. Whilst the (001) facet resulted in a clean triangular indent, the (010) led to 'pile ups' and micro cracks along the edges as seen from the micrographs in Figure 4.12.

Using the displacement curves, the hardness of facets (001) and (010) before and after regeneration was calculated using Equation 3.5, results of which are displayed in Figure 4.13(a). Some initial tests were also done on facets (201) and (011) and the results can be found in Section A.2 of the appendix. The hardness values are in similar orders of magnitude for paracetamol crystals as reported in the literature [238], with (001) being the easiest to indent and (010) being the hardest [239]. Although the standard deviation is significant, it is not uncommon due to crystal to crystal variability [242]. Even so, the data suggests a general increase in the hardness after regeneration, with the least increase ($\sim 2\%$) in the (001) facet followed by $\sim 6\%$ increase in the (201) and (011) facets and the largest increase of $\sim 10\%$ in the (010) facet. This increase in hardness was postulated to be due to the accumulated strain inside the crystal post regeneration. As seen from Figure

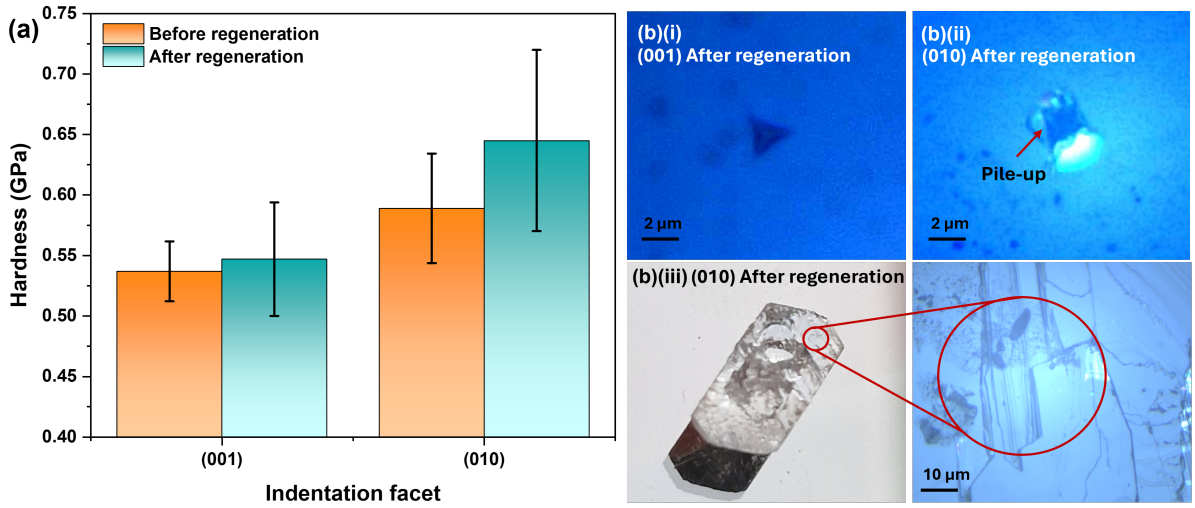


Figure 4.13: (a) Bar chart depicting the hardness of facets before and after regeneration where the error bars correspond to the standard deviation across 3 samples with 9 indents each. (b) images of the indents after regeneration on facet (i) (001) and (ii) (010) along with (b)(iii) the image of facet (010) exposed from a regenerated crystal

4.5(a), the regenerated part of the crystal is opaque compared to the non-regenerating side, corresponding to the accumulated tension due to rapid growth of the cleavage plane. As a result, when load is introduced normal to the facet, it dissipates via these lattice defects and therefore more work in required for the same level of indentation. Examining the (010) facet after regeneration (Figure 4.13(b)(iii)), it appears significantly rougher compared to its state before regeneration (Figure 4.11 (a)). This increased roughness is evident in the indentation, which lacks a distinct triangular shape and instead exhibits more pronounced pile-ups (Figure 4.13(b)(ii)), as opposed to the (001) after regeneration which still produces a neat indent.

The hardness conveys the resistance of the facet to indent under a certain load, and it can be deduced that even after regeneration (001) was the easiest to indent, whilst (010) was the hardest to indent. The reduced modulus of the (001) and (010) facets was calculated using Equation 3.8.4, displayed in Table 4.5, and even though there was a 20% decrease in the elasticity along the [001]/[100] direction after regeneration, the [010] direction still remains more susceptible to fracture after regeneration. Detailed analysis using the crack propagation along edges of the indents is required to elucidate the mechanisms of the fracture propagation for these facets. However, this lies outside the scope of this study as

Table 4.5: Reduced modulus, E_r, of facets (001) and (010) before and after regeneration

Indentation plane (hkl)	**Fracture plane** (hkl)	θ $^\circ$	**Before regeneration** E_r, GPa	**After regeneration** E_r, GPa
(001)	(010)	90	13.13 ± 1.18	13.14 ± 1.66
(010)	(001)/(100)	90	9.03 ± 0.98	10.88 ± 0.79

the main aim is to understand how regeneration affects the overall mechanical properties of a single paracetamol crystal.

4.4.4 Effect of regeneration on crystal quality

As seen in the above sections, even though the crystals retain their form, shape, and mechanical properties after regeneration, they seem to no longer remain 'pristine' in condition. Going by the definition of 'high quality' crystals stated in Section 3.3.1, the regenerated crystals only satisfy one of the two conditions. Although all the major facets are distinctly visible on the regenerated crystals, the majority of them also develop stress and defects internally - seen very clearly in the presented images. This is predominantly due to the mechanical damage induced during breakage, that then culminates into voids and irregularities in the crystal lattice during rapid regeneration. Even though this does not affect the overall fracture propensity of the crystal as seen in Section 4.4.3, the dislocations on the (010) plane exposed after regeneration (Figure 4.13(b)(iii)) are apparent. These dislocations could potentially host various impurities, including solvents, dust particles, or additives introduced to enhance crystallisation in an industrial context. Studies have shown that solvent occlusions can span up to 500 μm in radius in the presence of defects [242], whilst some studies have traced high impurity incorporation in crystals that are grown post fracture, via imaging [243] and via X-ray tomography [182]. These impurity incorporations can further alter the physical and chemical properties of the crystals such as their melting points, dissolution rates, purity, etc., making it a crucial topic to investigate in the future.

On the whole, peculiar observations arise from the regeneration phenomenon; firstly,

the rapid growth of facet (010) even though it is a weakly interacting plane. This was postulated to be due to the crystal trying to minimise it's overall surface free energy. Since facet (010) has little to no morphological importance on the equilibrium crystal habit, the cleaved crystal becomes extremely unstable once in solution, thus prompting rapid advancement of (010) to attain a thermodynamically stable configuration. Moreover, this effect could be amplified due to the 0 hydrogen bonding potential of the (010) facet. As the surface is extremely apolar, it is unlikely for the surface to have any affinity to the ethanol molecules which is a polar protic solvent. Hence, no substantial energy would be required to desorb the solvent molecules from the crystal surface before the solute molecules can adsorb. This goes against the traditional morphological prediction theories that suggest that slow growing facets dominate the crystal habit. Although this holds for unbroken crystals, it is not necessarily true for broken crystals. It is proposed that regeneration can occur in crystals that have a prominent cleavage plane that is also an inherently fast growing plane. Preliminary work has been carried out on carbamazepine (CBZ), glycine, and aspirin where CBZ and glycine have shown signs of regeneration when broken along their fast growing cleavage plane. Asprin on the other hand has a cleavage plane with high morphological importance and therefore does not regenerate. The author refers the reader to Section 7.2.4 of the conclusion chapter for preliminary results.

In this chapter, evaporative crystallisation was employed as the primary method for crystal growth. While this approach proved robust for observing and interpreting the regeneration phenomenon under ambient crystallisation conditions, it has limitations in analysing qualitative and quantitative behaviours across a broader range of conditions. Consequently, new methodologies and analysis were developed to investigate the effects of solvents, supersaturation ratio, and agitation on regeneration rates and behaviour, as detailed in chapters 5 and 6.

4.5 Conclusion

A clear distinction has been made in terms of nomenclature for slip planes and cleavage planes, and facet (010) has been identified as the preferred cleavage plane of form I paracetamol crystals based on the crystal structure. A previously unreported 'regeneration' phenomenon was observed in paracetamol crystals following breakage along the cleavage plane. Here the broken crystal grew back to its pre-breakage shape prior to demonstrating overall growth via rapid advancement of (010), which has previously not been reported. It was demonstrated via slow solvent evaporation, that regeneration is dependent on the breakage orientation, regardless of initial crystal size. Cuts parallel to the cleavage plane, irrespective of the extent of breakage, resulted in regeneration whilst cuts perpendicular to the cleavage plane did not. Following growth rate measurements of cleaved crystals, a 3-step post-breakage growth mechanism has been proposed; rapid regeneration, followed by slow regeneration, and eventually overall growth. Overall, the regeneration phenomenon not only restores the crystal shape and the mechanical properties but also preserves the crystal form. This chapter emphasises that after breakage, fast-growing facets dominate crystal growth, making it essential to account for specific post-breakage kinetics to accurately predict crystal shape and size.

Chapter 5

Design of isothermal crystallisation set-up with integrated macrophotography to investigate solvent effects on crystal regeneration

5.1 Overview

Solvents play an important role in crystallisation where they can strongly influence the crystal growth process and therefore the resulting crystal properties. This chapter investigates the effect of three solvents; ethanol, tetrahydrofuran, and acetone, on the novel regeneration phenomenon observed in paracetamol crystals. An isothermal crystallisation rig, compatible with macrophotography was developed to perform single crystal regeneration experiments in a controlled environment. Moreover, an image analysis protocol was designed on MATLAB for precise edge detection and facet specific crystal growth rate measurements.

Regeneration was successfully observed in all three solvents at a constant supersaturation of 1.10, despite differences in crystal habit. The rapid growth of the (010) face dominated the regeneration process, restoring each crystal to its pre-breakage shape. Regeneration rates differed across solvents, with the fastest observed in ethanol (0.07 mm/hr), followed by THF (0.03 mm/hr), and the slowest in acetone (0.02 mm/hr). Interestingly, it was also established that along with the rate of regeneration, the original crystal shape also plays a crucial role in the time taken for the completion of regeneration. Consistent with Chapter 4, two stages of regeneration were noted, with the rapid initial phase accounting for 8–15% of the total regeneration time across solvents. However, after regeneration, growth rate trends shifted, with ethanol exhibiting the fastest growth, followed by acetone and then THF.

Discussions revolving around crystal shape, surface chemistry, solvent interactions, as well as paracetamol solubility in the three solvents have been used to decipher the observations. These discussions have been aided with characterisation techniques such as XPS, as well as molecular dynamic simulations to quantify the binding energy of the crystal and the solvent, providing deeper insight into the regeneration behaviour.

5.2 Methods

5.2.1 Solubility of paracetamol in different solvents

Paracetamol was used as the pharmaceutical compound of choice along with three solvents; ethanol, acetone and THF. The details of these chemicals can be found in Section 3.1. The solubility of paracetamol in ethanol was determined using the method detailed in Section 3.2. Solubility was measured at 20 °C, 25 °C, 30 °C, 40 °C, and 50 °C. The procedure was repeated three times for each temperature and the final solubility at the corresponding temperature was found by calculating an average of the three repeats. The final solubility curve; concentration against temperature, was found by fitting the data

points as an exponential function of temperature with an R^2 value closest to 1. Solubility of paracetamol in acetone and THF was obtained by a colleague in the Heng group, Deniz Etit, using the same procedure and hence their data was utilised.

5.2.2 Isothermal crystallisation without agitation

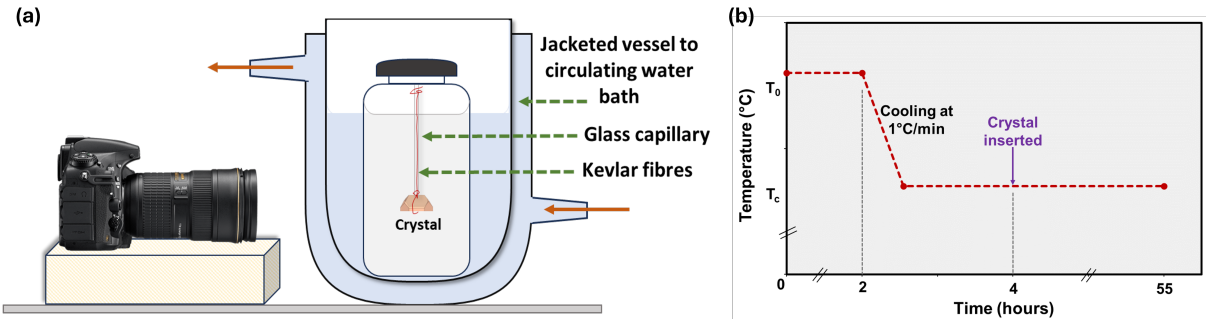


Figure 5.1: (a) isothermal crystallisation set-up using a jacketed vessel connected to a circulating waterbath and imaging done via a DSLR camera at fixed time intervals (b) Temperature profile for isothermal crystallisation where T_0 is the initial temperature at which solution is equilibrated and T_c is the temperature required to reach $S = 1.10$

Paracetamol seeds and macroscopic crystals were obtained from all three solvents in the exact manner as detailed in Section 3.3. Consequently they were cleaved using a scalpel to expose the cleavage plane (010) prior to being used in regeneration experiments. The methodology for cleaving the crystals can be found in Section 3.4 of this thesis. To investigate the effect of solvents at a constant supersaturation an isothermal crystallisation set-up was developed (Figure 5.1). A 100 ml jacketed vessel was connected to a circulating waterbath. Paracetamol crystals of size of 4-5 mm were cleaved and suspended in a 60 ml glass bottle, ensuring the freshly cleaved facet faced the bottle's base. This setup was achieved by tying the crystal to a few strands of Kevlar fibre, threading these fibres through a glass capillary, and securing the fibres to the capillary using Blu Tak ®. The capillary was passed through a hole in the bottle lid and secured in place, again using Blue Tak ®. This immobilised the crystal in the solution for better imaging, as seen in Figure 5.1. A solution saturated at 30 °C (T_0) was added to the glass jar before suspending the crystal, which was then placed in the jacketed vessel set at 30 °C for 2 hours. The solution was subsequently cooled to a temperature resulting in a supersaturation of

1.10 (T_c) and maintained for another hour, after which the crystal was inserted into the solution.

The jacketed vessel was placed inside a photography light box and using the same Nikon D90 DSLR camera rig detailed in Section 4.2.3, the regeneration of the crystals was monitored. Images were captured every 15 mins for a duration of 55 hours following which they were analysed using MATLAB (section 3.7.1) to obtain growth data. It is important to note that concentration of the solution was measured before the crystal was inserted as well as at the end of the 55 hours. In each case the change is concentration was $\leq 5\%$ and therefore considered constant throughout the experiment.

5.3 Results

5.3.1 Experimental habits and PXRD patterns of paracetamol crystals from different solvents

Experimental habits of paracetamol crystals obtained from ethanol, acetone and THF solutions can be seen in Figure 5.2(a-c). PXRD confirmed the crystals to be of the monoclinic form I paracetamol (Figure 5.3(b)). However, the habits are seen to be relatively different. Although they are of the same polymorphic form and have the same major facets, in agreement with the attachment energy habit shown in Section 4.3.1, the proportion of facets occupied on the equilibrium habit varies, highlighting the significance of solvent effects on the crystal growth. For instance, even though facets (111) and (200) appear on the attachment energy habit, due to the fast growing nature of the facets, (111) does not appear on any experimental habits whilst (200) only appears on crystals grown in acetone. Overall, the experimental habits are in line with the 'prismatic' morphology reported in literature [142, 157].

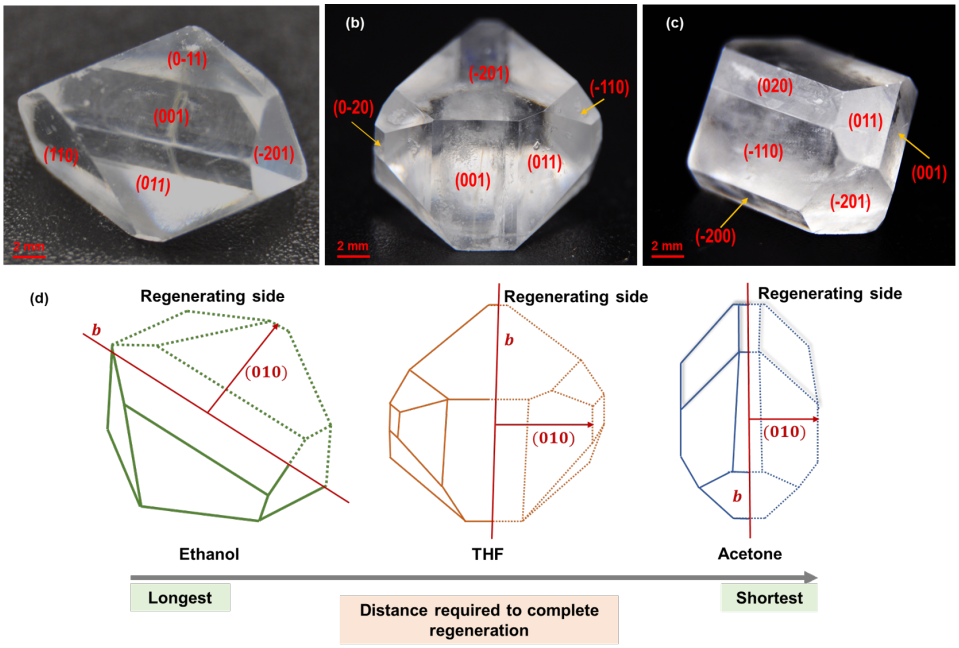


Figure 5.2: Experimental habits of paracetamol obtained via slow evaporation in (a) Ethanol, (b) THF, and (c) Acetone. The crystals in the image are approximately 1 cm large along their longest dimension (d) diagrams highlighting the characteristic dimension and (010) facet propagation on the observed experimental habits in the different solvents

5.3.2 Solubility of paracetamol in pure solvents

The solubility curves of paracetamol in ethanol, acetone and THF can be found in Figure 5.3(a) and show good agreement with literature [22]. Paracetamol shows highest solubility in ethanol, followed by THF, and the lowest in acetone. As the standard deviation (SD) of the solubility data is less than 2% and cannot be seen clearly on the plot, the corresponding SD values can be found in Table 5.1, along with the equations of the respective solubility curves. Using the measured solubility at 30 °C, the concentration resulting in a supersaturation of 1.10 was calculated via Equation 2.6, for each solvent system. Consequently the temperatures corresponding to a supersaturation of 1.10 for ethanol, acetone, and THF were found and can be seen in Table 5.2 below.

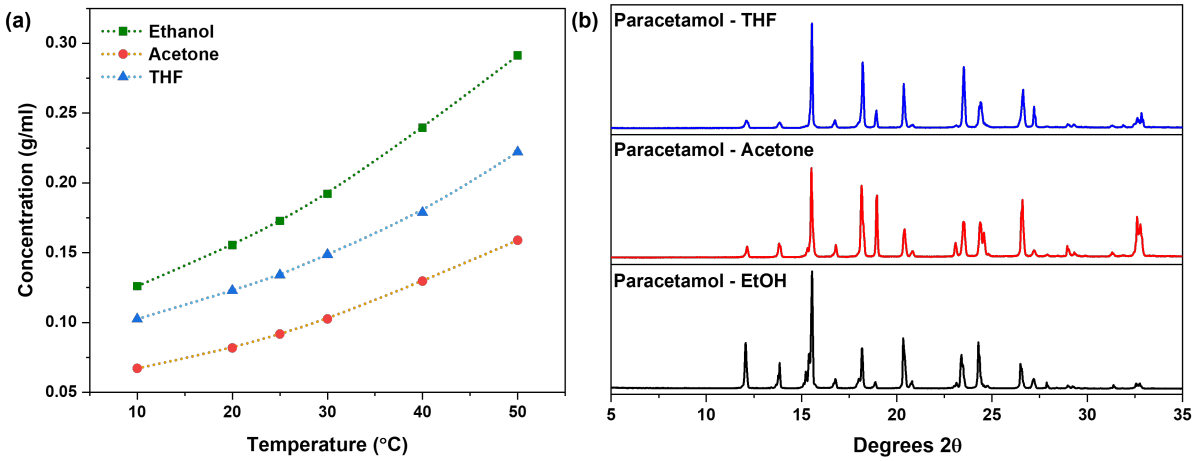


Figure 5.3: (a) Solubility curves of paracetamol in the three solvents and (b) the PXRD spectra of the crystals obtained from top to bottom: THF, acetone, and ethnaol

Table 5.1: Solubility of paracetamol in g/ml ± SD $\times 10^{-4}$ in three different solvents; ethanol, THF and acetone

Solvent	**Temperature (°C)**						**Equation**
	10	**20**	**25**	**30**	**40**	**50**	
Ethanol	0.128 ± 1.3	0.156 ± 1.1	0.172 ± 2.6	0.190 ± 3.4	0.232 ± 3.5	0.283 ± 3.3	$c = 0.1045 \times \exp^{0.0199 \times T}$
THF	0.102 ± 3.0	0.123 ± 8.5	0.134 ± 5.7	0.149 ± 5.3	0.179 ± 5.4	0.222 ± 12.8	$c = 0.0836 \times \exp^{0.0193 \times T}$
Acetone	0.067 ± 1.9	0.082 ± 1.9	0.092 ± 2.1	0.103 ± 1.5	0.130 ± 1.3	0.159 ± 7.0	$c = 0.0534 \times \exp^{0.0219 \times T}$

Table 5.2: Crystallisation conditions at S = 1.10 for the regeneration of paracetamol in ethanol, acetone, and THF

Solvent	**Crystallisation Temperature** T_c °C	**Concentration** c g/ml	**Equilibrium concentration** $c*$ g/ml	Δc g/ml
Ethanol	25.6	0.192	0.175	0.017
Acetone	25.9	0.103	0.093	0.011
THF	25.8	0.149	0.135	0.014

5.3.3 Effect of solvent on the rate of regeneration

Firstly, as seen from the snapshots in Figure 5.4, paracetamol crystals were observed to regenerate in all three solvents. The time taken for regeneration varied across the systems with the fastest regeneration taking place in acetone, followed by ethanol, and lastly THF, taking almost twice as long as in acetone. To further quantify the growth behaviour in the different crystallisation environments, the facet propagation of (010) was measured alongside the characteristic length b (section 3.7). Even though the dihedral angle between the (010) and (110) plane stays constant regardless of the crystal habit, the varying morphological significance of facets in different solvents leads to inconsistencies in which facets are imaged. So whilst keeping the focus on (010), (110) is only visible in ethanol but not in acetone and THF. Therefore to keep the comparison uniform, growth rate of (010) and length b, i.e., non-regenerating crystal dimension, for the different habits were calculated.



Figure 5.4: (a) Regeneration snapshots of paracetamol in top to bottom: ethanol, THF and acetone

Figure 5.5 depicts representative plots for each solvent system, illustrating the progression of length (mm) over time (hours) as obtained via MATLAB image analysis. Figure 5.5(a) highlights the facet propagation of (010) over the entire duration of the experiment. Using this plot and more importantly with visual verification from images, the

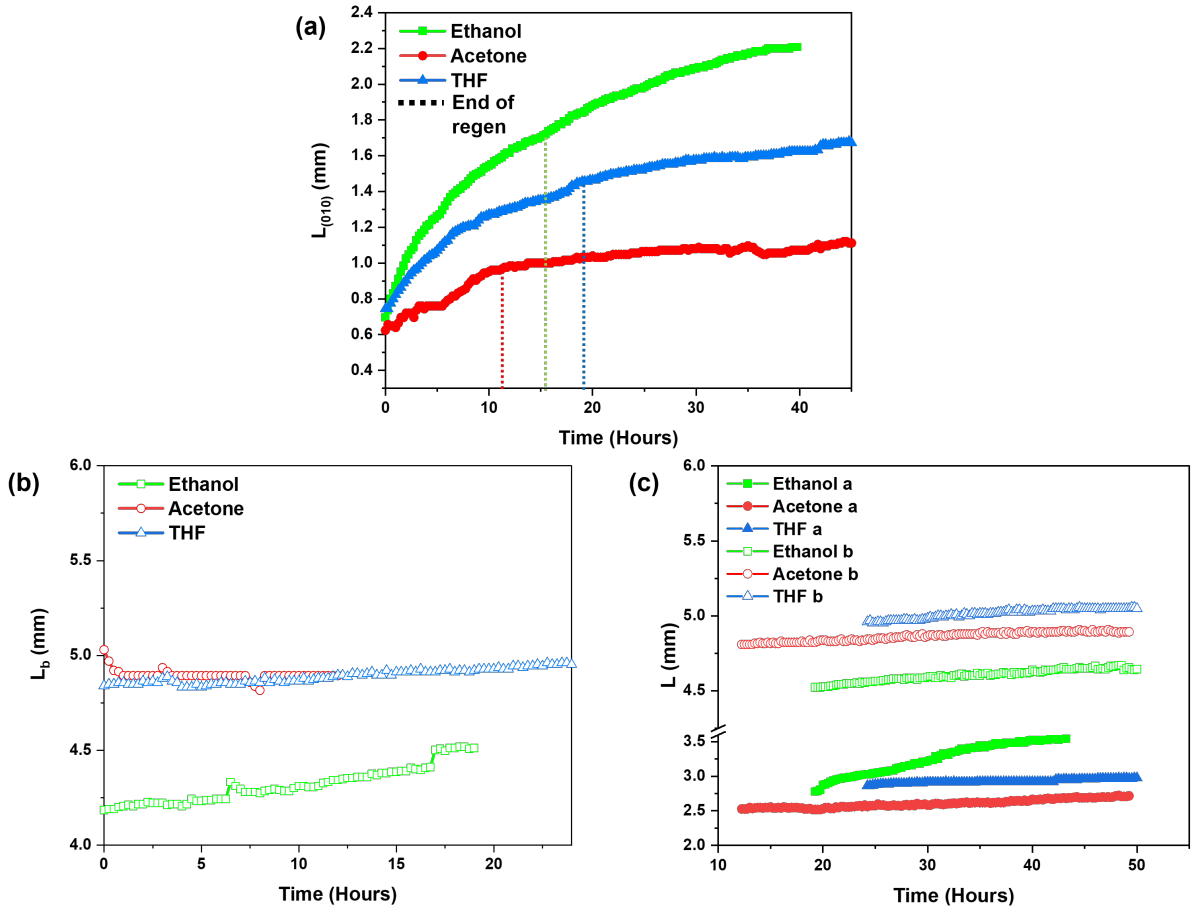


Figure 5.5: Example plots of crystal growth in each solvent obtained via MATLAB. Each line represents 1 individual crystal: (a) facet propagation of (010) for the entire duration of the experiment. Using this plot, the duration of the fast regeneration and the total regeneration period was deduced. Change in characteristic dimension b (b) during regeneration and (c) after regeneration. The gradients of these plots were used to estimate the growth rates

end point of regeneration for every crystal was deduced. The point where the line shows a change in gradient as well as the images indicate full shape restoration was designated as the end point of regeneration (as seen from the long dashed lines in Figure 5.5(a)). After regeneration is completed, (010) is no longer present on the crystal, deeming facet propagation of (010) unreliable. Therefore, for the rest of the experimental duration, length a and b are measured to demonstrate the change in characteristic dimensions of the crystal post regeneration as depicted in Figure 5.5(c). The growth rate in mm/hr for (010), length b during regeneration (Figure 5.5(b)) as well as length a and b after regeneration was calculated by fitting a linear trendline to the growth data.

The regeneration rate varies between the solvents in the order: Ethanol > THF > Ace-

tone. Figure 5.6(a) highlights that regeneration in ethanol is almost 3 times and 4 times faster than in THF and acetone respectively. Moreover, just as observed in the case of evaporative crystallisation with ethanol in chapter 4, the facets on the unbroken side of the crystals, regardless of the habit, were relatively dormant during regeneration and maintained a trivial growth rate in the range of $0.006 \leq G_b \leq 0.017$ mm/hr. Post regeneration, once the pre breakage shape is restored, length a and length b grow at relatively equivalent growth rates as shown in Figure 5.6(b). Interestingly, after regeneration, the trend between acetone and THF reverses, with crystal growth in acetone becoming nearly three times faster than in THF, although ethanol still leads with the fastest growth rate. It is important to note that the elongated appearance of the error bars in Figure 5.6(b) is primarily due to the narrow range on the y-axis. Despite the standard deviation, there remains a relative difference in growth rates among the three solvents. Notably, in the case of THF, the slight negative value of the error bar of length b is an artifact resulting from the very slow growth rate (fairly dormant), which overlaps with the uncertainty introduced by the edge detection algorithm.

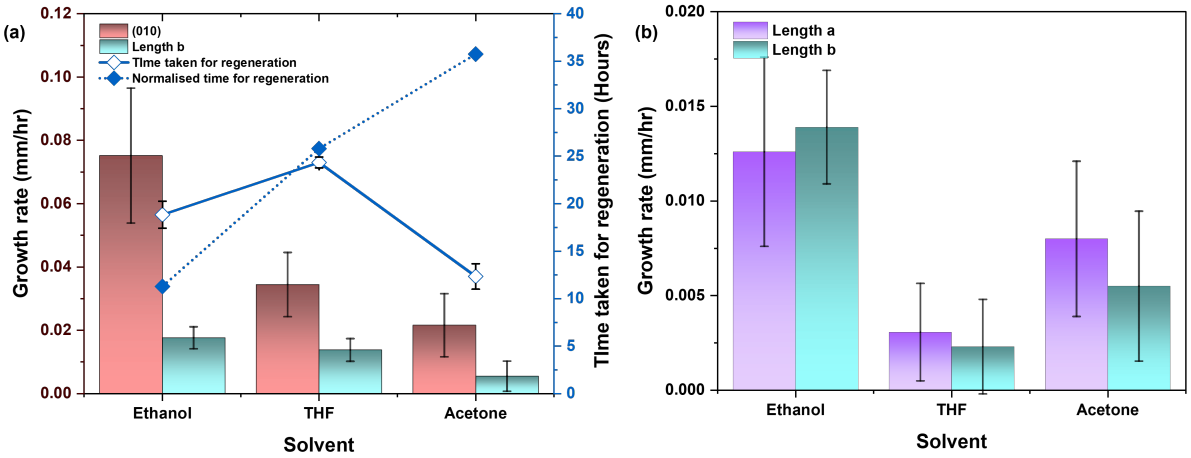


Figure 5.6: (a) Growth rates of (010) and length b during regeneration along with the absolute and normalised time taken for regeneration in each solvent. (b) Growth rates of length a and b after regeneration in all three solvents. Error bars in each case represent the standard deviation

Even though the rate of regeneration in acetone was the lowest in comparison to the other solvents, it resulted in the shortest regeneration period. This was postulated to be due to the distance required for (010) to grow in order to complete the regeneration.

This distance varied across the solvents because of the difference in crystal habits (Figure 5.2(d)). For instance, crystals grown in acetone have a very small (011) facet and a large (110) facet, opposite to that of ethanol grown crystals. Hence in acetone, (010) had to grow over a shorter length before the growth habit was achieved as opposed to in ethanol, where (010) had to keep growing until the large (011) facets were formed. Therefore, the time taken for regeneration was normalised over the distance of facet propagation required for regeneration to be completed. These normalised regeneration times can be seen as the blue dotted line in Figure 5.6(a) and as expected depict the opposite trend to that of the regeneration rates.

Table 5.3: Fast and slow regeneration rates of paracetamol in different solvents at S = 1.10

Solvent	**fast regeneration period** Hours	**% of Total regeneration period**	**Fast regeneration Rate** mm/hr	**Slow regeneration Rate** mm/hr
Ethanol	1.6	8.5%	0.16	0.07
THF	1.75	7.2%	0.12	0.04
Acetone	2	16%	0.07	0.02

The regeneration period of crystals was further analysed to elucidate if the mechanism proposed in chapter 4 applies in the case of different solvents. As seen from Figure 5.6(a), for each solvent there was indeed an initial segment on the (010) growth curve that has a steeper slope compared to the rest of the regeneration phase. The duration and growth rates of which have been tabulated in Table 5.3. It is interesting to note that regardless of the total regeneration period, the fast regeneration phase only lasted for around 2 hours for each solvent, corresponding to around 8.5%, 7%, and 16% of the total regeneration period in ethanol, THF, and acetone respectively. However, the growth rates in this initial phase varied depending on the solvent, following the same trend as the overall regeneration rate: the fastest in ethanol (0.16 mm/hr), followed by THF (0.12 mm/hr), and lastly acetone (0.07 mm/hr). These rates were at least twice as fast as the slower regeneration rates.

5.4 Discussion

The relative order of polarity between the solvents is as follows: Ethanol > Acetone > THF. It was hypothesised that, since the (010) facet is an apolar facet, the least polar solvent (THF) would have the highest affinity to the surface and hence result in a larger barrier to regeneration as more energy would be required to remove the solvent layer. However, this did not correlate with the case at hand. Based on the regeneration rates in the above sections, regeneration was the fastest in ethanol followed by THF and then acetone. To elucidate this discrepancy, the interaction energy between the solvent and (010) crystal surface was calculated using molecular dynamic simulations as described in Section 3.9.3. Because (010) is not a morphologically important facet of form I paracetamol, it has never been studied in detail, as opposed to some of the other major facets (001), (011), and (110), whose solvent interactions have already been reported [157, 205]. Prior to carrying out the simulations, the atomic composition as well as the functional group composition of each facet was analysed using XPS to get a better understanding of the facets at a molecular level. This XPS study goes in parallel with the molecular dynamic studies to reinforce that there is no fundamental discrepancy between the plane being modelled and the experimental facet.

As illustrated by the paracetamol structure ($C_8H_9NO_2$), carbon was found to be the most abundant element on each facet, followed by oxygen and then nitrogen (Table 5.4). However, the exact elemental composition varied between each facet which was postulated to be due to the molecular packing in each plane. It is important to note that the minimum penetration length of the X-rays is 10 nm and thus the 'surface' in this context in reality is 10 nm into the bulk of the crystal. As the miller indices are indicative of the crystallographic axis that the plane of the facets intercept, the orientation of packing in each individual facet will vary. Thus, the proportions of carbon, oxygen and nitrogen atoms coinciding with the X-rays will differ for unique facets.

From the atomic composition itself, it can be deduced that the (010) facet is relatively least polar with the highest carbon content and lowest oxygen and nitrogen content. To

Table 5.4: Elemental composition of different facets determined via XPS

Facet	Elemental composition		
	% C	*% N*	*% O*
(001)	82.7 ± 2.8	6.1 ± 0.7	11.2 ± 2.1
(010)	88.2 ± 0.9	4.4 ± 0.4	7.5 ± 0.5
(011)	83.9 ± 1.0	5.9 ± 0.4	9.9 ± 0.7
(110)	80.0 ± 1.5	6.4 ± 0.3	13.2 ± 1.5
(201)	82.2 ± 3.5	6.0 ± 1.8	11.7 ± 3.6

analyse further, the $C1_s$, $O1_s$, and $N1_s$ spectra were deconvoluted to obtain the functional group proportions for each element. A representative deconvoluted $C1_s$ spectra of facet (001) can be seen in Figure 5.7(a). The $C1_s$ spectra showed 3 peaks at 284.4 eV, 285.5 eV and 287.6 eV corresponding to the C-C, C-O+C-N and C=O functional groups respectively. From the $C1_s$ spectra in Figure 5.7(b), the ratio of peak intensities appears to vary between facets. Although there is some overlap in the error bars for the %C-C bonding environment (Figure 5.7(c)) — likely due to C-C being the most abundant functional group across all facets — a specific ratio of %C=O and %C-O, C-N to %C-C was calculated to better evaluate facet polarity. Despite this overlap, the (010) facet is clearly identified as the most apolar, with the least amount of the polar groups in proportion to the C-C environment, prompting it to be the most hydrophobic facet (Figure 5.7(c)), also in agreement with the literature [244]. When the aromatic contributions from each C spectra were compared with those obtained via surface analysis using Mercury (section 4.3.1), a good agreement in the trend between facets was observed. This can be seen as the red line on Figure 5.7(c).

Following the validation, interaction energy between the solvent and (010) surface was calculated and can be found in Table 5.5. The interaction energy of THF was almost 7% lower than of acetone which was similarly lower than of ethanol. This suggested stronger bonding between (010) and THF followed by acetone and then weakest with ethanol. Molecules at the surface behave differently to those in the bulk because they are not fully surrounded by neighbouring atoms. Thus the topmost layer of the crystal was unfixed during the simulations whilst keeping the lower layers fixed. This also leads to

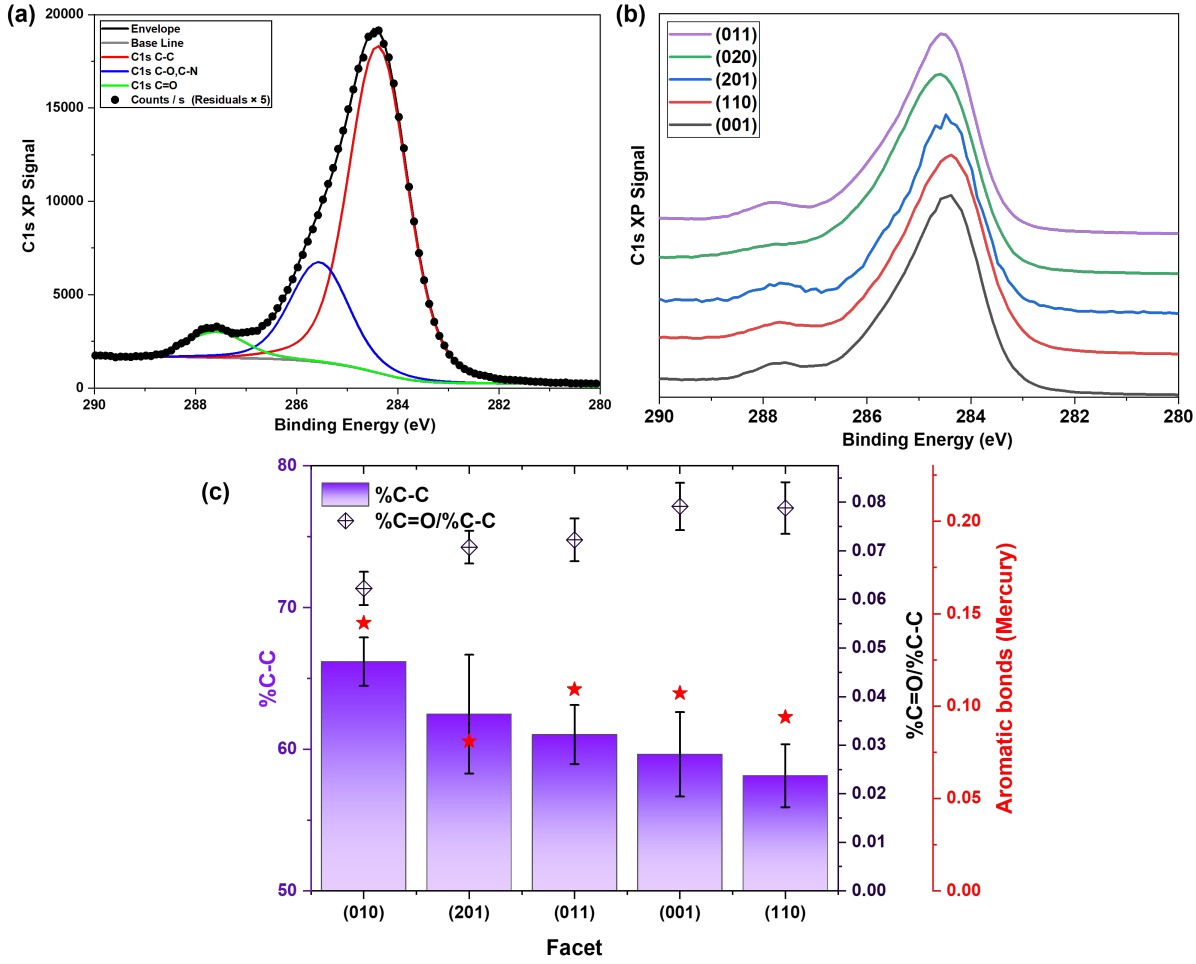


Figure 5.7: (a) An example plot of the deconvoluted carbon spectra of individual facets, (001) in this case (b) Overlayed carbon spectra of all major facets to highlight the differences in functional group composition (c) Summary plot of the amount of C-C bonding environment and ratio of C=O to C-C in each facet as well as a comparison with the aromatic bonds density obtained via Mercury in Table 4.2

surface relaxation where the top layer of atoms slightly adjusts its positions to minimize surface energy, therefore more accurately capturing the real physical behaviour of the crystal. Snapshots of the bilayer after the MD simulation were taken to analyse the bonding between the solvent molecules and the paracetamol molecules on the surface (Figure 5.8). Although (010) has no hydrogen bonding potential in the b direction, the unfixed solute layer has some degree of movement, thus, acetone and THF both formed hydrogen bonds with the surface molecules (Figure 5.8(b) and (c)) but ethanol did not (Figure 5.8(a)).

Table 5.5: Interaction energy between solvent and (010) crystal surface along with the solvent dielectric constant and molecular weight

Solvent	**Interaction Energy** kcal/mol	**Dipole moment**	**Molecular Weight** g/mol
Ethanol	-220.9	1.69	46.1
Acetone	-237.5	2.88	58.1
THF	-255.0	1.75	72.1

Although acetone and THF have higher dipole moments compared to ethanol, they are polar aprotic solvents, whereas ethanol is a polar protic solvent capable of independently forming hydrogen bonds. Since THF and acetone can only accept hydrogen bonds, it is postulated that the C-O-C group in THF and the C=O group in acetone preferentially bond with the hydroxyl (OH) groups of paracetamol molecules, rather than allowing hydrogen bonds to form between paracetamol molecules in the a and c directions. Conversely, in ethanol, it is energetically more favourable for the ethanol molecules to engage in hydrogen bonding with each other, interacting with paracetamol primarily through Van der Waals and Coulombic interactions. As confirmed by the radial distribution function (RDF) analysis in Figure 5.9, hydrogen bonding ($r \leq 3$ Å) is dominant in THF and acetone, followed by Van der Waals interactions ($3 \leq r \leq 5$ Å). In contrast, ethanol shows a dominance of Coulombic interactions ($r \geq 5$ Å). Although this is theoretically sound, does not align with the regeneration observation.

The role of solvents in crystal growth is highly complex and influenced by multiple interdependent factors, not just the hydrogen bonding affinity to the surface, though this is

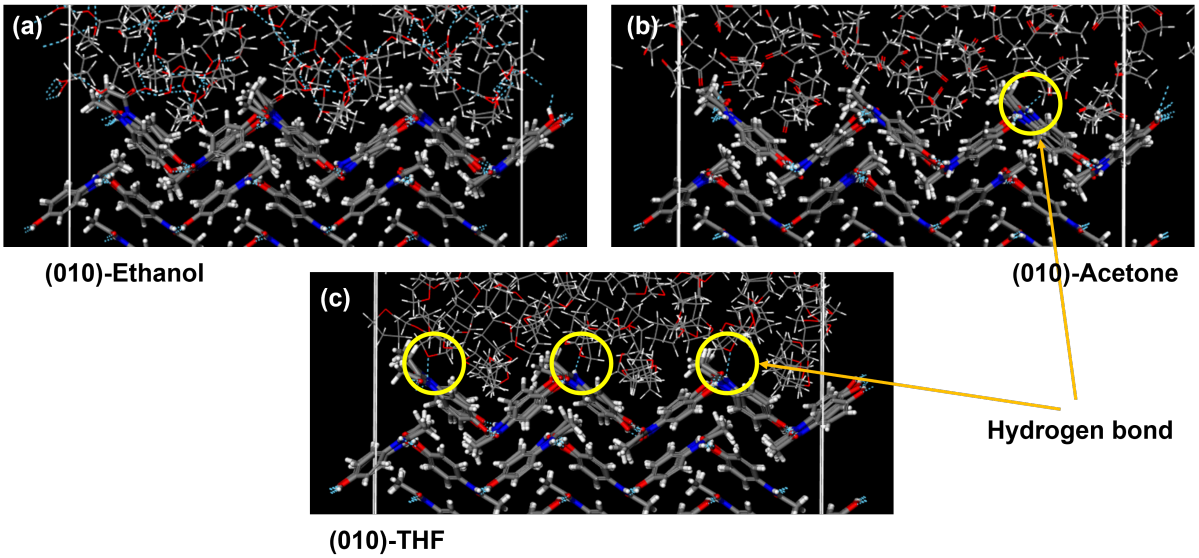


Figure 5.8: Snapshots of the bilayer at the end of the MD simulations depicting the bonding between the top layer of (010) surface with (a) ethanol, (b) acetone, (c) THF

often emphasised in the literature. Factors such as solubility, the rate of supersaturation generation, solvent pH, and evaporation number all contribute to the growth rate [157]. As shown in Table 5.2, the initial temperature across all solvent systems was consistent at 30°C, as was the crystallisation temperature, T_c. With a constant supersaturation ratio of 1.10, the ratio of c to $c*$ remained the same in each case. Additionally, the gradient of the solubility curves between 25°C and 30°C was similar for all three solvents, resulting in only a marginal difference in Δc. Consequently, the amount of excess solute at 1.10 supersaturation available for growth in a 60 ml volume was also approximately 1 gram, regardless of the solvent.

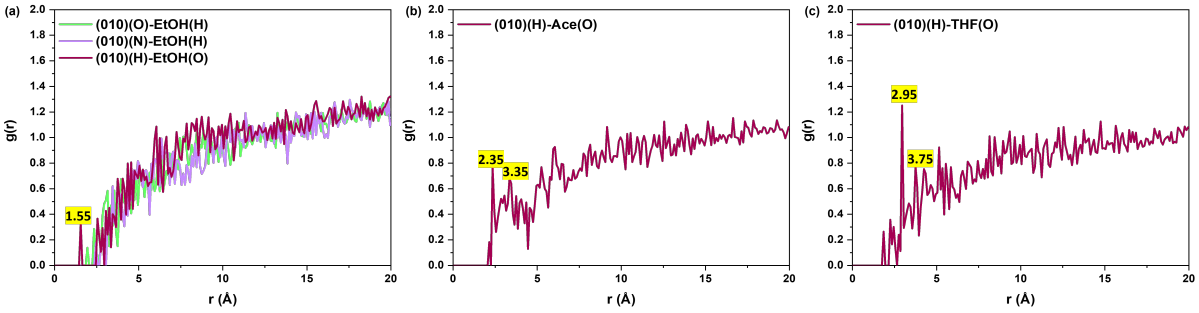


Figure 5.9: RDF analysis of the bonding between the (010) surface and (a) ethanol, (b) Acetone, and (c) THF

The primary difference, however, stems from the solubility of paracetamol in these solvents. Keeping all other crystallisation variables constant, the inherent differences in

solubility mean that the available solute for growth varies. For instance, the concentration of paracetamol in acetone was nearly 50% lower than in ethanol and 30% lower than in THF. Thus, while sufficient solute was present for crystal growth in each case, the ratio between solvent and solute molecules in solution differed, leading to a higher likelihood of favourable interactions in solvents with higher solubility [245]. This is particularly relevant during the regeneration phase when the (010) crystal face interacts with the solvent. After regeneration is complete and the (010) face disappears, the trend reverses, with growth rates in acetone surpassing those in THF, highlighting once again, the dominance of solute-solvent interactions with the morphologically important facets.

5.5 Conclusion

Using a newly designed isothermal crystallisation setup for single crystals, integrated with macrophotography, the regeneration of paracetamol in ethanol, acetone, and THF was observed. Precise measurements of the fast and slow regeneration times along with the growth rates was achieved with the aid of a crystal edge detection MATLAB script developed in house. It was found that the shape of the crystal prior to breakage has a large impact on the time taken for the regeneration to complete, even if the morphology of the crystals is the same. This difference in the initial habit being the effect of specific solute-solvent interactions with the facet. However, after cleavage, the (010) facet dominates growth, with its rate determined by the solubility of paracetamol in each solvent rather than solvent interactions. Higher solubility results in more favourable interactions of the crystal surface with the solute molecules and a faster rate of regeneration. Interestingly, once the (010) facet disappears after regeneration, solvent interactions regain influence, and overall growth rates once again depend on these interactions, as with the unbroken crystal.

Chapter 6

Effect of supersaturation and agitation on the regeneration rates of paracetamol crystals

6.1 Overview

Crystal growth is a two step process; diffusion followed by surface integration and therefore profoundly impacted by solution hydrodynamics. The final results chapter delves into the effect of supersaturation as well as solution stirring on the regeneration behaviour of crystals. The same experimental procedure and image analysis tool developed in chapter 5 were utilised to capture and measure the facet specific growth rates of paracetamol crystals during regeneration.

Three key observations were made in this study; firstly, although the rate of regeneration increased with supersaturation, the growth rate of (110) remained dormant at approximately 0.01 mm/hr regardless of the supersaturation until regeneration was complete, following which the growth rate increased with supersaturation. Secondly, even in the presence of agitation, the crystals demonstrated regeneration, emphasising that it is not

an artefact of solute accumulation at the cleavage plane. Finally, agitation also led to secondary nucleation, the onset of which varied depending on supersaturation as well as the type of crystal used; cleaved or whole.

The measured regeneration rates have been fitted to power law kinetics to understand the dependence of regeneration on supersaturation. Moreover, discussions revolving around 'memory effects' in crystals have been utilised to explain the 'turning on' and 'turning off' of facets that has not been observed in unbroken crystals. The chapter concludes by proposing a mechanism for the effect of crystal regeneration and growth on the onset of secondary nucleation which has previously not been studied.

6.2 Methods

6.2.1 Isothermal crystallisation with agitation

Paracetamol and ethanol were the primary chemicals used in this study, details of which can be found in Section 3.1. Paracetamol seeds and macroscopic crystals (4 mm) were obtained from ethanol using the procedure detailed in Section 3.3. Consequently they were cleaved using a scalpel to expose the cleavage plane (010) prior to being used in regeneration experiments. The methodology for cleaving the crystals can be found in Section 3.4 of this thesis. The same isothermal crystallisation set-up as outlined in Section 5.2.2 was used for the investigations of this chapter. A slight variation in the crystal immobilisation method was implemented, wherein to further secure the crystal and prevent it from moving due to solution flow, the cleaved crystal was directly stuck to the glass rod using a very small quantity of Loctite® super glue (figure6.1). To study the effect of agitation, firstly regeneration was carried out without any agitation at 5 different supersaturations; 1.03, 1.10, 1.17, 1.25, and 1.33. Following this, another set of experiments were carried out at the same supersaturations but in the presence of agitation. This was achieved by placing the jacketed vessel on a magnetic stirrer plate

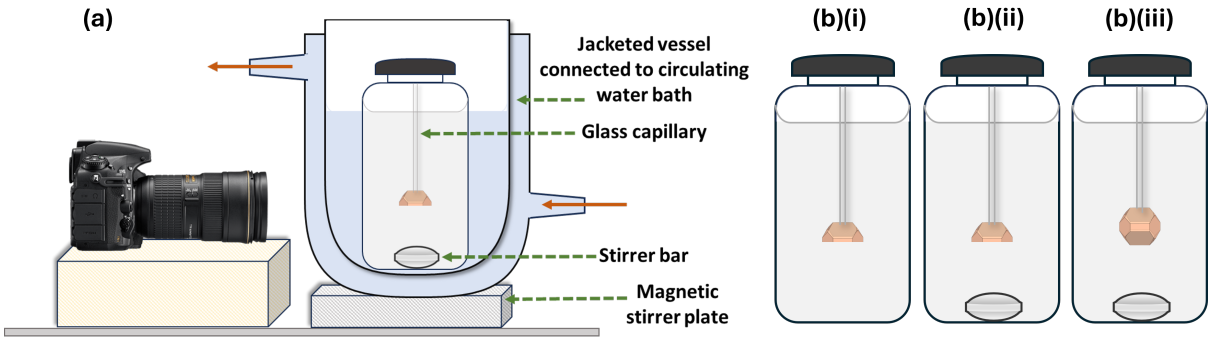


Figure 6.1: (a) isothermal crystallisation set-up with agitation using a magnetic stirrer (b)(i)-(iii) Cleaved crystal without agitation, cleaved crystal with agitation, whole crystal with agitation respectively, studied at 5 different S values; 1.03, 1.10, 1.17, 1.25, and 1.33

and stirrer the solution at 200 rpm with the aid of a PTFE magnetic stirrer bar. A set of control experiments were also conducted such that the same aforementioned experimental protocol was followed but instead of cleaving the crystals, the whole unbroken crystals were utilised. Figure 6.1(b) summarises the three crystal conditions tested, for which at least 3 crystals at each supersaturation were studied. The same temperature profile as seen in Figure 5.1(b) was implemented and in the case of agitation, the magnetic stirrer bar was introduced at the same time as the crystal. Images were taken between every 15-30 minutes depending on the supersaturation being tested. Images obtained from the DSLR camera were analysed using the edge detection MATLAB script detailed in Section 3.7.1, and the facet specific growth rates of (010) and (110) were measured (section 3.7).

6.3 Results

6.3.1 Metastable zone width determination

The solubility of paracetamol in ethanol was measured using the method detailed in Section 3.2 at 5 temperatures; 10°, 20°, 25°, 30°, 40°, and 50°, and a solubility curve was determined as seen in Figure 6.2. As the error associated with the measurements is small, error bars representing standard deviation are not visible and hence summarised in Table 5.1. The experimentally determined solubility showed good agreement with

the studies carried out by Granberg and Rasmuson [22], as well as by Fernandes [23] in literature. Consequently the MSZW was found as outlined in Section 3.2.1, at four different temperatures (25°, 30°, 40°, 50°), at 200 rpm and 0.1 °C/min cooling rate (Figure 6.2). Using the determined MSZW of 15.5 °C at a solubility temperature of 30 °C, five different supersaturations, S, were chosen for regeneration experiments; 1.03, 1.10, 1.17, 1.25, and 1.33, such that the S lies within the metastable zone and only crystal growth occurs.

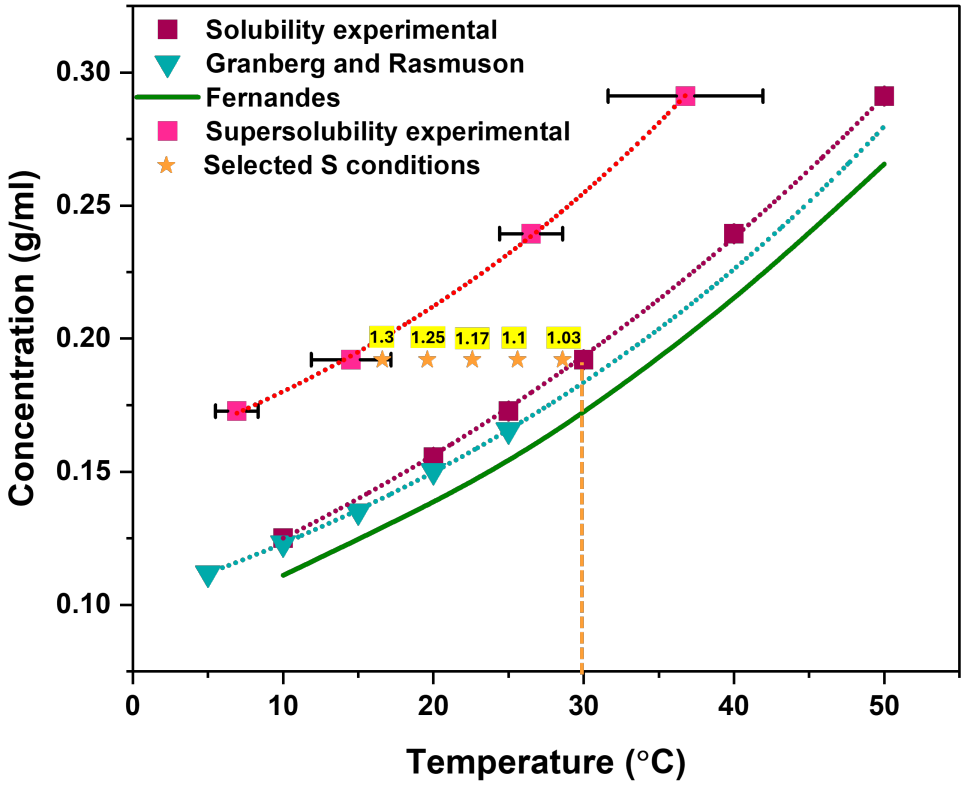


Figure 6.2: Solubility curve of paracetamol-ethanol system determined experimentally and compared against literature sources; Granberg and Rasmuson [22], and Fernandes [23]. Metastable zone width measured experimentally to select an ideal range of supersaturations for crystal growth experiments. Error bars represent standard deviation across a sample size of 3 repeats. Error bars for solubility curve are too small and hence can be found in Table 5.1

6.3.2 Effect of supersaturation on the rate of regeneration

Firstly, Figure 6.3 shows that the cleaved paracetamol crystal exhibited regeneration across all the supersaturations studied. The time required for regeneration decreased as

supersaturation increased, taking nearly 100 hours at a supersaturation of 1.03 and as little as 2 hours at 1.33. This point of regeneration completion was detected in the same way as detailed in chapter 5 Section 5.3.3.

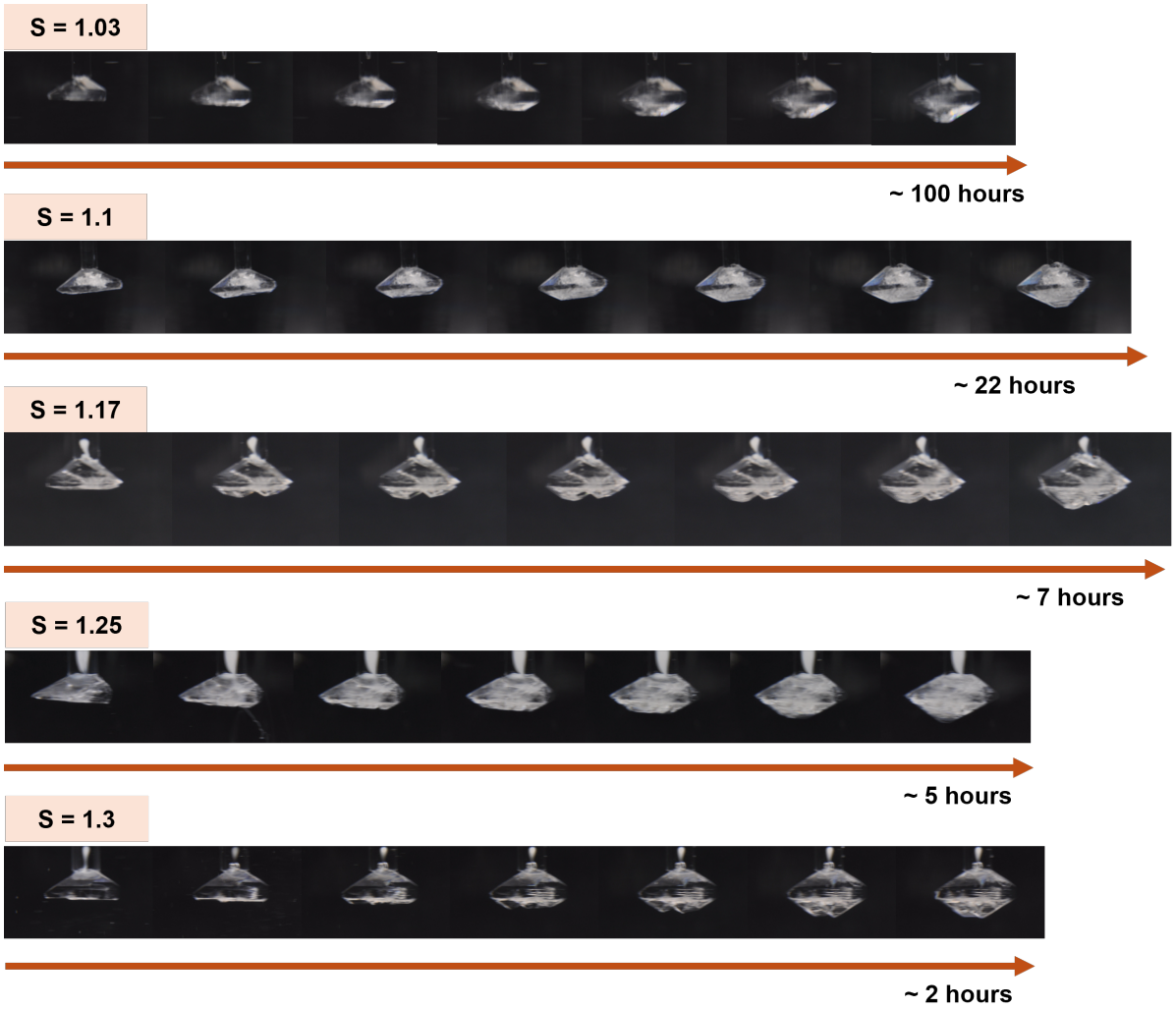


Figure 6.3: Snapshots of regenerating crystal at different supersaturation; top to bottom, 1.03, 1.10, 1.17, 1.25, 1.33, in non agitated systems along with the time taken to complete regeneration

To further quantify regeneration, three measurements were taken from the analysed images: facet propagation of (010) until regeneration completes, facet propagation of (110) on the unbroken side during regeneration, and facet propagation of (110) after regeneration is complete. Figure 6.4 shows example plots of these measurements for each supersaturation. In Figure 6.4(c), the x-axis starts at time 0, corresponding to the point of regeneration completion. Each experiment was limited to about twice the regeneration time to maintain constant supersaturation, except for $S = 1.03$, which was capped

at 120 hours due to time constraints. Consequently, linear trendlines were fitted to the growth plots and average growth rates over $n \geq 3$ samples for each supersaturation were obtained.

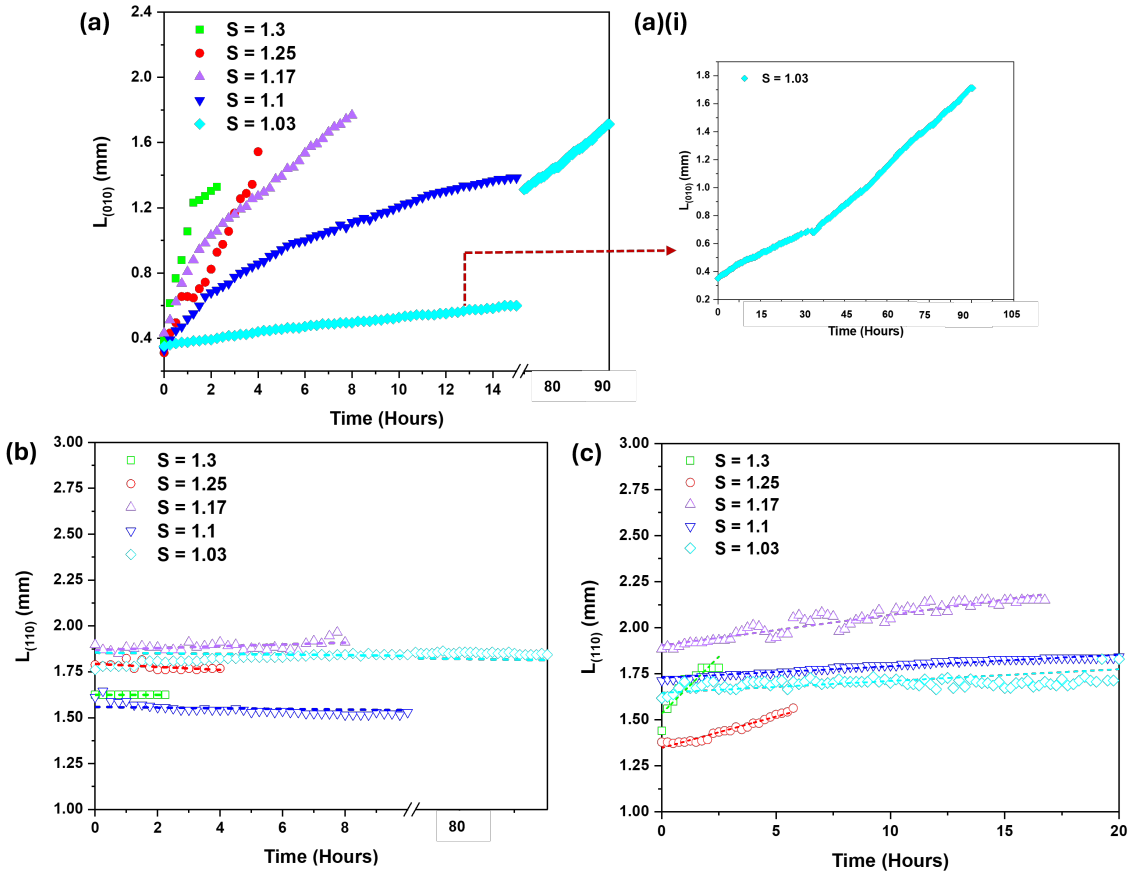


Figure 6.4: Example plots of crystal growth at each S obtained via MATLAB. Each line represents 1 individual crystal: (a) facet propagation of (010) during regeneration, (a)(i) a stand-alone plot showing the facet propagation of (010) for $S = 1.03$ to ensure data clarity. Facet propagation of (110) (b) during regeneration and (c) after regeneration. The gradients of these plots were used to estimate the growth rates.

As seen in Figure 6.5(a), the rate of regeneration, or, the growth rate of facet (010) increases exponentially with the supersaturation. Likewise, the time taken for regeneration to fully complete itself decreases exponentially with S. This consolidates that regeneration is not just limited to low supersaturation conditions. In the previous chapters it was also established that the facets on the unbroken side of the crystal remain relatively dormant during the rapid growth of (010). Here with the help of facet specific growth rates of (110) (Figure 6.5(b)), it is seen that regardless of the supersaturation, (110) on the unbroken side of the crystal grows at a rate of $\leq 0.03 \times 10^{-7}$ m/s up until regeneration

is complete. After which, the rate of (110) increases considerably with supersaturation. This difference in growth rates during and after regeneration is amplified at higher S.

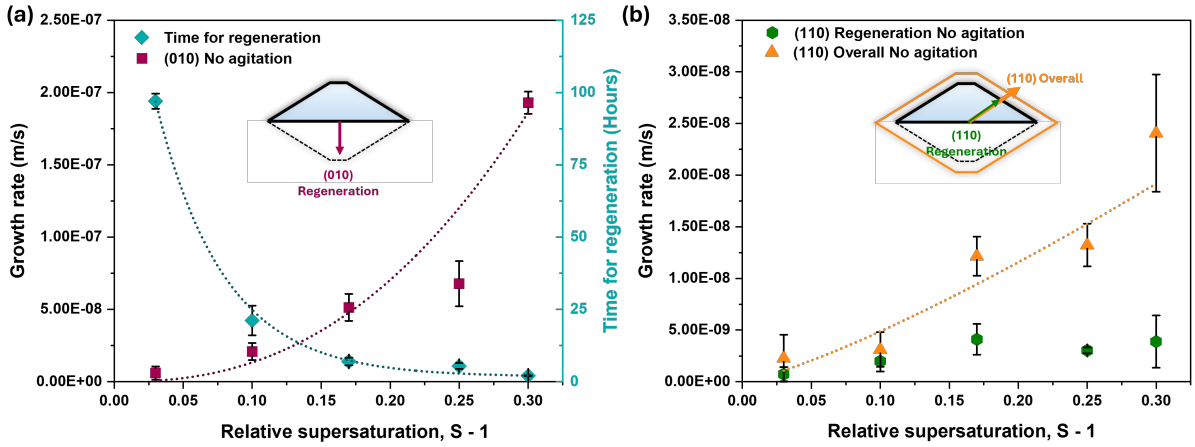


Figure 6.5: (a) Growth rate of (010) during regeneration as a function of supersaturation along with the time taken in hours for regeneration to finish at each supersaturation (b) Growth rates of facet (110) during regeneration (green) and after regeneration is completed (orange). Error bars demonstrate standard deviation

Table 6.1: Fast and slow regeneration rates of paracetamol in ethanol at different supersaturations

Relative Supersaturation S	**fast regeneration period** Hours	**% of Total regeneration period**	**Fast regeneration Rate** $(m/s)\ \times 10^{-7}$	**Slow regeneration Rate** $(m/s)\ \times 10^{-7}$
0.03	-	-	0.06 ± 0.01	0.06 ± 0.04
0.10	1.6 ± 0.1	$\sim 8.5\%$	0.44 ± 0.08	0.21 ± 0.06
0.17	0.8 ± 0.09	$\sim 11.5\%$	0.76 ± 0.20	0.51 ± 0.09
0.25	0.4 ± 0.06	$\sim 7.5\%$	0.96 ± 0.20	0.88 ± 0.08
0.33	0.2 ± 0.04	$\sim 9.5\%$	2.04 ± 0.50	1.93 ± 0.08

Furthermore, it is interesting to note that the regeneration mechanism proposed in chapter 4, also hold true at high supersaturations. Table 6.1 highlights the 'fast' and 'slow' regeneration rates as well as the duration of the fast phase. This is evident in the change in gradient of the $L_{(010)}$ lines in Figure 6.4(a). Unlike between $S = 1.10$ and 1.33, at $S = 1.03$, two distinct phases were not observed. The ratio of the growth rates in these regions was, $1.1 \leq G_{fast}/G_{slow} \leq 2.3$. Although the duration of the fast regeneration phase decreased with increasing S as the total time for regeneration itself decreases, it

still makes up approximately 10% of the total regeneration period irrespective of the supersaturation.

6.3.3 Effect of agitation on the rate of regeneration

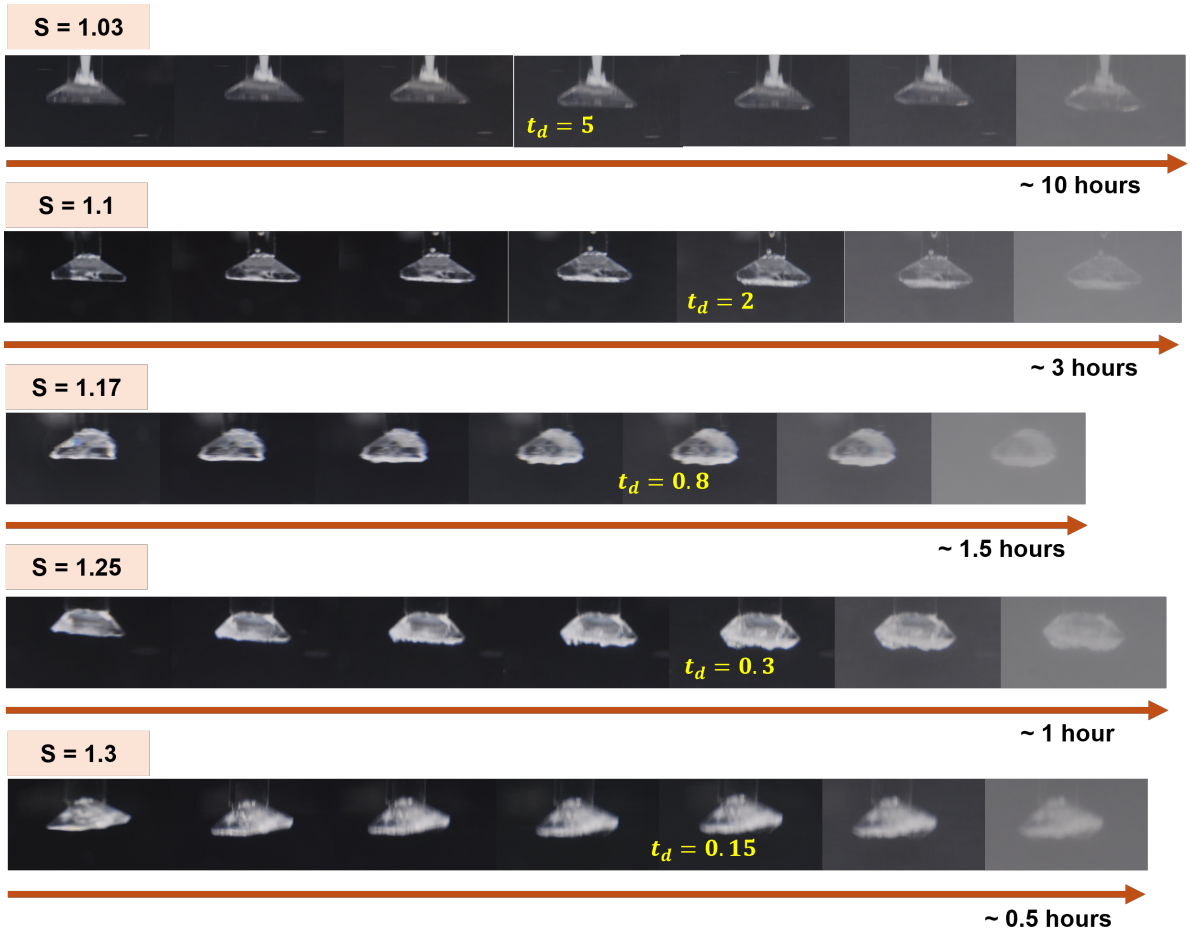


Figure 6.6: Snapshots of regenerating crystal at different supersaturation; top to bottom, 1.03, 1.10, 1.17, 1.25, 1.33, in agitated systems at 200 rpm

Figure 6.6 shows representative images of a cleaved crystal regenerating in the presence of agitation at different supersaturations. This consolidates that regeneration is not an artefact of solute accumulation at the cleavage plane due to the occurrence of concentration hotspots in a stagnant solution. However, before the regeneration could complete itself, nucleation occurred in the bulk of the solution which not only slowed down/halted the regeneration, due to a sudden drop in supersaturation, but also profoundly increased the solution turbidity making crystal detection impossible. Therefore the rate of regen-

eration was only measured up to the point just before nucleation was observed because beyond that point, the subsequent fall in concentration would affect the growth rate of (010) and it would no longer be a genuine representation of the phenomenon.

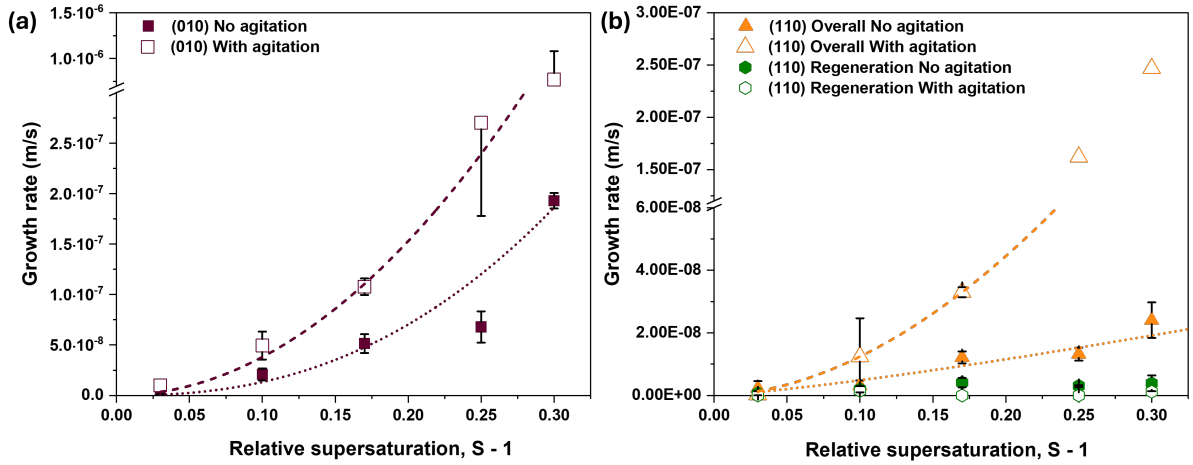


Figure 6.7: (a) Growth rate of (010) during regeneration as a function of supersaturation with and without agitation (b) Growth rates of facet (110) during regeneration and after regeneration is completed in the presence and absence of agitation

In order to compare the rate of regeneration with and without agitation, the time taken for the onset of nucleation in the stirred system was noted and the growth rate of (010) for the same duration in the unstirred system was calculated. This time frame also roughly corresponded to the fast regeneration phase of the non-agitated system. Figure 6.7(a) depicts the rate of (010) with and without agitation, and a clear difference in the trend lines can be seen where agitation results in faster regeneration rates, with the difference increasing with higher supersaturation. Surprisingly, agitation did not increase the growth rate of (110) during regeneration. From Figure 6.7(b), a considerable overlap in the data points for the (110) growth rates can be seen, irrespective of the supersaturation. Although counter intuitive, the preferred growth of (010) at an even higher rate in the presence of agitation further depletes the solute availability at the (110) facets, thus stifling their growth.

Since it was not feasible to track the growth rate of (110) after regeneration in the stirred system, whole unbroken crystals under the same conditions were observed (Figure 6.8). Considering the facet propagation of (110) of a whole crystal in a stirred system

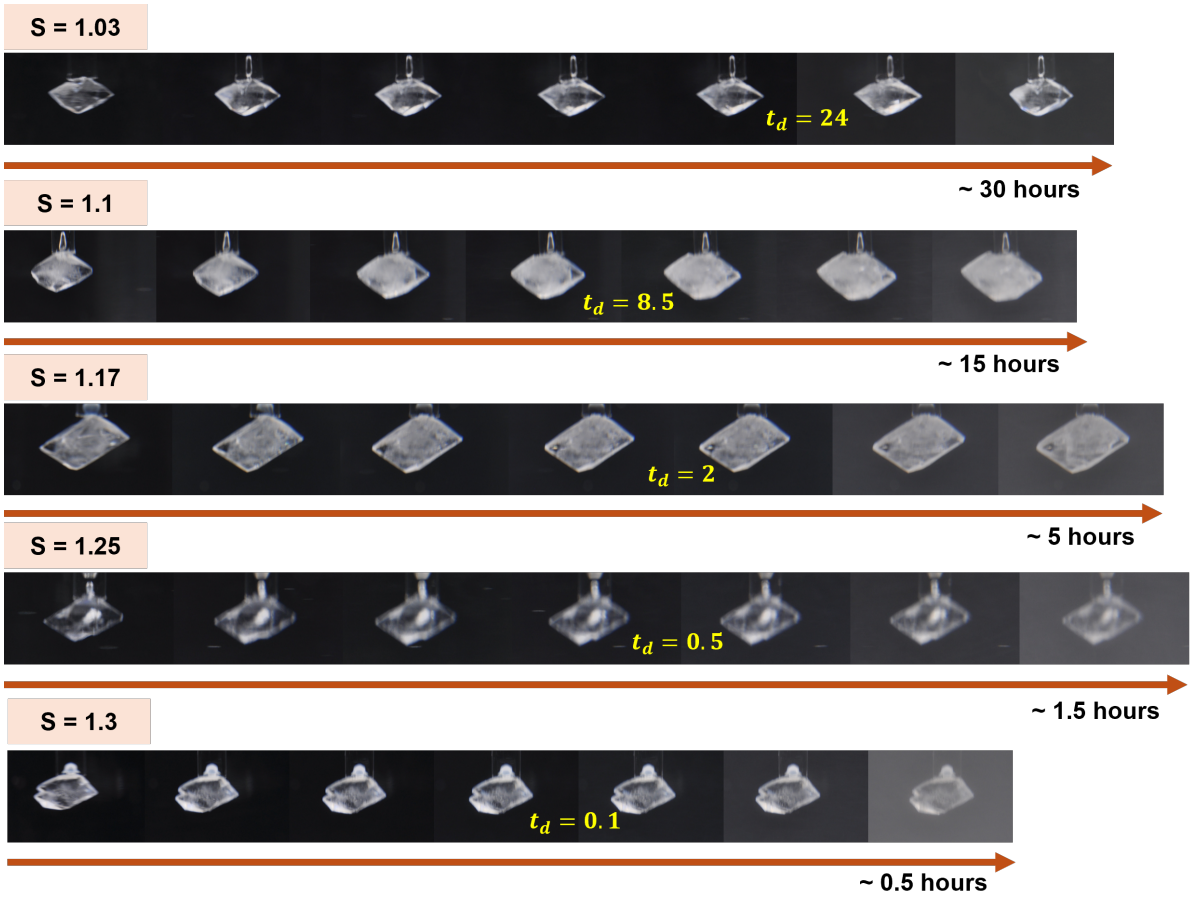


Figure 6.8: Snapshots of whole, unbroken crystals at different supersaturation; top to bottom, 1.03, 1.10, 1.17, 1.25, 1.33, in agitated systems at 200 rpm

to that of a regenerated cleaved crystal in an unstirred system, a substantial difference was observed. At 1.25 and 1.33, (110) grew 10 times faster in the presence of agitation. Looking at the agitation growth rates of (110), these are in agreeable orders of magnitude to the facet specific growth rates of paracetamol measured by Ristic et al. [20]. Moreover, a steep increase in the growth rates of (110) between supersaturations 1.15 and 1.25 was reported, which also supports our observation. The study suggests that at low supersaturations ($\leq$ 1.10), (110) shows no growth at all and only switches on at moderate to high supersaturations. Similarly in the data presented, although facet (110) was fully developed, the growth rate was 0 at a supersaturation of 1.03. Table 6.2 below summarises all the growth rates obtained at these conditions.

Table 6.2: Summary of the facet-specific growth rates of cleaved and whole paracetamol crystals in agitated and non-agitated environments with the time taken for secondary nucleation detection.

	Non-agitated Cleaved			Agitated Cleaved			Agitated Whole	
S - 1	$G_{(010)}$	$G_{(110)R}$	$G_{(110)}$	$G_{(010)}$	$G_{(110)R}$	t_d	$G_{(110)}$	t_d
		(m/s) $\times 10^{-7}$			*(m/s)* $\times 10^{-7}$	*(Hours)*	*(m/s)* $\times 10^{-7}$	*(Hours)*
0.03	0.06 ± 0.05	0.007 ± 0.007	0.02 ± 0.02	0.10 ± 0.05	0.00	4.9	0.003 ± 0.002	24
0.10	0.21 ± 0.06	0.02 ± 0.01	0.03 ± 0.02	0.49 ± 0.12	0.01 ± 0.01	2.3	0.12 ± 0.10	8.7
0.17	0.51 ± 0.09	0.04 ± 0.01	0.12 ± 0.02	1.08 ± 0.08	0.03 ± 0.02	0.83	0.33 ± 0.02	1.9
0.25	0.68 ± 0.16	0.03 ± 0.003	0.13 ± 0.02	2.70 ± 0.92	0.00	0.37	1.62 ± 0.002	0.47
0.33	1.93 ± 0.08	0.04 ± 0.002	0.24 ± 0.06	7.71 ± 3.11	0.00	0.16	2.47 ± 0.001	0.13

6.3.4 Secondary nucleation in agitated system

The major difference between the agitated and non agitated system was the onset of secondary nucleation, as seen in Figure 6.6. Secondary nucleation is the generation of nuclei in the presence of the parent crystal of the solute in solution [84]. This concept has been defined and discussed in detail in literature review Sections 2.2.2. Even though the same supersaturations were tested, no secondary nucleation occurred in the stagnant solution as opposed to in stirred conditions with a cleaved as well as a whole crystal. The total time taken for secondary nucleation to occur and detectable crystals to appear in the bulk solution, also called delay time, t_d [100, 93], was measured for the cleaved and the whole crystals, plotted in Figure 6.9. Two key observations were made; first, cleaved crystals in general led to shorter delay times and second, regardless of the crystal type, at higher supersaturations secondary nucleation occurred extremely quickly. At 1.33 supersaturation the whole and cleaved crystal both resulted in a delay time of 9 minutes whilst at 1.25 supersaturation, 28 and 22 minutes respectively. This difference in the t_d progressively widened at lower supersaturations, reaching a 20 hour difference at $S = 1.03$.

$$t_{ind} = 24390 \times \Delta T^{-2.276} \tag{6.1}$$

The induction times, t_{ind} at various supersaturations for paracetamol-ethanol solution at a saturation temperature of 30 °C was measured by Mitchell et al. [24] and found to fit the function 6.3.4, based on the induction time theory developed by Kubota [246], where

ΔT is the degree of supercooling in °C.

This data can be seen in Figure 6.9, as a red curve, for comparison between induction times and delay times. As expected the delay times did not show any overlap with the induction time, where the detection of particles via primary nucleation in unseeded solutions takes considerably longer than the detection of particles via secondary nucleation. This difference between the t_d and t_{ind}, also increases at lower supersaturations with unseeded experiments taking around 100 hours to nucleate.

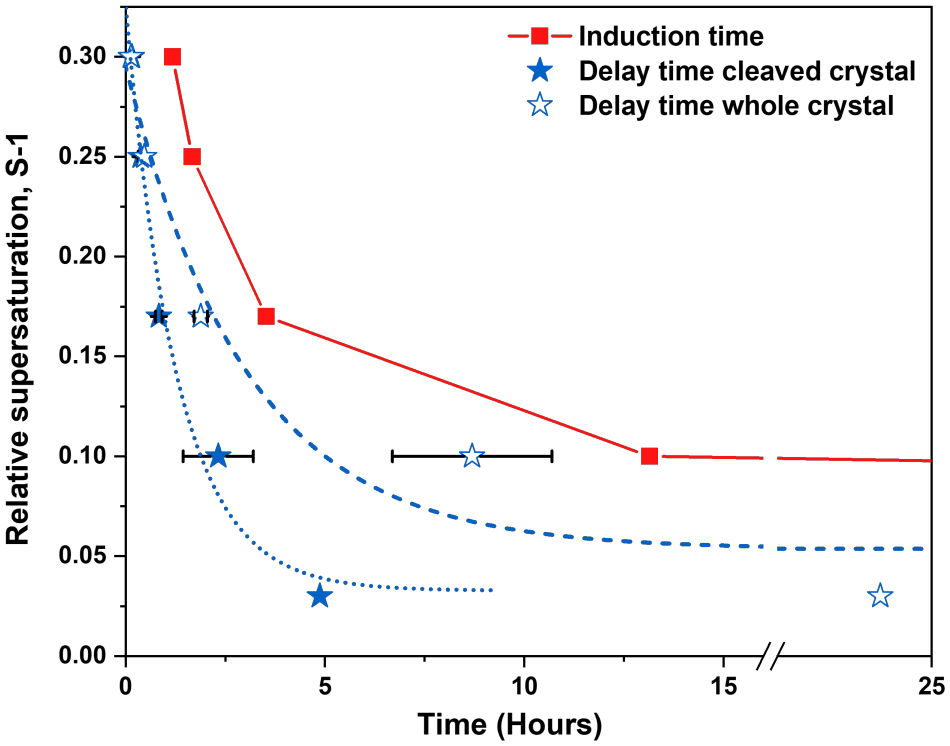


Figure 6.9: Plot depicting the delay time, t_d, for a cleaved crystal and a whole crystal grown in agitated conditions in comparison to the induction time data of paracetamol-ethanol solutions studied by Mitchell et al. [24]

6.4 Discussion

The most intriguing observation was that during the fast regeneration phase, all other facets on the crystal remain dormant. Although it is understandable that the crystal is prioritising stability by fast growth of (010), it still unclear as to how this rapid growth completely overwhelms growth on other facets. It was thought that perhaps the stagnant

solution results in selective deposition of solute molecules on the cleavage plane, thus hindering the growth of all other facets. However, even in a well mixed system, growth only on the (010) facet was preferred during fast regeneration. It was postulated that the selective 'turning on' and 'turning off' of facets could perhaps be a mechanism of crystals demonstrating 'shape-memory effect' that allows them to 'remember' their pre-breakage shape and return to it. Although this has only been seen in a few organic crystals that demonstrate shape and phase restoration after undergoing plastic bending [187], it could be a potential explanation. This effect in conjunction with surface energetics, where the freshly exposed thermodynamically unstable facet tries to grow rapidly to minimise the overall surface energy, may result in the temporary cessation of pre existing facets. Further atomic-level simulations are needed to clarify local facet behaviour and draw definitive conclusions.

As discussed in detail in Section 2.3.5, crystal growth involves 2 distinct steps: bulk diffusion of solute particles through the solute-solvent boundary layer, followed by surface integration of the solute particles into the crystal lattice. Bulk diffusion and surface integration occur in series and therefore the slower of the two, governs the crystal growth. When surface integration is the rate limiting step, solution hydrodynamics do not have any effect on the growth rate unlike when growth is diffusion limited. As the data clearly shows an increase in growth rates in the presence of agitation at 200 rpm, growth in the stagnant system can be classified as mass transport/diffusion limited. Therefore, the growth rates can not be fitted to the spiral growth (BCF), Birth and Spread (B&S), or the rough growth models that are only valid when surface integration is rate limiting. Faster growth rates in the presence of agitation mean an enhancement in the mass transfer due to the decrease in the width of the boundary layer in solution. Normally to understand growth kinetics, agitation rates are increased until growth becomes surface integration limited and no more increase in growth rates is observed [144, 143]. As the main aim of this work was to elucidate the implications of a stirred system on the regeneration phenomenon in contrast to a stagnant one, only one agitation rate was studied. So even though an increase in growth rates was observed, a surface integration limited

Table 6.3: Parameters of the power law equation fitted to the facet specific growth rates of cleaved and whole paracetamol crystals

Facet	**Phase**	**Condition**	$\mathbf{R^2}$	k_g $(m/s \times 10^{-7})$	g
(010)	Regeneration	No agitation	0.967	33.50	2.40
(010)	Regeneration	With agitation	0.871	38.60	2.00
(110)	Overall	No agitation	0.848	0.86	1.25
(110)	Overall	With agitation	0.999	8.65	1.84
(110)	Regeneration	No agitation	N/a	N/a	N/a
(110)	Regeneration	With agitation	N/a	N/a	N/a

regime can not be ascertained. Therefore the growth rates were fitted to the power law equation (2.3.6) to elucidate the dependence of regeneration on supersaturation. The fitted parameters k_g and g, for each facet are shown in Table 6.3 along with the crystallisation condition and the R^2 value. The power law shows a good fit for the (010) facet without agitation and the (110) facet with agitation, with R^2 values of 0.967 and 0.999, respectively. Although the fit for the other two conditions is less optimal, all parameters remain within acceptable ranges when compared to reported paracetamol growth kinetics in the literature [145]. The key takeaway from these findings is that the regeneration rate, specifically the growth of the (010) facet, exhibits a stronger dependence on supersaturation compared to the other facets.

The major point of discussion highlighted from the results is the observation of secondary nucleation during growth in stirred conditions (Figure 6.9). Although various studies have been undertaken to understand secondary nucleation as well as single crystal growth, as seen in Sections 2.2.2 and 2.3 respectively, the dependence of one on the other is rarely reported. As the cleaved and whole crystals being studied were immobilised, there was no possibility for crystal-crystal, crystal-wall, and crystal-stirrer collisions. Thus contact secondary nucleation was disregarded as a feasible SN mechanism. It was postulated that the source of SN was most likely to be crystal nuclei breeding where the surface of the crystal enable the formation of stable nuclei from the pre-existing solute clusters in solution [7, 92]. These nuclei are weakly bound to the crystal surface and are therefore swept away by the agitated fluid, leaving the crystal surface available again for nucleation.

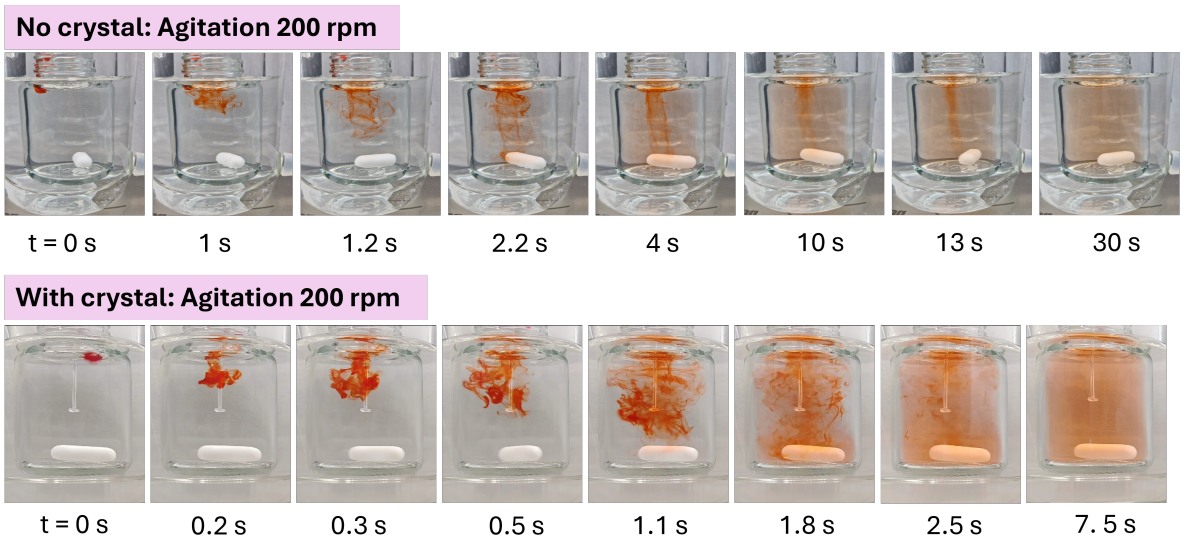


Figure 6.10: Displacement of red dye in solution being stirred using magnetic stirrer at 200 rpm (top) without, and (bottom) with the presence of an immobilised crystal

To demonstrate homogeneous mixing in the agitated system and verify surface breeding as a viable mechanism for secondary nucleation (SN), a quick mixing test was conducted. A few drops of orange dye (5 ml in total for each case) were introduced into the solution, first in the absence of a crystal (Figure 6.10 (top)) and then in the presence of an immobilised crystal (Figure 6.10 (bottom)), with the movement of the dye tracked in each case. In the absence of a crystal, a vortex forms at the centre, creating a dead zone with inefficient mixing. As shown in Figure 6.10 (top), this results in the development of a dye column in the middle of the jar, where the vortex is located, taking approximately 30 seconds to dissipate evenly throughout the solution. However, when a glass rod and crystal are introduced at the centre of the jar (Figure 6.10 (bottom)), the vortex is eliminated, and the dye disperses evenly in about 8 seconds. This observation confirms effective mixing in the solution and highlights a potential source for secondary nucleation.

Two key observations were mentioned in Section 6.3.4, where cleaved crystals as well as high supersaturations (irrespective of whole or cleaved) lead to a rapid onset of secondary nucleation. Only considering the crystal type, the freshly cleaved (010) facet is topologically more uneven compared to the fully developed facets of the whole crystal. This can be seen in the SEM images (Figure 4.11) in chapter 4. Therefore a higher surface area would mean lower interfacial energies at the (010) surface and an increased probability

of inducing secondary nucleation of the solute clusters, resulting in lower t_d. However, a bigger question arises: how does the growth rate of a crystal affect the delay time? In every scenario, regeneration/growth was observed prior to secondary nucleation. So, it could be argued that if the facet is growing extremely quickly then most of the solute molecules interacting with the crystal surface are being integrated into the crystal lattice, leaving less available for secondary nucleation and resulting in higher t_d, however the opposite is observed. At the same agitation rate, supersaturation, and temperature, a cleaved crystal is growing at least 2 times faster than the whole crystal, so what is causing the early onset of SN?

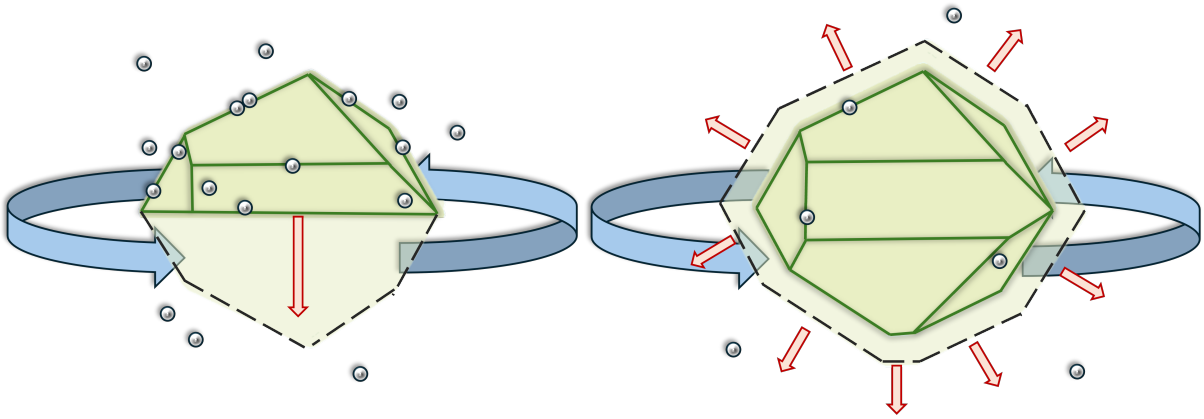


Figure 6.11: Proposed mechanism of the effect of regeneration on the occurrence of secondary nucleation in stirred systems

It was hypothesised that the secondary nucleation and crystal growth compete in solution, and an interplay between their energy barriers favour one over the other. At very high supersaturation, $S = 1.33$ and 1.25, the t_d for cleaved and whole crystals is relatively similar. It was postulated that the activation energy barrier for SN and growth are both very low. Hence, they don't affect one another - regeneration of the cleaved crystal and SN as well as growth of the whole crystal and SN can coexist. Due to the high S, secondary nucleation happens in the bulk solution itself with minimal aid from the surfaces [7]. The bigger difference appears at low and medium supersaturation, $S = 1.03$, 1.10, and 1.17. It is suggested that the nuclei breeding is dominated by the dormant facets. As the cleaved crystal has only 1 fast growing facet as opposed to the whole crystal which is growing evenly in all directions, it has more facets that do not need to

compete between SN and growth. This increases the available surface area for nuclei breeding. Moreover as S increases (from 1.03 to 1.17), t_d still decreases with an increase in growth rate regardless of a cleaved or whole crystal. This is probably because with a higher S, the energy barriers for SN and growth are both decreasing and the solution can facilitate both. The large volume allows S to remain constant whilst the even mixing ensures no concentration hotspots occur. This proposed mechanism has been visualised as a diagram in Figure 6.11.

6.5 Conclusion

Regeneration was observed in a range of supersaturations from $S = 1.03$ to $S = 1.33$ in the absence and presence of agitation. This confirmed that neither is regeneration limited to low supersaturations nor is it an artefact of solute accumulation at the cleavage plane in a stagnant solution. Facet specific growth rates of (010) and (110) during and after regeneration were measured with the aid of MATLAB image analysis and consequently fitted to obtain power law kinetics. It was demonstrated that the regeneration rate has a stronger dependence on supersaturation than the growth rate of facet (110). Regeneration is also highly impacted by solution hydrodynamics, especially when it is not occurring in the surface integration regime, such that enhanced mass transfer in the presence of agitation led to faster regeneration. It was also shown that regeneration aids the onset of secondary nucleation due to the availability of dormant facets for nuclei breeding, which could potentially be used as a seeding strategy to lower crystallisation times. This peculiarity in terms of selective cessation of facets during the regeneration process also hints at 'shape-memory' effect in crystals and needs to be explored further.

Chapter 7

Conclusions and Future Work

7.1 Overall Contributions and Conclusions

This thesis reports on a previously unobserved regeneration phenomenon in organic crystals, especially paracetamol, post breakage along their cleavage plane. The mechanistic understanding of this phenomenon, the effect of crystallisation conditions on it, and its implications on other aspects of crystallisation have been studied and discussed across the chapters. To summarise, the following are the key achievements, takeaways, and potential applications emerging from this work:

1. A systematic study was designed to investigate crystal growth post breakage which currently lacks understanding. This involved obtaining high quality, single macroscopic crystals of paracetamol, followed by a procedure to neatly break them along the cleavage plane. This established the groundwork required to carry out sequential and thought out experiments to study crystal growth.

2. 'Crystal regeneration' was reported for the first time, wherein a paracetamol crystal was shown to grow back to its original pre-breakage shape via rapid advancement of the (010) facet before demonstrating overall growth. This process was found to be analogous to the 'self-healing' phenomena found in nature such as a lizard regrowing

its tail after autotomy. This suggested that growth after breakage is dominated by fast growing facets as opposed to slow growing facets as in the case of unbroken crystals.

3. Novel imaging rigs utilising macrophotography, compatible with evaporative as well as isothermal crystallisation were designed to capture the regeneration phenomenon under various conditions. Moreover, an automated image analysis script was developed using MATLAB that works on the principle of 'edge detection' and was used to obtain precise crystal growth rates efficiently.

4. Regeneration was shown to be dependent on the orientation and extent of breakage but not on the initial size of the crystal. Regardless of the amount of breakage, cuts parallel to the cleavage plane resulted in regeneration whilst those perpendicular to the cleavage plane did not. Growth perpendicular to facet (010) in cleaved crystals was 3x faster than both parallel growth in cleaved and perpendicular growth in unbroken crystals, with the majority of regeneration occurring in the first 25 hours, one-fifth of the total 125-hour regeneration period.

5. Regeneration occurred in paracetamol crystals regardless of the solvent used (ethanol, THF, acetone), with the fastest rate in ethanol (0.07 mm/hr), followed by THF (0.03 mm/hr), and the slowest in acetone (0.02 mm/hr). In all solvents, regeneration was completed within 24 hours at a supersaturation of 1.10, with the rapid regeneration phase occurring in the first 8-15% of this period. Interestingly, after regeneration, the growth trend reversed, being fastest in ethanol, followed by acetone, and slowest in THF.

6. It was proved that regeneration is not an artefact of the crystallisation conditions but an inherent crystal growth behaviour since it was observed over a range of supersaturation ($S = 1.03$ to $S = 1.33$), and in the presence as well as absence of agitation. Not only were the growth rates of (010) between 3-8 times faster than the growth rates of (110) after regeneration, but during regeneration, the growth of (110) was seen to be temporarily 'switched-off' regardless of the crystallisation

condition.

7. Peculiar crystal behaviour arising as a result of regeneration have also been discussed in detail. In chapter 5, it was suggested that in a regenerating crsytal, paracetamol solubility has a dominating effect on the growth rate of (010) over the intermolecular interactions between solute and solvent. The cessation of surrounding facets during regeneration, reported in chapter 6, was postulated to be due to 'shape-memory' effect in crystals in conjunction with surface energetics

8. Two new mechanisms have been proposed:

   - Regeneration mechanism (chapter 4): The regeneration process in crystals occurs in 2 stages, fast regeneration and slow regeneration, before progressing towards overall crystal growth. This holds true regardless of the crystallisation condition

   - Effect of regeneration on secondary nucleation: This mechanism suggests that the dormant facets on the regenerating crystal aid the rapid onset of SN via nuclei breeding in comparison to an unbroken crystal where all facets are advancing and therefore competition between growth and SN is more pronounced

9. Finally, based on the results and discussion across the chapters, the regeneration phenomenon serves as a warning to consider post-breakage growth kinetics in process modelling and not treat it similar to that of unbroken crystals, in order for more accurate crystal shape and size prediction. This phenomenon also highlights the gaps in the current understanding of fundamental crystal growth and hence opens up new avenues for engineering the 'perfect' crystals. Finally, due to the increased growth kinetics and secondary nucleation times during regeneration, cleaved crystals have the potential to serve as a promising seeding strategy for enhancing batch crystallisation.

7.2 Future Work

7.2.1 Recyclability of crystals

Preliminary results have shown that a regenerated crystal can be cleaved again and both the resulting halves can demonstrate regeneration. This is a crucial step in order to understand the number of cycles of regeneration a crystal can undergo before completely 'dying'. The aim of this work is to eventually investigate how the crystal properties such as purity, form, shape, dissolution rates, melting points, etc change with every cycle.

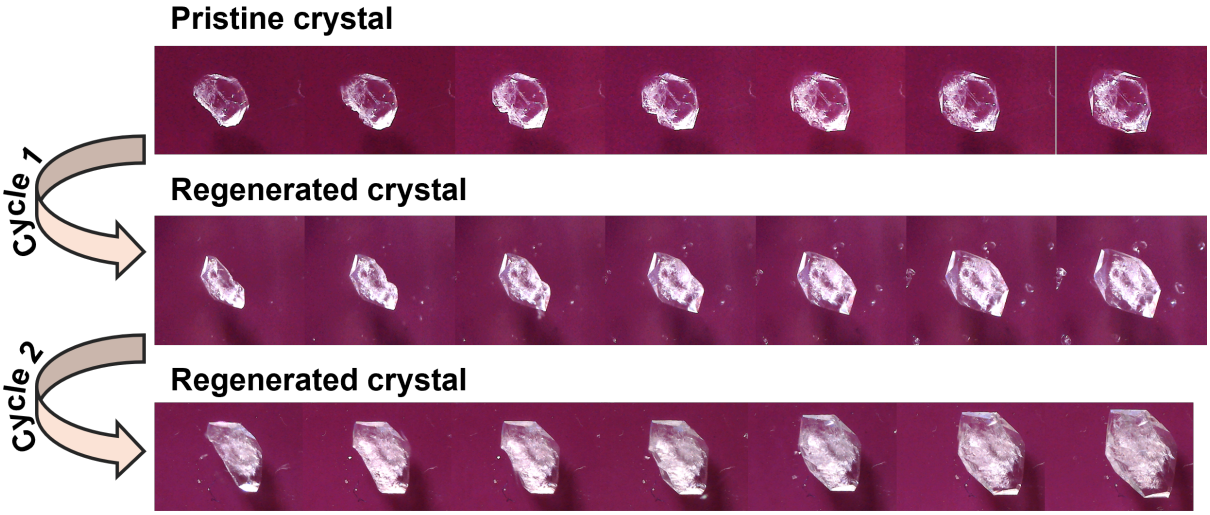


Figure 7.1: Snapshots depicting the regeneration of a pristine cleaved crystal followed by 2 cycles of further regeneration post cleavage of the regenerated crystal

7.2.2 Effect of crystal orientation

All isothermal crystallisation experiments in the presence of agitation carried out in chapter 6 involved immobilising the crystal with its cleavage face down. Here it was hypothesised that depending on the orientation of the cleavage plane with reference to the flow direction, the regeneration rate and behaviour could potentially be affected. With the cleavage plane facing downwards the fluid profile and therefore the trajectory of solute molecules would vary in comparison to if the crystal was oriented sideways and the cleavage plane was either facing in the direction of the flow or against the flow. Hence

preliminary experiments were carried out with an International Research Opportunities Programme (IROP) student, Hirokatsu Yoshioka, as part of student supervision, to study the effect of crystal orientation. Initial findings have shown that regeneration does occur when the cleavage plane is oriented against the fluid flow (Figure 7.2). However more work needs to be done do quantify the rates and compare them with other orientation scenarios.

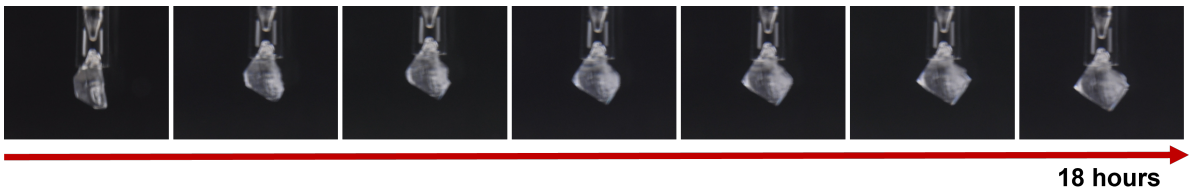


Figure 7.2: Snapshots of a cleaved crystal regenerating, despite being oriented with the cleavage plane facing sideways

7.2.3 Automated optical microscopy for regeneration screening

To increase the throughput of data from the evaporative crystallisation experiment and steer it in the direction of a regeneration 'screening' technique, a more automated approach was undertaken. Crystallisation dishes were prepared in the same manner as detailed in Section 4.2.2 and placed in the fumehood. A system was designed wherein a RS90 USB microscope was attached to a Dobot magician robotic arm such that top down crystal imaging could be done through the glass lid. A python script has been developed by a member of the Heng Group, Hamish Mitchell, to control the movement of the arm so that multiple crystallisation dishes could be imaged at once, at regular and shorter time intervals. This enabled imaging to be done continuously over a desired period of time, without having gaps in data from nighttime and weekend measurements as was the case with manual imaging. Furthermore, the set-up is currently being adjusted to enable isothermal crystallisation capabilities, with the help of waterbaths and jacketed vessels, so that screening of regeneration can be carried out in controlled environments (Figure 7.3(b)).

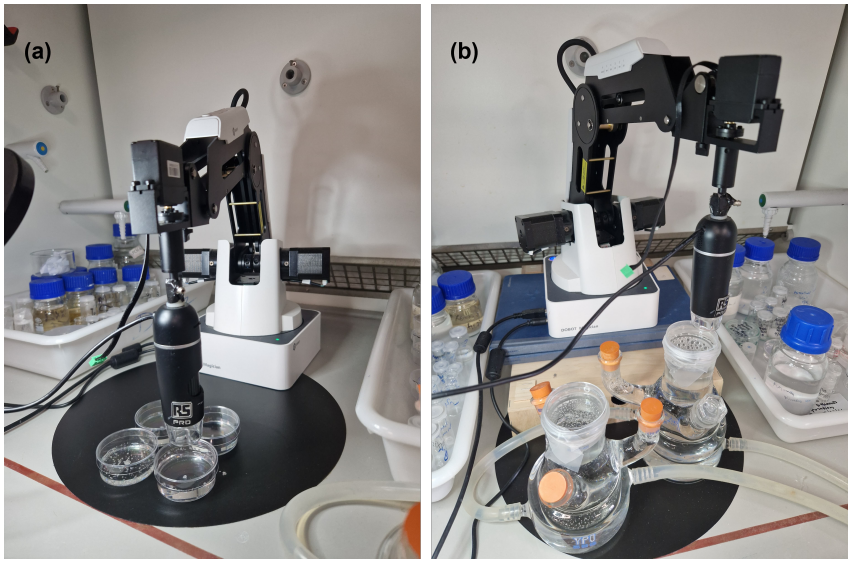


Figure 7.3: Automated imaging set-up using Dobot, the robotic arm, and USB microscope for cystal imaging in (a) evaporative crystallisation environment, and (b) isothermal crystallisation environment

7.2.4 Regeneration in other organic crystal

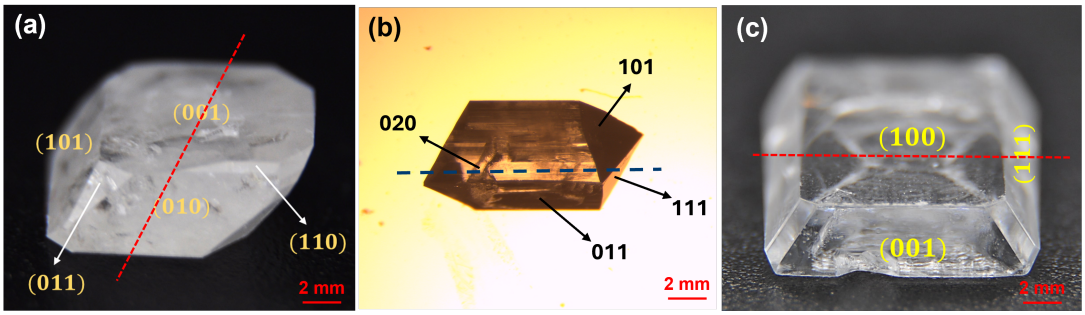


Figure 7.4: Macroscopic crystals of (a) carbamazepine, (b) glycine, and (c) aspirin obtained from methanol, DI water, and acetone respectively

A few other systems have been screened for regeneration using the automated imaging set-up discussed above. Carbamazepine, aspirin, and α glycine crystals were grown and regenerated in methanol, acetone, and DI water respectively. This work has been done in conjunction with a visiting student, Karolina Stankova, as part of student supervision undertaken during this PhD. Preliminary results have shown that regeneration occurring in CBZ and α glycine post breakage exposing their cleavage planes, (111) and (200) respectively, which are also fast growing planes. Aspirin on the other hand, has a morphologically important cleavage plane, (001), and therefore does not demonstrate regeneration. Figure 7.4 and 7.5 show the experimental habits of the CBZ, glycine, and

aspirin crystals grown in the lab and their growth behaviour post breakage respectively.

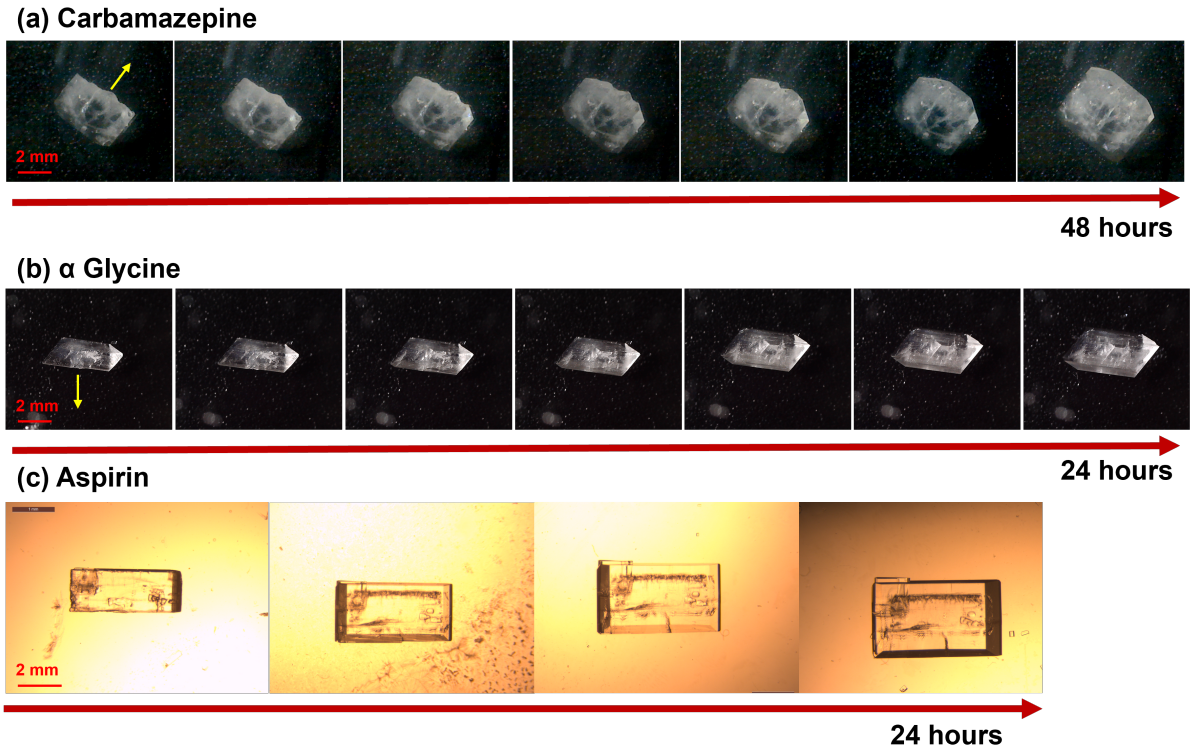


Figure 7.5: Snapshots representing the regeneration behaviour observed for (a) carbamazepine in methanol, (b) glycine in DI water, and (c) aspirin in acetone over a period of 48 and 24 hours respectively

Appendix A

Results

A.1 Growth rates of large crystals

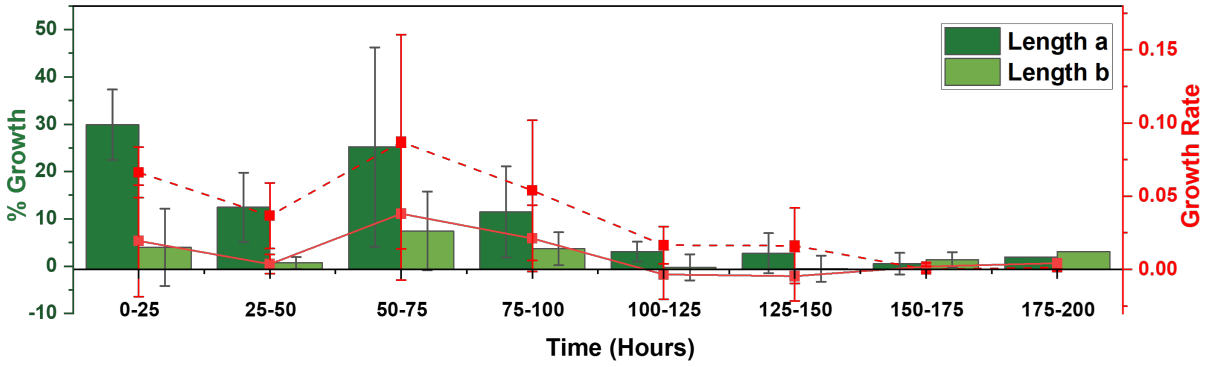


Figure A.1: % Growth and growth rate of length a and b for large cleaved paracetamol crystals over a period of 200 hours. Error bars represent standard deviation across 3 crystals

Figure A.1 shows the growth rates of large cleaved crystal where a trend similar to that of small crystals was observed – regeneration takes place in 2 phases followed by slow overall growth. However, due to the size difference, the larger crystals regenerate over a longer period of time – phase 1 from 0-75 hours corresponding to rapid regeneration and phase 2 from 75-150 hours corresponding to slow regeneration. As can be seen from Table A.1 the average growth rates for a small and large cleaved crystal for the characteristic lengths a and b are relatively similar. However, the wide standard deviation of the growth rates of

the larger crystal highlights the crystal to crystal variability during growth mainly due to temperature fluctuations. Hence, further repeat experiments need to be done to validate the growth rates of the large crystals to draw meaningful conclusions on the effect of initial crystal size on regeneration.

Table A.1: Growth rates of small and large crystals in the different phases of regeneration along with the standard deviation in mm/hr

	Length a		**Length b**	
Initial Crystal Size	*Small*	*Large*	*Small*	*Large*
Phase 1	0.064 ± 0.009	0.063 ± 0.038	0.021 ± 0.004	0.020 ± 0.029
Phase 2	0.021 ± 0.002	0.029 ± 0.009	0.027 ± 0.002	0.004 ± 0.018
Overall Growth	0.025 ± 0.004	0.002 ± 0.003	0.028 ± 0.005	0.003 ± 0.002

A.2 Hardness of facets before and after regeneration

Preliminary results on the hardness of facets (201) and (011) measured before and after regeneration

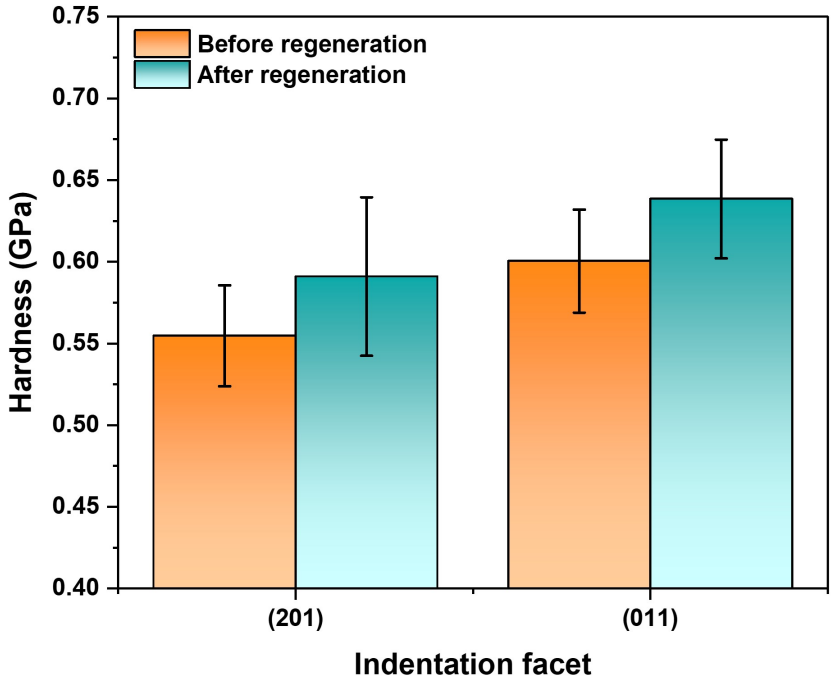


Figure A.2: Hardness of facets (201) and (011) before and after regeneration

A.3 MATLAB script for Image analysis

```
function Final_Dobot_Script_copy()
clc;
clear;
workspace;
format long g;
format compact;
fontSize = 10;

% Check that user has the Image Processing Toolbox installed.
hasIPT = license('test', 'image_toolbox');
if ~hasIPT
    % User does not have the toolbox installed.
    message = sprintf('Sorry, but you do not seem to have the Image Processing Toolbox.\nDo you want to try to continue anyway?');
    reply = questdlg(message, 'Toolbox missing', 'Yes', 'No', 'Yes');
    if strcmpi(reply, 'No')
        % User said No, so exit.
        return;
    end
end

% Specify the folder where the files live.
myFolder ="C:\Users\Isha Bade\OneDrive - Imperial College London\PhD\Experimentation\jacketed vessel\Cooling regeneration\GLycine";
% Check to make sure that folder actually exists.  Warn user if it doesn't.
```

```
24 if ~isfolder(myFolder)
25     errorMessage = sprintf('Error: The following folder does not
           exist:\n%s\nPlease specify a new folder.', myFolder);
26     uiwait(warndlg(errorMessage));
27     myFolder = uigetdir(); % Ask for a new one.
28     if myFolder == 0
29          % User clicked Cancel
30          return;
31     end
32 end
33
34 % Get a list of all files in the folder with the desired file
       name pattern.
35 filePattern = fullfile(myFolder, '*.png'); % Change to whatever
       pattern you need.
36 theFiles = dir(filePattern);
37 Data = [];
38 for m = 1 : length(theFiles)
39     baseFileName = theFiles(m).name;
40     fullFileName = fullfile(theFiles(m).folder, baseFileName);
41     fprintf(1, 'Now reading %s\n', fullFileName);
42
43     I = imread(fullFileName);
44     I2 = imcrop(I,[442.51 203.51 521.98 327.98]);
45     I3 = rgb2gray(I2);
46     I4 = medfilt2(I3,[1 1]);
47     I5 = imfill(I4);
48     grayImage = adapthisteq(I5,'NumTiles',[8 8],'ClipLimit',0.01)
           ;
49     image_thresholded = grayImage;
50     image_thresholded(grayImage>100) = 256;
```

```
51      image_thresholded(grayImage<=100) = 0;
52
53      se = strel('line',1,90);
54      dilatedI = imdilate(image_thresholded,se);
55      BW2 = imfill(dilatedI,'holes');
56
57      se2 = strel('disk',5);
58      BW3 = imclose(BW2,se2);
59      BW4 = imfill(BW3,'holes');
60      BW5 = bwareaopen(BW4, 5);
61
62      D = -bwdist(~BW5);
63      Ld = watershed(D);
64      bw2 = BW5;
65      bw2(Ld == 0) = 0;
66      mask = imextendedmin(D, 0.01);
67      D2 = imimposemin(D,mask);
68      Ld2 = watershed(D2);
69      bw3 = BW5;
70      bw3(Ld2 == 0) = 0;
71
72      props = regionprops(bw3, 'Centroid', 'Area');
73      BW6 = bwpropfilt(bw3,'area',[200 1500000]);
74      BW7 = bwconvhull(BW6);
75
76      boundaries = bwboundaries(BW7);
77      numberOfBoundaries = size(boundaries, 1);
78      for k = 1 : numberOfBoundaries
79          thisBoundary = boundaries{k};
80          plot(thisBoundary(:,2), thisBoundary(:,1), 'g', '
            LineWidth', 1);
```

```
81      end
82      caption = sprintf('%d␣Outlines', numberOfBoundaries);
83      title(caption, 'FontSize', fontSize);
84      firstBoundary = boundaries{1};
85
86      x = firstBoundary(:, 2);
87      y = firstBoundary(:, 1);
88
89      subplot(1, 2, 1);
90      imshow(I2, []);
91      axis image;
92      hold on;
93      plot(x, y, 'r-', 'LineWidth', 1);
94      title('Overlayed␣boundary', 'FontSize', fontSize)
95      set(gcf, 'Units', 'Normalized', 'OuterPosition', [0 0 1 1]);
96      set(gcf, 'Name', 'Crystal␣boundary␣and␣size', 'NumberTitle',
            'Off')
97
98      info = regionprops(BW7,'Orientation');
99      A = struct2table(info);
100     Orientation = table2array(A(:,1));
101
102     Rotationorder = -Orientation;
103     box1 = imrotate(BW7,Rotationorder,'bilinear','crop');
104     info2 = regionprops(box1,'Boundingbox','MajorAxisLength','
            MinorAxisLength','Orientation');
105
106     subplot(1, 2, 2);
107     imshow(box1);
108     title('Bounding␣box␣around␣crystal');
109     hold on;
```

```
110
111     for k = 1 : length(info2)
112         BB = info2(k).BoundingBox;
113         rectangle('Position', [BB(1),BB(2),BB(3),BB(4)],'
                EdgeColor','r','LineWidth',0.1);
114     end
115
116     baseFileName = sprintf('Image␣%d.png', m);
117     fullFileName = fullfile("C:\Users\Isha Bade\OneDrive -
            Imperial College London\PhD\Experimentation\jacketed
            vessel\Multiple cleavage plane Deniz\Processed images",
            baseFileName);
118     saveas(gcf, fullFileName);
119
120     A = struct2table(info2);
121     Para = table2array(A(:,1));
122     FT = array2table(Para,'VariableNames',{'x','y','length␣b','
            length␣a'});
123     Data = [Data; FT];
124     Finaltable = Data(:,[3 4]);
125     Finaltable{:, :} = Finaltable{:, :};
126 end
```

Appendix B

Figure Permissions

Page No.	Type of work:	Name of work	Source of work	Copyright holder and contact	permission requested on	I have permission yes /no	Permission note
16	Figure	Figure 3	The role of nanopore shape in surface-induced crystallization. Nature Mater 10, 867–871 (2011).	Copyright © 2011, Springer Nature Limited Journalpermissions@springernature.com	02.10.24	yes	License granted at no charge: no. 5880801071862
16	Figure	Figure 4(b)	The role of nanopore shape in surface-induced crystallization. Nature Mater 10, 867–871 (2011).	Copyright © 2011, Springer Nature Limited Journalpermissions@springernature.com	02.10.24	yes	License granted at no charge: no. 5880801071862
16	Figure	Figure 8	Dependence of Heterogeneous Nucleation on Hydrogen Bonding Lifetime and Complementarity, Cryst. Growth Des., 18, 11, 7158–7172, (2018)	Copyright © 2018 American Chemical Society copyright@acs.org	30.09.24	yes	Permission/license granted at no charge via CCC RightsLink
16	Figure	Figure 4(d)	Toward the Rational Design of Crystalline Surfaces for Heteroepitaxy: Role of Molecular Functionality, Cryst. Growth Des., 12, 3, 1159–1166, (2012)	Copyright © 2012 American Chemical Society copyright@acs.org	30.09.24	Yes	Permission/license granted at no charge via CCC RightsLink
16	Figure	Figure 7 Only a part of the figure used	The heterogeneous nucleation of pimelic acid under the effect of a template: experimental research and molecular simulation, CrystEngComm,24, 2825-2835, (2022)	© The Royal Society of Chemistry 2022	30.09.24	Yes	Does not require permission as I am an author of a Royal Society of Chemistry (RSC) publication. Correct acknowledgement has been provided in text

18	Figure	Figure 1	Overview of Secondary Nucleation: From Fundamentals to Application, Ind. Eng. Chem. Res., 59, 41, 18335–18356, (2020)	Copyright © 2020 American Chemical Society copyright@acs.org	30.09.24	Yes	Permission/license granted at no charge via CCC RightsLink
18	Figure	Figure 4	Overview of Secondary Nucleation: From Fundamentals to Application, Ind. Eng. Chem. Res., 59, 41, 18335–18356, (2020)	Copyright © 2020 American Chemical Society copyright@acs.org	30.09.24	Yes	Permission/license granted at no charge via CCC RightsLink
18	Figure	Figure 2	Secondary Crystal Nucleation: Nuclei Breeding Factory Uncovered†. Angew. Chem. Int. Ed., 54: 14681-14684, (2015)	© 2015 Wiley-VCH Verlag GmbH & Co. KGaA, Weinheim	30.09.24	Yes	License granted at no charge: no. 5878730136787
20	Figure	Figure 2.5	Crystals and crystal growth. In Handbook of Industrial Crystallization, chapter 2, pages 32–75, (2019).	Cambridge University Press	30.09.24	Yes	License granted at no charge via PLS Clear: Ref. no. 98195
24	Figure	Figure 7(a)	Ostwald Rule of Stages–Myth or Reality?, Cryst. Growth De, 23, 6, 3958–3969, (2023)	Copyright © 2023 The Author. copyright@acs.org	30.09.24	Yes	Published by American Chemical Society. This publication is licensed under CC-BY 4.0 .
25	Figure	Figure 1	Application of Bravais-Friedel-Donnay-Harker, attachment energy and Ising models to predicting and understanding the morphology of molecular crystals, J. Phys. D: Appl. Phys. 24 89, (1991)	© 1991 IOP Publishing Ltd	30.09.24	Yes	Permission/license granted at no charge via CCC RightsLink License ID: 1531243-1
25	Figure	Figure 1	Steady State Morphologies of Paracetamol Crystal from Different Solvents, Cryst. Growth Des., 17, 2, 659–670, (2017)	Copyright © 2016 American Chemical Society copyright@acs.org	30.09.24	Yes	Permission/license granted at no charge via CCC RightsLink

28	Figure	Figure 2.14	Crystals and crystal growth. In Handbook of Industrial Crystallization, chapter 2, pages 32–75, (2019).	Cambridge University Press	30.09.24	Yes	License granted at no charge via PLS Clear: Ref. no. 98198
28	Figure	Figure 3.7(A)	On the mechanistic studies of the growth of anisotropic particles (theory and simulation), In Particle Assemblies: Synthesis, Assembly, Modeling, and Applications, chapter 3, pages 55–103. Elsevier, 1st edition, (2018)	Elsevier B.V.	30.09.24	Yes	License granted at no charge via PLS Clear: Ref. no. 98199
28	Figure	Figure 2	Modeling layered crystal growth at increasing supersaturation by connecting growth regimes. AIChE J., 63: 1338-1352, (2017)	© 2017 American Institute of Chemical Engineers	30.09.24	Yes	License granted at no charge: no. 5878771232287
35	Figure	Figure 2	Predicting mechanical properties of crystalline materials through topological analysis, CrystEngComm,20, 2698-2704, (2018)	© The Royal Society of Chemistry 2018	30.09.24	Yes	Does not require permission as I am an author of a Royal Society of Chemistry (RSC) publication. Correct acknowledgement has been provided in text
39	Figure	Figure 1	Structural basis for bending of organic crystals, Chem. Commun., 31, 3945-3947 (2005)	© The Royal Society of Chemistry 2005	04.10.24	Yes	Does not require permission as I am an author of a Royal Society of Chemistry (RSC) publication. Correct acknowledgement has been provided in text
39	Figure	Graphical abstract	Self-Healing Molecular Crystals, 55, 42, 13028-13032, (2016)	© 2016 Wiley-VCH Verlag GmbH & Co. KGaA, Weinheim	04.10.24	Yes	License granted at no charge: no. 5881981160374

39	Figure	Figure 6(c)	Self-healing ferroelastic metal–organic framework sensing guests, pressure and chemical environment, 14, 2, 4677-4684, (2021)	© The Royal Society of Chemistry 2021	04.10.24	Yes	Does not require permission as I am an author of a Royal Society of Chemistry (RSC) publication. Correct acknowledgement has been provided in text
41	Figure	Figure 2	Concerning Elusive Crystal Forms: The Case of Paracetamol, J. Am. Chem. Soc., 142, 14, 6682–6689, (2020)	Copyright © 2020 American Chemical Society copyright@acs.org	30.09.24	Yes	Permission/license granted at no charge via CCC RightsLink
41	Figure	Figure 2	Macro- and Micromorphology of Monoclinic Paracetamol Grown from Pure Aqueous Solution, J. Phys. Chem. B, 105, 38, 9057–9066, (2001)	Copyright © 2001 American Chemical Society copyright@acs.org	30.09.24	Yes	Permission/license granted at no charge via CCC RightsLink
41	Figure	Figure 3	Macro- and Micromorphology of Monoclinic Paracetamol Grown from Pure Aqueous Solution, J. Phys. Chem. B, 105, 38, 9057–9066, (2001)	Copyright © 2001 American Chemical Society copyright@acs.org	30.09.24	Yes	Permission/license granted at no charge via CCC RightsLink
56	Figure	Figure 2	Relationship between mechanical properties and crystal structure in cocrystals and salt of paracetamol. Drug Development and Industrial Pharmacy, 43(1), 89–97, (2016)	Rights managed by Taylor & Francis	30.09.24	Yes	Permission granted at no charge via CCC RightsLink

Bibliography

[1] Allan S. Myerson, Deniz Erdemir, and Alfred Y. Lee. Crystals and Crystal Growth. In *Handbook of Industrial Crystallization*, chapter 2, pages 32–75. Cambridge University Press, 3rd edition, 2019.

[2] Ying Diao, Takuya Harada, Allan S. Myerson, T. Alan Hatton, and Bernhardt L. Trout. The Role of Nanopore Shape in Surface-induced Crystallization. *Nature Materials*, 10(11):867–871, 2011.

[3] Vivek Verma, Jacek Zeglinski, Sarah Hudson, Peter Davern, and Benjamin K. Hodnett. Dependence of Heterogeneous Nucleation on Hydrogen Bonding Lifetime and Complementarity. *Crystal Growth & Design*, 18(11):7158–7172, 2018.

[4] Keith Chadwick, Jie Chen, Allan S. Myerson, and Bernhardt L. Trout. Toward the Rational Design of Crystalline Surfaces for Heteroepitaxy: Role of Molecular Functionality. *Crystal Growth & Design*, 12(3):1159–1166, 2012.

[5] Peng Yang, Ian Rosbottom, Zhonghua Li, Vivek Verma, Songgu Wu, Junbo Gong, and Jerry Y.Y. Heng. The Heterogeneous Nucleation of Pimelic Acid Under the Effect of a Template: Experimental Research and Molecular Simulation. *CrystEngComm*, 24(15):2825–2835, 2022.

[6] Shijie Xu, Yanfei Wang, Zhongbi Hou, and Xiaoyu Chuai. Overview of Secondary Nucleation: From Fundamentals to Application. *Industrial and Engineering Chemistry Research*, 59(41):18335–18356, 2020.

[7] Jamshed Anwar, Shahzeb Khan, and Lennart Lindfors. Secondary Crystal Nucleation: Nuclei Breeding Factory Uncovered. *Angewandte Chemie - International Edition*, 54(49):14681–14684, 2015.

[8] Srinivasulu Aitipamula, Rahul Banerjee, Arvind K. Bansal, Kumar Biradha, Miranda L. Cheney, Angshuman Roy Choudhury, Gautam R. Desiraju, Amol G. Dikundwar, Ritesh Dubey, Nagakiran Duggirala, Preetam P. Ghogale, Soumyajit Ghosh, Pramod Kumar Goswami, N. Rajesh Goud, Ram R. K. R. Jetti, Piotr Karpinski, Poonam Kaushik, Dinesh Kumar, Vineet Kumar, Brian Moulton, Arijit Mukherjee, Gargi Mukherjee, Allan S. Myerson, Vibha Puri, Arunachalam Ramanan, T. Rajamannar, C. Malla Reddy, Nair Rodriguez-hornedo, Robin D. Rogers, T. N. Guru Row, Palash Sanphui, Ning Shan, Ganesh Shete, Amit Singh, Changquan C. Sun, Jennifer A. Swift, Ram Thaimattam, Tejender S. Thakur, Rajesh Kumar Thaper, Sajesh P. Thomas, Srinu Tothadi, Venu R. Vangala, Narayan Variankaval, Peddy Vishweshwar, David R. Weyna, and Michael J. Zaworotko. Polymorphs, Salts, and Cocrystals: What's in a Name? *Crystal Growth & Design*, 12(5):2147–2152, 2012.

[9] Peter T. Cardew. Ostwald Rule of Stages–Myth or Reality? *Crystal Growth & Design*, 23(6):3958–3969, 2023.

[10] R. Docherty, G. Clydesdale, K. J. Roberts, and P. Bennema. Application of Bravais-Friedel-Donnay-Harker, Attachment Energy and Ising Models to Predicting and Understanding the Morphology of Molecular Crystals. *Journal of Physics D: Applied Physics*, 24(2):89–99, 1991.

[11] Jinjin Li and Michael F. Doherty. Steady State Morphologies of Paracetamol Crystal from Different Solvents. *Crystal Growth & Design*, 17(2):659–670, 2017.

[12] Matteo Salvalaglio. On the Mechanistic Studies of the Growth of Anisotropic Particles (Theory and Simulation). In Alberto Striolo Ning Wu, Daeyeon Lee, editor, *Anisotropic Particle Assemblies: Synthesis, Assembly, Modeling, and Applications*, chapter 3, pages 55–103. Elsevier, 1st edition, 2018.

[13] Carl J. Tilbury and Michael F. Doherty. Modeling Layered Crystal Growth at Increasing Supersaturation by Connecting Growth Regimes. *AIChE Journal*, 63(4):1338–1352, 2017.

[14] M. J. Bryant, A. G.P. Maloney, and R. A. Sykes. Predicting Mechanical Properties of Crystalline Materials Through Topological Analysis. *CrystEngComm*, 20(19):2698–2704, 2018.

[15] Mohammad Hossain Shariare, Frank J.J. Leusen, Marcel De Matas, Peter York, and Jamshed Anwar. Prediction of the Mechanical Behaviour of Crystalline solids. *Pharmaceutical Research*, 29(1):319–331, 2012.

[16] C. Malla Reddy, Ravi C. Gundakaram, Srinivas Basavoju, Michael T. Kirchner, K. Anantha Padmanabhan, and Gautam R. Desiraju. Structural Basis for Bending of Organic Crystals. *Chemical Communications*, 1(31):3945–3947, 2005.

[17] Patrick Commins, Hideyuki Hara, and Panče Naumov. Self-Healing Molecular Crystals. *Angewandte Chemie - International Edition*, 55(42):13028–13032, 2016.

[18] Aleksandra Pólrolniczak and Andrzej Katrusiak. Self-healing Ferroelastic Metal-organic Framework Sensing Guests, Pressure and Chemical Environment. *Materials Advances*, 2(14):4677–4684, 2021.

[19] Yumin Liu, Benjamin Gabriele, Roger J. Davey, and Aurora J. Cruz-Cabeza. Concerning Elusive Crystal Forms: The Case of Paracetamol. *Journal of the American Chemical Society*, 142(14):6682–6689, 2020.

[20] R. I. Ristic, S. Finnie, D. B. Sheen, and J. N. Sherwood. Macro- and Micromorphology of Monoclinic Paracetamol Grown from Pure Aqueous Solution. *Journal of Physical Chemistry B*, 105(38):9057–9066, 2001.

[21] Hamzah Ahmed, Manishkumar R. Shimpi, and Sitaram P. Velaga. Relationship Between Mechanical Properties and Crystal Structure in Cocrystals and Salt of Paracetamol. *Drug Development and Industrial Pharmacy*, 43(1):89–97, 2017.

[22] Roger A. Granberg and Åke C. Rasmuson. Solubility of Paracetamol in Pure Solvents. *Journal of Chemical and Engineering Data*, 44(6):1391–1395, 1999.

[23] C. Fernandes. Effect of the nature of the solvent on the crystallization of paracetamol. In *Proceedings of the 14th International Symposium on Industrial Crystallization, Cambridge, UK*. IChemE Rugby, UK, 1999.

[24] Niall A. Mitchell, Clifford T. Óciardhá, and Patrick J. Frawley. Estimation of the Growth Kinetics for the Cooling Crystallisation of Paracetamol and Ethanol Solutions. *Journal of Crystal Growth*, 328(1):39–49, 2011.

[25] ICH Guideline. Ich Q7. *International Conference on Harmonisation of Technical Requirements for Registration of Pharmaceuticals for Human Use*, 2000.

[26] MR1. At 6.4% CAGR, Active Pharmaceutical Ingredients Market Size is Projected to Exceed $284.4 Bn by 2027, Says Brandessence Market Research, 2021.

[27] MR2. Active Pharmaceutical Ingredients (API) Market- Growth, Trends, COVID-19 and Forecasts (2021 - 2026), 2020.

[28] MR3. Active Pharmaceutical Ingredient (API) Market by type (Innovative, generic), manufacturer (captive, merchant), synthesis (synthetic, biotech), by product (vaccines, Hormones), drug (OTC, Rx), application (Diabetes, oncology, CVD) - Global Forecast to 2025, 2020.

[29] Zoltan K. Nagy, M. Baker, N. Pedge, and Gerry Steele. Supersaturation and Direct Nucleation Control of an Industrial Pharmaceutical Crystallisation Process Using a Crystallisation Process Informatics System. *Proc. Int. Workshop Ind. Cryst., 18th, Sept 7–9.*, pages 101–6, 2011.

[30] Jie Chen, Bipul Sarma, James M.B. Evans, and Allan S. Myerson. Pharmaceutical Crystallization. *Crystal Growth & Design*, 11(4):887–895, 2011.

[31] Richard D. Braatz. Advanced Control of Crystallization Processes. *Annual Reviews in Control*, 26(1):87–99, 2002.

[32] Zhenguo Gao, Sohrab Rohani, Junbo Gong, and Jingkang Wang. Recent Developments in the Crystallization Process: Toward the Pharmaceutical Industry. *Engineering*, 3(3):343–353, 2017.

[33] Lian Feng Huang and Wei Qin Tong. Impact of Solid State Properties on Developability Assessment of Drug Candidates. *Advanced Drug Delivery Reviews*, 56(3):321–334, 2004.

[34] Fan Liu, Sujay D. Bagi, Qinglin Su, Rajshree Chakrabarti, Rita Barral, Janaka C. Gamekkanda, Chuntian Hu, and Salvatore Mascia. Targeting Particle Size Specification in Pharmaceutical Crystallization: A Review on Recent Process Design and Development Strategies and Particle Size Measurements. *Organic Process Research and Development*, 26(12):3190–3203, 2022.

[35] Durga Prasad Karothu, Jad Mahmoud Halabi, Ejaz Ahmed, Rodrigo Ferreira, Peter R. Spackman, Mark A. Spackman, and Panče Naumov. Global Analysis of the Mechanical Properties of Organic Crystals. *Angewandte Chemie - International Edition*, 61(10), 2022.

[36] Patrick Commins, Marieh B. Al-Handawi, Durga Prasad Karothu, Gijo Raj, and Panče Naumov. Efficiently Self-healing Boronic Ester Crystals. *Chemical Science*, 11(10):2606–2613, 2020.

[37] Ling Zhang, Jake B. Bailey, Rohit H. Subramanian, and F. Akif Tezcan. Hyperexpandable, Self-healing Macromolecular Crystals with Integrated Polymer Networks. *Nature*, 557(7703):86–91, 2018.

[38] Poonam Gupta, Sumair A. Rather, Binoy K. Saha, Tamas Panda, Durga Prasad Karothu, and Naba K. Nath. Mechanical Flexibility of Molecular Crystals Achieved by Exchanging Hydrogen Bonding Synthons. *Crystal Growth & Design*, 20(5):2847–2852, 2020.

[39] Gerrit Vreeman, Chenguang Wang, C. Malla Reddy, and Changquan Calvin Sun. Exceptional Powder Tabletability of Elastically Flexible Crystals. *Crystal Growth & Design*, 21(12), 2021.

[40] Jerry Y.Y. Heng, Alexander Bismarck, and Daryl R. Williams. Anisotropic Surface Chemistry of Crystalline Pharmaceutical solids. *AAPS PharmSciTech*, 7(4), 2006.

[41] H.J.M. Kramer and G.M. van Rosmalen. Crystallization. In *Encylopedia of Separation Science*, pages 64–84. Academic Press, 1st edition, 2000.

[42] C. Price. Take Some Solid Steps to Improve Crystallization. *Chemical Engineering Progress*, 93(9):34–43, 1997.

[43] Pieter Vonk. Industrial Aspects of Crystallization. In Henk G. Merkus and Gabriel M.H. Meesters, editors, *Production, Handling and Characterization of Particulate Materials*, pages 31–71. Springer, Cham, 2016.

[44] K. J. Carpenter and W. M.L. Wood. Industrial Crystallization for Fine Chemicals. *Advanced Powder Technology*, 15(6):657–672, 2004.

[45] Lars Vicum, Marco Mazzotti, and Martin Iggland. *Precipitation and Crystallization of Pigments*. Cambridge University Press, 3rd edition, 2019.

[46] Seong-Hoon Jeong, Yu-Seok Youn, Beom-Soo Shin, and Eun-Seok Park. Drug Polymorphism and its Importance on Drug Development Process. *Journal of Pharmaceutical Investigation*, 40(special issue):9–17, 2010.

[47] Stephen R Byrn, Ralph R Pfeiffer, and Joseph G Stowell. *Solid-state Chemistry of Drugs*. SSCI, Inc., West Lafayette, Ind. SE - xvii, 574 pages : illustrations ; 24 cm, 2nd ed edition, 1999.

[48] J.W. Mullin. The Crystalline State. In *Crystallization*, chapter 1, pages 1–27. Butterworth Heinemann, 4th edition, 2001.

[49] Michael A. Lovette, Andrea Robben Browning, Derek W. Griffin, Jacob P. Sizemore, Ryan C. Snyder, and Michael F. Doherty. Crystal Shape Engineering. *Industrial and Engineering Chemistry Research*, 47(24):9812–9833, 2008.

[50] W. Ostwald. Studien über die Bildung und Umwandlung fester Körper. *Zeitschrift für Physikalische Chemie*, 22:289–330, 1897.

[51] Florence Isaac Henry ALexander Miers. The Refractive Indices of Crystallising Solutions, with Especial Reference to the Passage from the Metastable to the Labile Condition. *The Journal of the Chemical Society, Transactions*, 89:413–454, 1906.

[52] Experiments Salol. The Spontaneous Crystallisation of Binary Mixtures.— Experiments on Salol and Betol. *Proceedings of the Royal Society of London. Series A, Containing Papers of a Mathematical and Physical Character*, 79(531):322–351, 1907.

[53] Wojciech Bogacz and Janusz Wójcik. The Metastable Zone of Aqueous Solutions. *CHEMIX*, 68(3):198–201, 2014.

[54] Joachim Ulrich and Christine Strege. Some Aspects of the Importance of Metastable Zone Width and Nucleation in Industrial Crystallizers. *Journal of Crystal Growth*, 237-239(part III):2130–2135, 2002.

[55] A. Mersmann and K. Bartosch. How to Predict the Metastable Zone Width. *Journal of Crystal Growth*, 183(1-2):240–250, 1998.

[56] Jennifer Moffitt Schall and Allan S. Myerson. *Solutions and Solution properties*. Cambridge University Press, 3rd edition, 2019.

[57] O.Loisnard F. Baillon, F. Espitalier, C. Cogne, R. Peczalski. Crystallization and Freezing Processes Assisted by Power Ultrasound. In *Power Ultrasonics - Applications of High-Intensity Ultrasound*, pages 845–874. Woodhead Publishing, 2015.

[58] Huaiyu Yang and Alastair J. Florence. Relating Induction Time and Metastable Zone Width. *CrystEngComm*, 19(28):3966–3978, 2017.

[59] J.W. Mullin. Nucleation. In *Crystallization*, chapter 5, pages 181–214. Butterworth Heinemann, 4th edition, 2001.

[60] Deniz Erdemir, Alfred Y. Lee, and Allan S. Myerson. Crystal Nucleation. In *Handbook of Industrial Crystallization*, chapter 3, pages 76–114. Cambridge University Press, 3rd edition, 2016.

[61] Denette Murphy and Nair Rodriguez-Hornedo. Significance of Controlling Crystallization Mechanisms and Kinetics in. *Journal of Pharmaceutical Sciences*, 88(7):651–660, 1999.

[62] Wolfgang Beckmann. Mechanisms of crystallization. In *Crystallization*, chapter 2, pages 7–33. John Wiley & Sons, Ltd, 2013.

[63] J.W. Mullin. Solutions and Solubility. In *Crystallization*, chapter 3, pages 86–132. Butterworth Heinemann, 4th edition, 2001.

[64] Martin Iggland and Marco Mazzotti. Population Balance Modeling with Size-dependent Solubility: Ostwald Ripening. *Crystal Growth & Design*, 12(3):1489–1500, 2012.

[65] Yongfan Yang, Ling Zhou, Xia Zhang, Wenchao Yang, Shihao Zhang, Lixuan Xiong, Yu Wei, Meijin Zhang, Baohong Hou, and Qiuxiang Yin. Influence of Solvent Properties and Intermolecular Interaction Between Solute and Solvent on Nucleation Kinetics of HMBTAD. *Journal of Crystal Growth*, 498:77–84, 2018.

[66] J. Cookman, V. Hamilton, S. R. Hall, and U. Bangert. Non-classical crystallisation pathway directly observed for a pharmaceutical crystal via liquid phase electron microscopy. *Scientific Reports*, 10(1):1–10, 2020.

[67] Oleg Galkin, Kai Chen, Ronald L. Nagel, Rhoda Elison Hirsch, and Peter G. Vekilov. Liquid-liquid Separation in Solutions of Normal and Sickle Cell Hemoglobin. *Proceedings of the National Academy of Sciences of the United States of America*, 99(13):8479–8483, 2002.

[68] Denis Gebauer and Helmut Cölfen. Prenucleation clusters and non-classical nucleation. *Nano Today*, 6(6):564–584, 2011.

[69] Ramya Muthusamy, Nandhu varshini Gnanasekar, and Srinivasan Karuppannan. Nucleation Control and Isolation of Polymorphic Forms of Aspirin through an Efficient Template-Assisted Swift Cooling Process. *Crystal Research and Technology*, 59(8):1–14, 2024.

[70] Umang V. Shah, Christian Amberg, Ying Diao, Zhongqiang Yang, and Jerry Y.Y. Heng. Heterogeneous Nucleants for Crystallogenesis and Bioseparation. *Current Opinion in Chemical Engineering*, 8:69–75, 2015.

[71] Jose V. Parambil, Sendhil K. Poornachary, Jerry Y.Y. Heng, and Reginald B.H. Tan. Template-induced Nucleation for Controlling Crystal Polymorphism: From Molecular Mechanisms to Applications in Pharmaceutical Processing. *CrystEngComm*, 21(28):4122–4135, 2019.

[72] C. A. Mitchell, L. Yu, and M. D. Ward. Selective Nucleation and Discovery of Organic Polymorphs Through Epitaxy with Single Crystal Substrates. *Journal of the American Chemical Society*, 123(44):10830–10839, 2001.

[73] Stan F.S.P. Looijmans, Dario Cavallo, Lian Yu, and Gerrit W.M. Peters. Cross-Nucleation between Polymorphs: Quantitative Modeling of Kinetics and Morphology. *Crystal Growth & Design*, 18(7):3921–3926, 2018.

[74] Eun Hee Lee, Stephan X M Boerrigter, and Stephen R Byrn. Epitaxy of a Structurally Related Compound on the (100) Faces of Flufenamic Acid Form I and III Single Crystals. *Crystal Growth & Design*, 10(2):518–527, 2010.

[75] Dario Cavallo, Francesca Galli, Lian Yu, and Giovanni C. Alfonso. Cross-Nucleation between Concomitantly Crystallizing α- And γ-Phases in Polypivalolactone: Secondary Nucleation of One Polymorph on Another. *Crystal Growth & Design*, 17(5):2639–2645, 2017.

[76] David H. Case, Vijay K. Srirambhatla, Rui Guo, Rona E. Watson, Louise S. Price, Hector Polyzois, Jeremy K. Cockcroft, Alastair J. Florence, Derek A. Tocher, and Sarah L. Price. Successful Computationally Directed Templating of Metastable Pharmaceutical Polymorphs. *Crystal Growth & Design*, 18(9):5322–5331, 2018.

[77] Rupa Hiremath, Joseph A. Basile, Stephen W. Varney, and Jennifer A. Swift. Controlling Molecular Crystal Polymorphism with Self-assembled Monolayer Templates. *Journal of the American Chemical Society*, 127(51):18321–18327, 2005.

[78] Ana Kwokal, Thai T H Nguyen, and Kevin J Roberts. Polymorph-Directing Seeding of Entacapone Crystallization in Aqueous/Acetone Solution Using a Self-Assembled Molecular Layer on Au (100). *Crystal Growth & Design*, 9(10):4324–4334, 2009.

[79] Phillip W. Carter and Michael D. Ward. Topographically Directed Nucleation of Organic Crystals on Molecular Single-Crystal Substrates. *Journal of the American Chemical Society*, 115(24):11521–11535, 1993.

[80] Pierre-Andre Cazade, Vivek Verma, Benjamin K Hodnett, and Damien Thompson. Extended Lifetime of Molecules Adsorbed onto Excipients Drives Nucleation in Heterogeneous Crystallization. *Crystal Growth & Design*, 21(4):2101–2112, 2021.

[81] Jeong Myeong Ha, Johanna H. Wolf, Marc A. Hillmyer, and Michael D. Ward. Polymorph Selectivity under Nanoscopic Confinement. *Journal of the American Chemical Society*, 126(11):3382–3383, 2004.

[82] Antonella Caridi, Samir A. Kulkarni, Gianluca Di Profio, Efrem Curcio, and Joop H. Ter Horst. Template-induced Nucleation of Isonicotinamide Polymorphs. *Crystal Growth & Design*, 14(3):1135–1141, 2014.

[83] Vivek Verma, Hamish Mitchell, Ethan Errington, Mingxia Guo, and Jerry Y.Y. Heng. Templated Crystallization of Glycine Homopeptides: Experimental and Computational Developments. *Chemical Engineering and Technology*, 46(6):1271–1278, 2023.

[84] René R.E. Steendam and Patrick J. Frawley. Secondary Nucleation of Sodium Chlorate: The Role of Initial Breeding. *Crystal Growth & Design*, 19(6):3453–3460, 2019.

[85] John Garside and Roger J. Davey. Secondary Contact Nucleation: Kinetics, Growth and Scale-up. *Chemical Engineering Communications*, 4(4-5):393–424, 1980.

[86] S. G. Agrawal and A. H.J. Paterson. Invited Review Secondary Nucleation: Mechanisms and Models. *Chemical Engineering Communications*, 202(5):698–706, 2015.

[87] Norvin A Clontz. Contact nucleation of magnesium sulfate heptahydrate. In *Chem. Eng. Progr. Symp. Ser.*, volume 67, pages 6–17, 1971.

[88] Luca Bosetti and Marco Mazzotti. Study of Secondary Nucleation by Attrition of Potassium Alum Crystals Suspended in Different Solvents. *Crystal Growth & Design*, 20(4):2570–2577, 2020.

[89] Alan D. Randolph and Maurice A. Larson. *Theory of Particulate Processes*. Academic Press Inc., 1971.

[90] Ru Ying Qian and Gregory D. Botsaris. A New Mechanism for Nuclei Formation in Suspension Crystallizers: The Role of Interparticle Forces. *Chemical Engineering Science*, 52(20):3429–3440, 1997.

[91] Dejiang Zhang, Xinyi Wang, Joachim Ulrich, Weiwei Tang, Shijie Xu, Zhonghua Li, Sohrab Rohani, and Junbo Gong. Control of Crystal Properties in a Mixed-Suspension Mixed-Product Removal Crystallizer: General Methods and the Effects of Secondary Nucleation. *Crystal Growth & Design*, 19(5):3070–3084, 2019.

[92] Mustafa Yousuf and Patrick J. Frawley. Experimental Evaluation of Fluid Shear Stress Impact on Secondary Nucleation in a Solution Crystallization of Paracetamol. *Crystal Growth & Design*, 18(11):6843–6852, 2018.

[93] Andrew Cashmore, Konstantinos Georgoulas, Christopher Boyle, Mei Lee, Mark D. Haw, and Jan Sefcik. Published as part of Crystal Growth & Design virtual special

issue “Industrial Crystallization: ISIC 22/BACG 52”. *Crystal Growth & Design*, 2024.

[94] Reinhard Ploß and Alfons Mersmann. A new model of the effect of stirring intensity on the rate of secondary nucleation. *Chemical Engineering & Technology*, 12(1):137–146, 1989.

[95] E P K Ottens and E. J. De Jong. A Model for Secondary Nucleationin a Stirred Vessel Cooling Crystallizer. *Kristall and Technik*, 9(8):873–886, 1974.

[96] Patrick J. Frawley, Niall A. Mitchell, Clifford T. Ó'Ciardhá, and Kieran W. Hutton. The Effects of Supersaturation, Temperature, Agitation and Seed Surface Area on the Secondary Nucleation of Paracetamol in Ethanol Solutions. *Chemical Engineering Science*, 75:183–197, 2012.

[97] Kevin J. Roberts, Robert Docherty, and Rui Tamura. *Engineering Crystallography: From Molecule to Crystal to Functional Form*. Springer, 2017.

[98] C. Hoff M. Kohl, G. Fevotte, J.-P. Klein, O. Monnier. Proceedings of the 4th International Workshop on CGOM (Special Event of the 6th BIWIC). In *Bremen, Martin-Luther-University Halle-Wittenberg, Halle (Saale)*, pages 175–181, 1997.

[99] Terence L. Threlfall and Simon J. Coles. A Perspective on the Growth-only Zone, the Secondary Nucleation Threshold and Crystal Size Distribution in Solution Crystallisation. *CrystEngComm*, 18(3):369–378, 2016.

[100] Maria L. Briuglia, Jan Sefcik, and Joop H. Horst. Measuring Secondary Nucleation through Single Crystal Seeding. *Crystal Growth & Design*, 2019.

[101] Vasuki Ramachandran, Peter J. Halfpenny, and Kevin J. Roberts. Crystal Science Fundamentals. In Kevin J. Roberts, Robert Docherty, and Rui Tamura, editors, *Engineering Crystallography: From Molecule to Crystal to Functional Form*, chapter 1, pages 3–21. Springer, 1st edition, 2017.

[102] B.D. Cullity and S.R. Stock. *Elements of X-Ray Diffraction*. Prentice-Hall, 3rd edition, 2001.

[103] E. Michalski. On the New Characteristics of Miller Indices for Centered Lattices. *Bulletin of the Polish Academy of Sciences: Technical Sciences*, 66(4):529–538, 2018.

[104] G. Patrick Stahly. Diversity in Single- and Multiple-Component Crystals. The Search for and Prevalence of Polymorphs and Cocrystals. *Crystal Growth & Design*, 7(6):1007–1026, 2007.

[105] Jonathan W. Steed. The Role of Co-crystals in Pharmaceutical Design. *Trends in Pharmacological Sciences*, 34(3):185–193, 2013.

[106] Jonathan C. Burley, Melinda J. Duer, Robin S. Stein, and Ranko M. Vrcelj. Enforcing Ostwald's Rule of Stages: Isolation of Paracetamol Forms III and II. *European Journal of Pharmaceutical Sciences*, 31(5):271–276, 2007.

[107] Narayan Variankaval and Aaron S. Cote. From Form to Function: Crystallization of Active Pharmaceutical Ingredients. *AIChE Journal*, 54(7):1682–1688, 2008.

[108] Kevin P. Guiry, Joanne M. Kelleher, Simon E. Lawrence, Marie T. McAuliffe, Humphrey A. Moynihan, and Andrea L. Ryan. Crystal Polymorphism of Pharmaceuticals: Probing Crystal Nucleation at the Molecular Level. *Journal of Enzyme Inhibition and Medicinal Chemistry*, 22(5):550–555, 2007.

[109] J. Bauer, S. Spanton, R. Henry, J. Quick, W. Dziki, W. Porter, and J. Morris. Ritonavir: An Extraordinary Example of Conformational Polymorphism. *Pharmaceutical Research*, 18(6):859–866, 2001.

[110] Eun Hee Lee. A Practical Guide to Pharmaceutical Polymorph Screening & Selection. *Asian Journal of Pharmaceutical Sciences*, 9(4):163–175, 2014.

[111] Jaroslav Nývlt. The Ostwald Rule of Stages. *Crystal Research and Technology*, 30(4):443–449, 1995.

[112] G. T. Rengarajan, D. Enke, M. Steinhart, and M. Beiner. Size-dependent Growth of Polymorphs in Nanopores and Ostwald's Step Rule of Stages. *Physical Chemistry Chemical Physics*, 13(48):21367–21374, 2011.

[113] Mailavaram Raghu Prasad, Pran Kishore Deb, Balakumar Chandrasekaran, Rahul Maheshwari, and Rakesh K. Tekade. Chapter 3 - basics of crystallization process applied in drug exploration. In Rakesh K. Tekade, editor, *Dosage Form Design Parameters*, Advances in Pharmaceutical Product Development and Research, pages 67–103. Academic Press, 2018.

[114] D.D. Le Pevelen. 8.4 physical separations: Solid-state forms and habits of chiral substances. In Erick M. Carreira and Hisashi Yamamoto, editors, *Comprehensive Chirality*, pages 54–62. Elsevier, Amsterdam, 2012.

[115] Josiah Willard Gibbs. *Scientific papers of J. Willard Gibbs, in two volumes*, volume 1. Longmans, Green, 1906.

[116] Rongjin Li, Xiaotao Zhang, Huanli Dong, Qikai Li, Zhigang Shuai, and Wenping Hu. Gibbs-Curie-Wulff Theorem in Organic Materials: A Case Study on the Relationship between Surface Energy and Crystal Growth. *Advanced Materials*, 28(8):1697–1702, 2016.

[117] G. Wulff. Xxv. zur frage der geschwindigkeit des wachsthums und der auflösung der krystallflächen. *Zeitschrift für Kristallographie - Crystalline Materials*, 34(1-6):449–530, 1901.

[118] David S. Coombes, C. Richard A Catlow, Julian D. Gale, Martin J. Hardy, and Martin R. Saunders. Theoretical and Experimental Investigations on the Morphology of Pharmaceutical Crystals. *Journal of Pharmaceutical Sciences*, 91(7):1652–1658, 2002.

[119] AA Chernov. The kinetics of the growth forms of crystals. *Sov. Phys. Crystallogr*, 7:728–730, 1963.

[120] F. C. Frank. On the kinematic theory of crystal growth and dissolution processes, ii. *Zeitschrift für Physikalische Chemie*, 77(1-6):84–92, 1972.

[121] J. D. H. Donnay and D. Harker. A New Law of Crystal Morphology Extending the Law of Bravais. *Am. Mineral.*, 22:446, 1937.

[122] P. Hartman and W. G. Perdok. On the Relations Between Structure and Morphology of Crystals. I. *Acta Crystallographica*, 8(1):49–52, 1955.

[123] P. Hartman. The Attachment Energy as a Habit Controlling Factor. III. Application to Corundum. *Journal of Crystal Growth*, 49(1):166–170, 1980.

[124] Keith Chadwick, Jie Chen, Erik E. Santiso, and Bernhardt L. Trout. Molecular Modeling Applications in Crystallization. In *Handbook of Industrial Crystallization*, chapter 5, pages 136–171. Cambridge University Press, 3rd edition, 2019.

[125] Gang Chen, Chunyu Chen, Mingzhu Xia, Wu Lei, Fengyun Wang, and Xuedong Gong. A Study of the Solvent Effect on the Crystal Morphology of Hexogen by Means of Molecular Dynamics Simulations. *RSC Advances*, 5(32):25581–25589, 2015.

[126] Dan Zhu, Shihao Zhang, Pingping Cui, Chang Wang, Jiayu Dai, Ling Zhou, Yaohui Huang, Baohong Hou, Hongxun Hao, Lina Zhou, and Qiuxiang Yin. Solvent Effects on Catechol Crystal Habits and Aspect Ratios: A Combination of Experiments and Molecular Dynamics Simulation Study. *Crystals*, 10(4), 2020.

[127] Matteo Salvalaglio, Thomas Vetter, Federico Giberti, Marco Mazzotti, and Michele Parrinello. Uncovering Molecular Details of Urea Crystal Growth in the Presenceof Additives. *J. Am. Chem. Soc.*, 134:17221–17233, 2012.

[128] Stefano Piana, Manijeh Reyhani, and Julian D. Gale. Simulating Micrometre-scale Crystal Growth from Solution. *Nature*, 438(7064):70–73, 2005.

[129] Marco De La Pierre, Paolo Raiteri, and Julian D. Gale. Structure and Dynamics of Water at Step Edges on the Calcite 1014 Surface. *Crystal Growth & Design*, 16(10):5907–5914, 2016.

[130] T. Kuroda. Growth of a Crystal Surface with Non-uniformity in Supersaturation Due to Laminar Flow of Solution Along the Surface. *Journal of Crystal Growth*, 71(1):84–94, 1985.

[131] William R. Wilcox. Transport Phenomena in Crystal Growth from Solution. *Progress in Crystal Growth and Characterization of Materials*, 26(C):153–194, 1993.

[132] W. K. Burton, N. Cabrera, and F.C. Frank. The Growth of Crystals and the Equilibrium Structure of Their Surfaces. *Philosophical Transactions of the Royal Society of London. Series A, Mathematical and Physical Sciences*, 243(866):299–358, 1951.

[133] T. T.H. Nguyen, R. B. Hammond, K. J. Roberts, I. Marziano, and G. Nichols. Precision Measurement of the Growth Rate and Mechanism of Ibuprofen 001 and 011 as a Function of Crystallization Environment. *CrystEngComm*, 16(21):4568–4586, 2014.

[134] F. C. Frank. The Influence of Dislocations on Crystal Growth. *Discussions of the Faraday Society*, 5(48):48–54, 1949.

[135] Ryan C. Snyder and Michael F. Doherty. Predicting Crystal Growth by Spiral Motion. *Proceedings of the Royal Society A: Mathematical, Physical and Engineering Sciences*, 465(2104):1145–1171, 2009.

[136] R. Davey, W. Fila, and J. Garside. The Influence of Biuret on the Growth Kinetics of Urea Crystals from Aqueous Solutions. *Journal of Crystal Growth*, 79(1-3 PART 2):607–613, 1986.

[137] A. Markande, A. Nezzal, J. J. Fitzpatrick, and L. Aerts. Investigation of the Crystallization Kinetics of Dextrose Monohydrate Using In Situ Particle Size and

Supersaturation Monitoring. *Particulate Science and Technology*, 27(4):373–388, 2009.

[138] L. Derdour, C. Sivakumar, D. Skliar, S. K. Pack, C. J. Lai, J. P. Vernille, and S. Kiang. Crystallization from Solutions Containing Multiple Conformers. 2. Experimental Study and Model Validation. *Crystal Growth & Design*, 12(11):5188–5196, 2012.

[139] S. D. Finnie, R. I. Ristic, J. N. Sherwood, and A. M. Zikic. Morphological and Growth Rate Distributions of Small Self-nucleated Paracetamol Crystals Grown from Pure Aqueous Solutions. *Journal of Crystal Growth*, 207(4):308–318, 1999.

[140] Caroline A. Offiler, Aurora J. Cruz-Cabeza, Roger J. Davey, and Thomas Vetter. Crystal Growth Cell Incorporating Automated Image Analysis Enabling Measurement of Facet Specific Crystal Growth Rates. *Crystal Growth & Design*, 22(5):2837–2848, 2022.

[141] Thai Thu Hien Nguyen, Thomas D. Turner, Andrea M.E. Matinong, Ivan Marziano, Robert B. Hammond, and Kevin J. Roberts. Measured Growth Rates of Ibuprofen: Comparing Single Crystal and Bulk Suspensions Data. *Chemical Engineering and Technology*, 44(7):1287–1293, 2021.

[142] W. Omar, S. Al-Sayed, A. Sultan, and J. Ulrich. Growth Rate of Single Acetaminophen Crystals in Supersaturated Aqueous Solution Under Different Operating Conditions. *Crystal Research and Technology*, 43(1):22–27, 2008.

[143] Rodrigo Soto, Vivek Verma, Aisling Lynch, Benjamin K. Hodnett, and Åke C. Rasmuson. Crystal Growth Kinetics of Pharmaceutical Compounds. *Crystal Growth & Design*, 20(12):7626–7639, 2020.

[144] Lynch Aisling and Rasmuson Åke. Crystal Growth of Single Salicylamide Crystals. *Crystal Growth & Design*, 19(12):7230–7239, 2019.

[145] Patrícia Cruz, Fernando Rocha, and António Ferreira. Crystallization of Paracetamol from Mixtures of Ethanol and Water in a Planar Oscillatory Flow Crystallizer:

Effect of the Oscillation Conditions on the Crystal Growth Kinetics. *CrystEngComm*, 23(47):8301–8314, 2021.

[146] M. K. Singh and Arup Banerjee. Role of Solvent and External Growth Environments to Determine Growth Morphology of Molecular Crystals. *Crystal Growth & Design*, 13(6):2413–2425, 2013.

[147] Liang Song, Feng Qi Zhao, Si Yu Xu, Xue Hai Ju, and Cai Chao Ye. Crystal Morphology Prediction and Anisotropic Evolution of 1,1-Diamino-2,2-dinitroethylene (FOX-7) by Temperature Tuning. *Scientific Reports nature research*, 10(1):1–9, 2020.

[148] I. Rosbottom, C. Y. Ma, T. D. Turner, R. A. O'Connell, J. Loughrey, G. Sadiq, R. J. Davey, and K. J. Roberts. Influence of Solvent Composition on the Crystal Morphology and Structure of p-Aminobenzoic Acid Crystallized from Mixed Ethanol and Nitromethane Solutions. *Crystal Growth & Design*, 17(8):4151–4161, 2017.

[149] J. H. Ter Horst, R. M. Geertman, and G. M. Van Rosmalen. The Effect of Solvent on Crystal Morphology. *Journal of Crystal Growth*, 230(1-2):277–284, 2001.

[150] Qiaoqiao Liu, Guihong Lin, Jian Zhou, Liangliang Huang, and Chang Liu. Hydrogen-bond Mediated and Concentrate-dependent NaHCO3 Crystal Morphology in NaHCO3–Na2CO3 Aqueous Solution: Experiments and Computer Simulations. *Chinese Journal of Chemical Engineering*, 55:49–58, 2023.

[151] Hang Chen, Shaojun Duan, Yuzhu Sun, Xingfu Song, and Jianguo Yu. Molecular Dynamics Simulations of Solvent Effects on the Crystal Morphology of Lithium Carbonate. *RSC Advances*, 10(10):5604–5609, 2020.

[152] Liangcheng Song, Sheng Lv, Huai Guo, Yingbei Cui, Xiao Zhang, Shuguang Zhang, Yu Tian, and Chunhui Yang. Crystal Morphology Regulation of Pronamide Through Solvent Selection: Prediction and Implementation. *Journal of Chemical Thermodynamics*, 169(January), 2022.

[153] Maaya Omori and Kiyohiko Sugano. Solution-Mediated Phase Transformation on Crystal Facets of Carbamazepine-Saccharin Cocrystals. *Crystal Growth & Design*, 21(11):6237–6244, 2021.

[154] Li Zhao, Jing Li, Jinxuan He, Peicheng Luo, Liangwei Shi, Junhong Zhou, and Aimin Pang. A study of Solvent and Antisolvent Influence on the Crystal Morphology of ϵ-CL-20 by a Modified Attachment Energy Model. *Propellants, Explosives, Pyrotechnics*, 45(7):1117–1128, 2020.

[155] Aisling Lynch, Vivek Verma, Jacek Zeglinski, Pauric Bannigan, and Åke Rasmuson. Face Indexing and Shape Analysis of Salicylamide Crystals Grown in Different Solvents. *CrystEngComm*, 21(16):2648–2659, 2019.

[156] Jie Chen and Bernhardt L. Trout. Computer-aided Solvent Selection for Improving the Morphology of Needle-like Crystals: A Case Study of 2,6-dihydroxybenzoic Acid. *Crystal Growth & Design*, 10(10):4379–4388, 2010.

[157] C. Sudha and K. Srinivasan. Understanding the Effect of Solvent Polarity on the Habit Modification of Monoclinic Paracetamol in Terms of Molecular Recognition at the Solvent Crystal/Interface. *Crystal Research and Technology*, 49(11):865–872, 2014.

[158] R. J. Davey. The Effect of Impurity Adsorption on the Kinetics of Crystal Growth from Solution. *Journal of Crystal Growth*, 34(1):109–119, jun 1976.

[159] Yasushi Yoshioka, Takashi Matsui, Masanobu Kasuga, and Toshiharu Irisawa. Effects of Impurities on Lateral Growth of Crystals. *Journal of Crystal Growth*, 198-199(PART I):71–76, 1999.

[160] K. Sangwal. Effect of Impurities on the Processes of Crystal Growth. *Journal of Crystal Growth*, 128(1-4 PART 2):1236–1244, 1993.

[161] N. Cabrera and D.A. Vermilyea. Growth and Perfection of Crystals. In R. H. Doremus, B. W. Roberts, and D. Turnbull, editors, *International Conference on Crystal Growth*, page 393, New York, 1958. John Wiley & Sons.

[162] James F. Lutsko, Nélido González-Segredo, Miguel A. Durán-Olivencia, Dominique Maes, Alexander E.S. Van Driessche, and Mike Sleutel. Crystal Growth Cessation Revisited: The Physical Basis of Step Pinning. *Crystal Growth & Design*, 14(11):6129–6134, nov 2014.

[163] James P. Lee-Thorp, Alexander G. Shtukenberg, and Robert V. Kohn. Crystal Growth Inhibition by Mobile Randomly Distributed Stoppers. *Crystal Growth & Design*, 20(3):1940–1950, 2020.

[164] Edward N. Constance, Muzaffer Mohammed, Adeolu Mojibola, Micah Egiefameh, Oluseyi Daodu, Travis Clement, Taiwo Ogundolie, Chinenye Nwawulu, and Kadir Aslan. Effect of Additives on the Crystal Morphology of Amino Acids: A Theoretical and Experimental study. *J. Phys. Chem. C*, 120(27):14749–14757, 2016.

[165] Korlakunte V R Prasad, Radoljub I Ristic, David B Sheen, and John N Sherwood. Crystallization of Paracetamol from Solution in the Presence and Absence of Impurity. *Int. J. Pharm.*, 215(1):29–44, 2001.

[166] Govindhan Dhanaraj, Kullaiah Byrappa, Vishwanath (Vish) Prasad, and Michael Dudley. Crystal Growth Techniques and Characterization: An Overview. In *Handbook of Crystal Growth*, chapter 1, pages 3–15. Springer, 2010.

[167] R. J. Roberts, R. C. Rowe, and P. York. The Relationship Between Indentation Hardness of Organic Solids and Their Molecular Structure. *Journal of Materials Science*, 29(9):2289–2296, 1994.

[168] Changquan Sun and David J.W. Grant. Improved Tableting Properties of p-Hydroxybenzoic Acid by Water of Crystallization: A Molecular Insight. *Pharmaceutical Research*, 21(2):382–386, 2004.

[169] J. Wijnen, R. H.J. Peerlings, J. P.M. Hoefnagels, and M. G.D. Geers. A Discrete Slip Plane Model for Simulating Heterogeneous Plastic Deformation in Single Crystals. *International Journal of Solids and Structures*, 228:111094, 2021.

[170] Lawrence E. Murr. Volume Defects: 3D Imperfections in Crystals Contents. In *Handbook of Materials Structures, Properties, Processing and Performance*, pages 313–324. Springer International Publishing, 2015.

[171] CHANGQUAN CALVIN SUN and Y.-H. KIANG. On the Identification of Slip Planes in Organic Crystals Based on Attachment Energy Calculation. *Journal of Pharmaceutical Sciences*, 97(8):3456–3461, 2007.

[172] H.M. Hulburt and S. Katz. Some Problems in Particle Technology. *Chemical Engineering Science*, 19(8):555–574, 1964.

[173] Zoltan K. Nagy and Richard D. Braatz. Advances and New Directions in Crystallization Control. *Annual Review of Chemical and Biomolecular Engineering*, 3:55–75, 2012.

[174] Yongchun Zhang and Michael F. Doherty. Simultaneous Prediction of Crystal Shape and Size for Solution Crystallization. *AIChE Journal*, 50(9):2101–2112, 2004.

[175] Zoltan K. Nagy, Gilles Fevotte, Herman Kramer, and Levente L. Simon. Recent advances in the monitoring, modelling and control of crystallization systems. *Chemical Engineering Research and Design*, 91(10):1903–1922, 2013.

[176] Boris Y. Shekunov, Pratibhash Chattopadhyay, Henry H.Y. Tong, and Albert H.L. Chow. Particle Size Analysis in Pharmaceutics: Principles, Methods and Applications. *Pharmaceutical Research*, 24(2):203–227, 2007.

[177] C. Gahn and A. Mersmann. Brittle Fracture in Crystallization Processes Part A. Attrition and Abrasion of Brittle Solids. *Chemical Engineering Science*, 54(9):1273–1282, 1999.

[178] C. Gahn and A. Mersmann. Brittle Fracture in Crystallization Processes Part B. Growth of Fragments and Scale-up of Suspension Crystallisers. *Chemical Engineering Science*, 54(9):1283–1292, 1999.

[179] Luca Bosetti and Marco Mazzotti. Population Balance Modeling of Growth and Secondary Nucleation by Attrition and Ripening. *Crystal Growth & Design*, 20(1):307–319, 2020.

[180] Rory Tyrrell and Patrick Frawley. Single Crystal Fragmentation: Visualizing Breakage Model Performance for Pharmaceutical Processes. *Wear*, 414-415(March):275–288, 2018.

[181] Sagar B. Gadewar and Michael F. Doherty. A Dynamic Model for Evolution of Crystal Shape. *Journal of Crystal Growth*, 267(1-2):239–250, 2004.

[182] S. A. Schiele, T. Haider, and H. Briesen. Growth of broken crystals tracked in 4D using X-ray computed tomography and its influence on impurity incorporation. *Scientific Reports*, 14(1):1–14, 2024.

[183] Cai Y. Ma and Kevin J. Roberts. Morphological population balance modelling of the effect of crystallisation environment on the evolution of crystal size and shape of para-aminobenzoic acid. *Computers and Chemical Engineering*, 126:356–370, 2019.

[184] H. Li and Bing Shiou Yang. Model evaluation of particle breakage facilitated process intensification for Mixed-Suspension-Mixed-Product-Removal (MSMPR) crystallization. *Chemical Engineering Science*, 207:1175–1186, 2019.

[185] Panče Naumov, Stanislav Chizhik, Manas K. Panda, Naba K. Nath, and Elena Boldyreva. Mechanically Responsive Molecular Crystals. *Chemical Reviews*, 115(22):12440–12490, 2015.

[186] Panče Naumov, Durga Prasad Karothu, Ejaz Ahmed, Luca Catalano, Patrick Commins, Jad Mahmoud Halabi, Marieh B. Al-Handawi, and Liang Li. The Rise of the Dynamic Crystals. *Journal of the American Chemical Society*, 142(31):13256–13272, 2020.

[187] Ejaz Ahmed, Durga Prasad Karothu, Mark Warren, and Panče Naumov. Shape-memory Effects in Molecular Crystals. *Nature Communications*, 10(1), 2019.

[188] Surojit Bhunia, Shubham Chandel, Sumanta Kumar Karan, Somnath Dey, Akash Tiwari, Susobhan Das, Nishkarsh Kumar, Rituparno Chowdhury, Saikat Mondal, Ishita Ghosh, Amit Mondal, Bhanu Bhusan Khatua, Nirmalya Ghosh, and C. Malla Reddy. Autonomous Self-repair in Piezoelectric Molecular Crystals. *Science*, 373(6552):321–327, 2021.

[189] & PančeNaumov Marieh B. Al-Handawi, Patrick Commins, Ahmed S. Dalaq, Pedro A. Santos-Florez, Srujana Polavaram, Pascal Didier, Durga Prasad Karothu, Qiang Zhu, Mohammed Daqaq, Liang Li. Ferroelastic Ionic Organic Crystals that Self-heal to 95 *Nature Communications*, 15:1–10, 2024.

[190] C. Malla Reddy, K. Anantha Padmanabhan, and Gautam R. Desiraju. Structure-Property Correlations in Bending and Brittle Organic Crystals. *Crystal Growth & Design*, 6(12):2720–2731, 2006.

[191] Kuan-Lin Yeh, Hung-Lin Lee, and Tu Lee. Crystallization of form ii paracetamol with the assistance of carboxylic acids toward batch and continuous processes. *Pharmaceutics*, 14(5), 2022.

[192] M. Haisa, S. Kashino, R. Kawai, and H. Maeda. The Monoclinic Form of p-Hydroxyacetanilide. *Acta Crystallographica*, B30:1283–1285, 1976.

[193] M. Haisa, S. Kashino, and H. Maeda. The Orthorhombic Form of p-Hydroxyacetanilide. *Acta Crystallographica*, B30:2510–2512, 1974.

[194] A. BURGER. ZUR INTERPRETATION VON POLYMORPHIE-UNTERSUCHUNGEN. *Acta Pharm. Technol.*, 28(1):1–20, 1982.

[195] Marc Antoine Perrin, Marcus A. Neumann, Hagit Elmaleh, and Lionel Zaske. Crystal Structure Determination of the Elusive Paracetamol Form III. *Chemical Communications*, 22:3181–3183, 2009.

[196] Lauren R. Agnew, Dyanne L. Cruickshank, Thomas McGlone, and Chick C. Wilson. Controlled Production of the Elusive Metastable Form II of Acetaminophen

(Paracetamol): a Fully Scalable Templating Approach in a Cooling Environment. *Chem. Commun.*, 52(46):7368–7371, may 2016.

[197] Lauren R. Agnew, Thomas McGlone, Helen P. Wheatcroft, Amy Robertson, Anna R. Parsons, and Chick C. Wilson. Continuous Crystallization of Paracetamol (Acetaminophen) Form II: Selective Access to a Metastable Solid Form. *Crystal Growth & Design*, 17(5):2418–2427, 2017.

[198] P. Di Martino, A. M. Guyot-Hermann, P. Conflant, M. Drache, and J. C. Guyot. A New Pure Paracetamol for Direct Compression: The Orthorhombic Form. *International Journal of Pharmaceutics*, 128(1-2):1–8, 1996.

[199] Sunil Varughese, M. S.R.N. Kiran, Upadrasta Ramamurty, and Gautam R. Desiraju. Nanoindentation in Crystal Engineering: Quantifying Mechanical Properties of Molecular Crystals. *Angewandte Chemie - International Edition*, 52(10):2701–2712, 2013.

[200] Jerry Y.Y. Heng, Frank Thielmann, and Daryl R. Williams. The Effects of Milling on the Surface Properties of Form I Paracetamol Crystals. *Pharmaceutical Research*, 23(8):1918–1927, 2006.

[201] Jackson A. Jiménez and Fleming Martínez. Temperature Dependence of the Solubility of Acetaminophen in Propylene Glycol + Ethanol Mixtures. *Journal of Solution Chemistry*, 35(3):335–352, 2006.

[202] Roger A. Granberg, Dan G. Bloch, and Åke C. Rasmuson. Crystallization of Paracetamol in Acetone-Water Mixtures. *Journal of Crystal Growth*, 198-199(pt 2):1287–1293, 1999.

[203] Ajinkya V. Pandit and Vivek V. Ranade. Modeling Hysteresis during Crystallization and Dissolution: Application to a Paracetamol-Ethanol System. *Industrial and Engineering Chemistry Research*, 54(42):10364–10382, 2015.

[204] Niall A. Mitchell and Patrick J. Frawley. Nucleation Kinetics of Paracetamol Ethanol Solutions from Metastable Zone Widths. *Journal of Crystal Growth*, 312(19):2740–2746, 2010.

[205] Nurshahzanani Shahrir, Nornizar Anuar, Nur Aisyah Abdul Muttalib, Siti Nurul Ain Yusop, Mohd Rushdi Abu Bakar, Fatmawati Adam, and Siti Fatimah Ibrahim. The Role of Solvent Hydroxyl Functional Groups on the Interaction Energy and Growth of Form i Paracetamol Crystal Facets. *Organic Process Research and Development*, 26(12):3226–3235, 2022.

[206] Claire Thompson, Martyn C. Davies, Clive J. Roberts, Saul J.B. B Tendler, and Mike J. Wilkinson. The Effects of Additives on the Growth and Morphology of Paracetamol (Acetaminophen) Crystals. *Int. J. Pharm.*, 280(1):137–150, aug 2004.

[207] Sara Ottoboni, Michael Chrubasik, Layla Mir Bruce, Thai Thu Hien Nguyen, Murray Robertson, Blair Johnston, Iain D.H. Oswald, Alastair Florence, and Chris Price. Impact of Paracetamol Impurities on Face Properties: Investigating the Surface of Single Crystals Using TOF-SIMS. *Crystal Growth & Design*, 18(5):2750–2758, 2018.

[208] Boris Yu Shekunov, David J.W. Grant, Roger J. Latham, and John N. Sherwood. In situ Optical Interferometric Studies of the Growth and Dissolution Behavior of Paracetamol (Acetaminophen) Crystals. 3. Influence of Growth in the Presence of p-acetoxyacetanilide. *Journal of Physical Chemistry B*, 101(44):9107–9112, 1997.

[209] Naghmeh Fatemi, Cedric Devos, Tom Van Gerven, and Simon Kuhn. Continuous Crystallization of Paracetamol Exploiting Gas–liquid Flow in Modular Nucleation and Growth Stages. *Chemical Engineering Science*, 248:117095, 2022.

[210] Stephanie J. Urwin, Stephanie Yerdelen, Ian Houson, and Joop H. Ter Horst. Impact of Impurities on Crystallization and Product Quality: A Case Study with Paracetamol. *Crystals*, 11(11):1344, nov 2021.

[211] W. H. Liao, S. J. Aggarwal, and J. K. Aggarwal. The Reconstruction of Dynamic 3D Structure of Biological Objects Using Stereo Microscope Images. *Machine Vision and Applications*, 9(4):166–178, 1996.

[212] Faris Abouakil, Huicheng Meng, Marie Anne Burcklen, Hervé Rigneault, Frédéric Galland, and Loïc LeGoff. An Adaptive Microscope for the Imaging of Biological Surfaces. *Light: Science and Applications*, 10(1), 2021.

[213] Fred Koenig. Compound Microscopes vs Stereo Microscopes - How Do They Compare?, 2020.

[214] Spencer Cox. Everything You Need to Know About Macro Photography, 2023.

[215] Adobe. Thinking small for a big impact with macro photography., 2024.

[216] DPReview. Nikon D90 Specs, 2008.

[217] A. Gavezzotti. Structure and Intermolecular Potentials in Molecular Crystals. *Modelling and Simulation in Materials Science and Engineering*, 10(3), 2002.

[218] Hayat Khan, Aditya S. Yerramilli, Adrien D'Oliveira, Terry L. Alford, Daria C. Boffito, and Gregory S. Patience. Experimental Methods in Chemical Engineering: X-ray Diffraction Spectroscopy—XRD. *Canadian Journal of Chemical Engineering*, 98(6):1255–1266, 2020.

[219] George F. Harrington and José Santiso. Back-to-Basics Tutorial: X-ray Diffraction of Thin Films. *Journal of Electroceramics*, 47(4):141–163, 2021.

[220] Victoria Klang and Nadejda B. Matsko. Electron Microscopy of Pharmaceutical Systems. *Advances in Imaging and Electron Physics*, 181:125–208, 2014.

[221] A. Bogner, P. H. Jouneau, G. Thollet, D. Basset, and C. Gauthier. A History of Scanning Electron Microscopy Developments: Towards "wet-STEM" Imaging. *Micron*, 38(4):390–401, 2007.

[222] NANOIMAGES Perfect Focus. SEM Technology Overview – Scanning Electron Microscopy, 2023.

[223] Erik Luyk. Backscattered Electrons in SEM Imaging, 2019.

[224] A.D. Micheals. Materials analysis and failure analysis. In Jay A. Siegel, Pekka J. Saukko, and Max M. Houck, editors, *Encyclopedia of Forensic Sciences (Second Edition)*, pages 483–493. Academic Press, Waltham, second edition edition, 2013.

[225] G. Greczynski and L. Hultman. X-ray Photoelectron Spectroscopy: Towards Reliable Binding Energy Referencing. *Progress in Materials Science*, 107(April 2019):100591, 2020.

[226] Fred A. Stevie and Carrie L. Donley. Introduction to X-ray Photoelectron Spectroscopy. *Journal of Vacuum Science & Technology A: Vacuum, Surfaces, and Films*, 38(6), 2020.

[227] S. R. Stock. X-ray Microtomography of Materials. *International Materials Reviews*, 44(4):141–164, 1999.

[228] National Institute of Standards and Technology U.S. Department of Commerce. NIST X-ray Photoelectron Spectroscopy Database (SRD 20), Version 5.0.

[229] David J. Shuman, André L.M. Costa, and Margareth S. Andrade. Calculating the Elastic Modulus from Nanoindentation and Microindentation Reload Curves. *Materials Characterization*, 58(4):380–389, 2007.

[230] Manish Kumar Mishra, Pinki Mahur, Praveena Manimunda, and Kamini Mishra. Recent Advances in Nanomechanical Measurements and Their Application for Pharmaceutical Crystals. *Molecular Pharmaceutics*, 20(10):4848–4867, 2023.

[231] W. C. Oliver and G. M. Pharr. Measurement of Hardness and Elastic Modulus by Instrumented Indentation: Advances in Understanding and Refinements to Methodology. *Journal of Materials Research*, 19(1):3–20, 2004.

[232] Bharat Bhushan. Depth-sensing Nanoindentation Measurement Techniques and Applications. *Microsystem Technologies*, 23(5):1595–1649, 2017.

[233] Tatyana N. Drebushchak and Elena V. Boldyreva. Variable Temperature (100-360 K) Single-crystal X-ray Diffraction Study of the Orthorhombic Polymorph of Paracetamol (p-hydroxyacetanilide). *Zeitschrift fur Kristallographie*, 219(8):506–512, 2004.

[234] H. Sun. Compass: An ab initio Force-field Optimized for Condensed-phase Applications - Overview with Details on Alkane and Benzene Compounds. *Journal of Physical Chemistry B*, 102(38):7338–7364, 1998.

[235] Stephen L. Mayo, Barry D. Olafson, and William A. Goddard. DREIDING: A Generic Force Field for Molecular Simulations. *Journal of Physical Chemistry*, 94(26):8897–8909, 1990.

[236] A. K. Rappé, C. J. Casewit, K. S. Colwell, W. A. Goddard, and W. M. Skiff. UFF, a Full Periodic Table Force Field for Molecular Mechanics and Molecular Dynamics Simulations. *Journal of the American Chemical Society*, 114(25):10024–10035, 1992.

[237] Hans C. Andersen. Molecular Dynamics Simulations at Constant Pressure and/or Temperature. *The Journal of Chemical Physics*, 72(4):2384–2393, 02 1980.

[238] Wendy C. Duncan-Hewitt, David L. Mount, and Alfred Yu. Hardness Anisotropy of Acetaminophen Crystals, 1994.

[239] Korlakunte V.R. Prasad, David B. Sheen, and John N. Sherwood. Fracture Property Studies of Paracetamol Single Crystals Using Microindentation Techniques. *Pharmaceutical Research*, 18(6):867–872, 2001.

[240] Stuart Finnie, Korlakunte V.R. Prasad, David B. Sheen, and John N. Sherwood. Microhardness and Dislocation Identification Studies on Paracetamol Single Crystals. *Pharmaceutical Research*, 18(5):674–681, 2001.

[241] D. Olusanmi, K. J. Roberts, M. Ghadiri, and Y. Ding. The Breakage Behaviour of Aspirin Under Quasi-static Indentation and Single Particle Impact Loading: Effect of Crystallographic Anisotropy. *International Journal of Pharmaceutics*, 411(1-2):49–63, 2011.

[242] Benjamin P.A. Gabriele, Craig J. Williams, Matthias Eckhard Lauer, Brian Derby, and Aurora J. Cruz-Cabeza. Nanoindentation of Molecular Crystals: Lessons Learned from Aspirin. *Crystal Growth & Design*, 20(9):5956–5966, 2020.

[243] Anne Nong, Claire Schleper, Abigail Martin, Mitchell Paolello, Fredrik Lars Nordstrom, and Gerard Capellades. Impurity Retention and Pharmaceutical Solid Solutions: Visualizing the Effect of Impurities on Dissolution and Growth using Dyed Crystals. *CrystEngComm*, 26(38):5337–5350, 2024.

[244] Jerry Y Y Heng, Alexander Bismarck, Adam F Lee, Karen Wilson, and Daryl R Williams. Anisotropic Surface Energetics and Wettability of Macroscopic Form I Paracetamol Crystals. *Langmuir*, 22:2760–2769, 2006.

[245] C. T. Óciardhá, N. A. Mitchell, K. W. Hutton, and P. J. Frawley. Determination of the Crystal Growth Rate of Paracetamol as a Function of Solvent Composition. *Industrial and Engineering Chemistry Research*, 51(12):4731–4740, 2012.

[246] Noriaki Kubota Ã. A New Interpretation of Metastable Zone Widths Measured for Unseeded Solutions. *Journal of Crystal Growth*, 310:629–634, 2008.